Cherenkov radiation in the soft X-ray region : towards a compact narrowband source

Please check the document version of this publication:

Cherenkov radiation in the soft x-ray region: towards a compact narrowband source

Cherenkov radiation in the soft x-ray region: towards a compact narrowband source

PROEFSCHRIFT

ter verkrijging van de graad van doctor aan de Technische
Universiteit Eindhoven, op gezag van de Rector Magnificus,
prof.dr. R.A. van Santen, voor een commissie aangewezen
door het College voor Promoties in het openbaar te verdedigen
op dinsdag 10 februari 2004 om 16.00 uur

door

Walter Knulst

geboren te Alkmaar

Dit proefschrift is goedgekeurd door de promotoren:

prof.dr. M.J. van der Wiel
en
prof.dr.ir. G.M.W. Kroesen

Copromotor:
dr.ir. O.J. Luiten

This thesis is based on the following publications:

1. J. Corstens, W. Knulst, O.J. Luiten and M.J. van der Wiel, "An efficient method for calculating plural scattering of relativistic electrons in thin foils and multilayers", submitted to Nucl. Instrum. Methods B.

2. W. Knulst, M.J. van der Wiel, O.J. Luiten and J. Verhoeven, "High-brightness, narrowband, and compact, soft x-ray Cherenkov sources in the water window", *Appl. Phys. Lett* **83**, 4050-4052 (2003).

3. W. Knulst, M.J. van der Wiel, O.J. Luiten and J. Verhoeven, "High-brightness, compact soft x-ray source based on Cherenkov radiation", *in Proceedings of SPIE Annual Meeting 2003 in San Diego*, 2003.

4. W. Knulst, O.J. Luiten, M.J. van der Wiel and J. Verhoeven "Goniometer to measure the angular distribution of narrow-band soft x-ray cherenkov radiation", *Proceedings of EPAC 2002*, (Paris, France, 2002), 706-708.

5. W. Knulst, O.J. Luiten, M.J. van der Wiel and J. Verhoeven, "Observation of narrow band Si L-edge Cerenkov radiation generated by 5 MeV electrons", *Appl. Phys. Lett.* **79**, 2999-3001 (2001).

6. W. Knulst, O.J. Luiten, M.J. van der Wiel and J. Verhoeven, "A tabletop soft x-ray source based on 5-10 MeV LINACs", *Proceeding of EPAC 2000*, (Vienna, Austria, 2000), 2609-2611.

Contents

1   Introduction

This thesis describes an investigation on the physics of a new type of radiation source in the soft x-ray region. This part of the spectrum (from about 100 eV[*] to several keV) causes on the one hand large difficulties due to the extremely high absorption of all materials. On the other hand it creates great opportunities like imaging of nm-size features, because of the short wavelength, and chemical identification, enabled by the atomic resonances of all elements in this region. The principle of the soft x-ray source is the emission of Cherenkov radiation by relativistic electrons passing through a foil. That such emission occurs not only in the visible, but also in the soft x-ray region, is not widely known. It was established experimentally only relative recently with the use of electrons at energies of 75 MeV and 1.2 GeV. This project of investigating the feasibility of a compact soft x-ray source based on the Cherenkov effect was initiated by J. Verhoeven[1,2,3] at the FOM-institute AMOLF.

On the basis of extensive, but still somewhat incomplete data sets of optical constants of various materials in the soft x-ray region, a number of features of Cherenkov radiation can be predicted. The main goal of this project was to demonstrate these features experimentally, namely:

> (i) Electron energies in the 5-10 MeV range are sufficient to generate the radiation.
> (ii) The spectrum consists of a single, narrow line, which strongly peaks above a continuous background of transition radiation. That is inherently coupled the physical principle of the source.
> (iii) The emission is forwardly directed, which enables efficient collection of all radiation using grazing-incidence optics.
> (iv) The soft x-ray yield, which is the number of photons generated per electron, is sufficient to consider application as a real source.
> (v) A range of soft x-ray photon energies can be generated from a series of materials, which are available in the form of μm-thick foils.

After established the above features, the conclusion is drawn that a new type of soft x-ray source is indeed possible. With the use of compact (i.e. tabletop), commercially available

---

[*] Boundaries are not well defined. Often the region from 30 eV to 250 eV is called extreme ultraviolet (EUV).

electron-accelerators, a laboratory-sized source can be build as an alternative to other compact sources or large-scale facilities producing synchrotron radiation. Such a Cherenkov source is inherently narrowband and different wavelengths are selected with a simple exchange of foils. The brightness that can be achieved is comparable to laser-produced plasma sources.

In this introduction the principles of emission by relativistic electrons are reviewed, a brief introduction of the Cherenkov effect in the soft x-ray region is presented, a comparison with other compact soft x-ray sources is made and some applications of such sources are briefly discussed.

1.1 Radiation by relativistic electrons

Our proposed Cherenkov source is based on radiation generated by relativistic electrons. This application of relativistic electrons fits perfectly in the theme of our research group, which is the development of tabletop, high-quality electron accelerators and the study of the generation of radiation by relativistic electrons. In this section the principle of different radiation phenomena by relativistic electrons is illustrated.
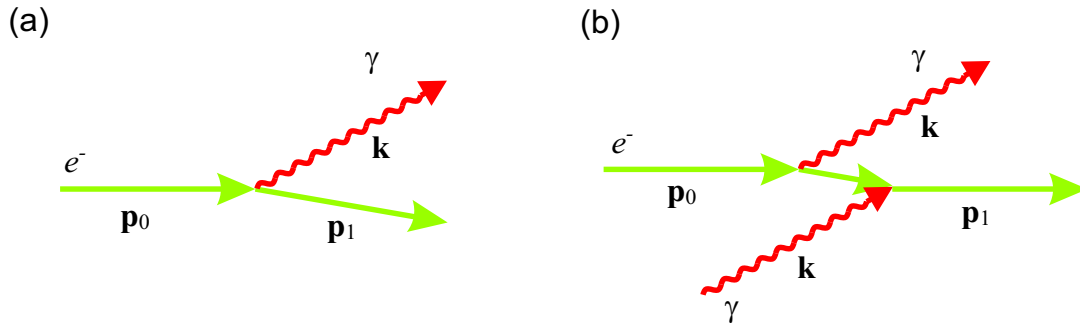
Figure 1.1: (a) Emission of a photon by an electron. (b) Emission and re-absorption of a (virtual) photon by an electron.

An electron moving with constant velocity on a linear trajectory in vacuum, far from any material and in the absent of external fields, emits no radiation. In other words, the only solution of the Maxwell equations is the Coulomb field that is accompanying the electron. Using the concept photon from the quantum mechanical point of view, the process $e^- \rightarrow e^- + \gamma$ [see Fig. 1.1(a)] is kinematically forbidden, because it is impossible to satisfy simultaneously the constraints of energy and momentum conservation:

$$E_0^{el} = E_1^{el} + E^{ph} , \tag{1.1}$$

$$\mathbf{p}_0 = \mathbf{p}_1 + \hbar\mathbf{k} . \tag{1.2}$$

The dispersion relation of an electron and photon couples the energy E with the momentum $\mathbf{p}$ and $\mathbf{k}$, respectively:

$$E^{el}(\mathbf{p}) = \sqrt{m_0^2 c^4 + \mathbf{p}^2 c^2} , \tag{1.3}$$

$$E^{ph}(\mathbf{k}) = \hbar|\mathbf{k}|c .\qquad(1.4)$$

On the other hand, the process $e^- \rightarrow e^- + \gamma \rightarrow e^-$ in Fig. 1.1(b) is allowed by the uncertainty principle, providing that the intermediate state lasts a sufficiently short time. In this case, at least one of the above equations is violated. This is the origin of the "virtual photon cloud", which is the quantum description of the Coulomb field. With this picture, a few radiation phenomena of relativistic electrons are discussed.

(i) An electron in an external field. From classical electromagnetism it is well known that the Liénard-Wiechert potential, which describes the field of a moving electron, contains a radiation term that only has a value when the electron experiences acceleration due to an external force. Therefore, momentum and energy exchange takes place with the source of the external force and an extra term is added in the initial state, i.e. $\mathbf{p}_0 + \mathbf{p}_{ext}$. As a consequence the emission of a photon is allowed, i.e. the virtual photon has become real. This case applies to synchrotron radiation, Bremsstrahlung, channeling radiation and Compton scattering.

(ii) Uniform motion inside a homogeneous medium. The refractive index of the medium determines the phase velocity of light, thus the dispersion relation of the photon (1.4) is changed. If the velocity of the electron exceeds the phase velocity of light, the momentum and energy conservation is satisfied and Cherenkov radiation is emitted.

(iii) Uniform motion inside a heterogeneous medium. When the electron passes through or close to a piece of matter, it induces polarization currents, which in turn can generate radiation. This process can be viewed as a scattering process of the virtual photon into a real photon. The recoil of the material due to the scattering appears in the momentum equation and thereby allows the emission of radiation. This case applies to transition radiation, parametric x-rays and Smith-Purcell radiation.

Emission mechanisms that have been widely used as an x-ray radiation source are so far only Bremsstrahlung (x-ray tubes), synchrotron radiation (storage rings) and very recently free-electron-laser radiation. Some attempts have been made to use other emission mechanisms. X-ray microlithography have been demonstrated with keV transition-radiation using 245-MeV electrons[4]. Compton scattering has been demonstrated to generate multi-keV x-ray radiation with a reasonable yield using 17-MeV electrons[5]. The subject of this thesis is the generation of narrowband and forward-directed radiation in the soft x-ray spectral region using the Cherenkov mechanism[6]. In this spectral region the intensity of Cherenkov radiation is higher than that of transition radiation, Bremsstrahlung or Compton scattering.

1.2   Soft x-ray Cherenkov radiation: a novel source

Cherenkov radiation is emitted by a charged particle if its velocity (v) exceeds the phase velocity of light in a medium ($v_\varphi = c/n$) and is therefore limited to the wavelength regions where the real part of the refractive index exceeds unity ($n > 1$). Particular for Cherenkov radiation is the emission angle, which is illustrated in Fig. 1.2 by a Huygens construction: along the trajectory of the charged particle spherical waves are generated that expand with the phase velocity. Constructive interference between radiation from all source points, which is observed in Fig. 1.2 (b) for the case of $v > v_\varphi$, forms a propagating wave front that is identified

as Cherenkov radiation. The propagation direction of the wave front with respect to the electron trajectory is simply given by

$$\cos\theta = \frac{v_\varphi}{v} = \frac{c}{nv}, \tag{1.5}$$

which is called the Cherenkov relation.
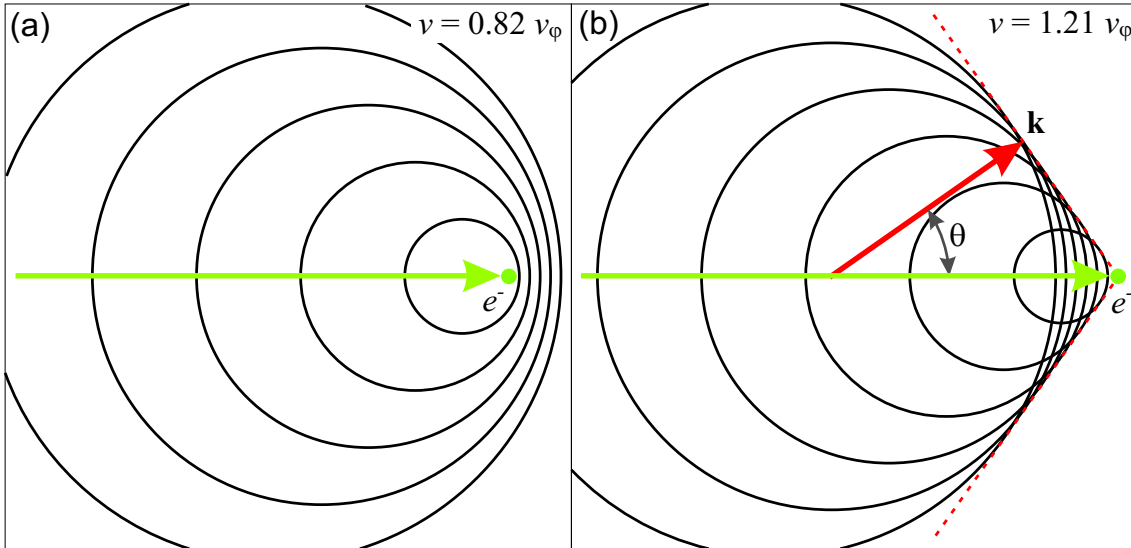
Figure 1.2: Huygens construction of Cherenkov radiation: (a) An electron traveling with velocity $v = 0.82\ v_\varphi$ and emitting spherical waves along its trajectory. (b) An electron traveling with velocity $v = 1.21\ v_\varphi$ and emitted spherical waves interfering constructively into a wave front, which is the Cherenkov radiation. This wave front propagates with an angle θ with respect to the electron trajectory.

Due to the fact that materials are dispersive, Cherenkov radiation is only generated in limited spectral regions as is indicated by Fig. 1.3. In the visible region Cherenkov radiation is a well-known effect, which is often applied in high-energy particle detection[7]. In the soft x-ray region, however, the refractive index is generally smaller than unity and materials are highly absorbing. Therefore, Cherenkov radiation in the soft x-ray region was excluded for a long time. In 1981 Bazylev *et al.*[8], however, realized that at some inner-shell absorption edges the refractive index exceeds unity and Cherenkov radiation can be generated in a narrowband region, which was demonstrated for the carbon K-edge (284 eV) using 1.2-GeV electrons. Later, also Moran *et al.*[9] showed that Cherenkov radiation is emitted by 75-MeV electrons in silicon at the L-edge (99.7 eV) and in carbon at the K-edge. Only a few theoretical studies[10,11] have addressed the feasibility of soft x-ray Cherenkov radiation at inner-shell photon energies.

This thesis is about using electron beams of moderate energies (5-25 MeV), which are generated by laboratory-sized accelerators, to produce soft x-ray Cherenkov radiation from a variety of foils with photon energies ranging from 100 eV up to 1 keV. Below a few characteristics of the soft x-ray Cherenkov radiation are listed.

      (i) The radiation is characterized by a narrow bandwidth. Due to the resonant anomalous dispersion at some inner-shell absorption edges the refractive index

exceeds unity in a narrow spectral region where Cherenkov radiation is generated. In addition, the part generated at the high photon-energy side of the edge is reabsorbed by the medium due to the high absorption. Therefore, the soft x-ray Cherenkov radiation originates effectively from the part in front of the absorption edge, having typically a width of a few electron-volts.

(ii) The radiation is emitted in the forward direction. In the soft x-ray region the refractive index is close to unity and can exceed unity only slightly (0.1% up to 5%) at the absorption edges. The Cherenkov angle is determined by the refractive index value and has typically a value between 1° and 12°.
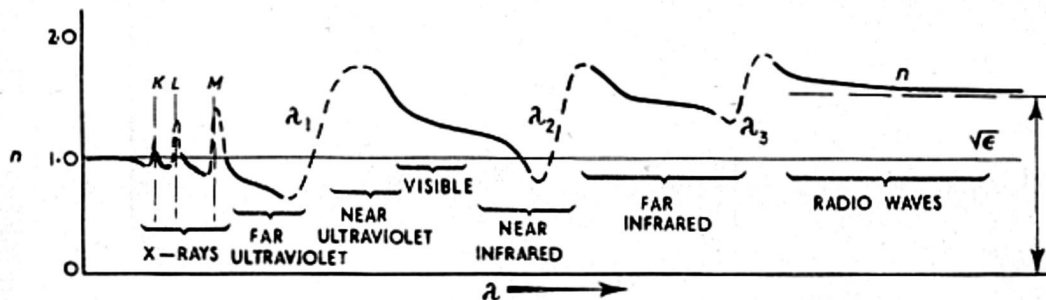
Figure 1.3: General behavior of the refractive index as a function of wavelength from Ref. 12.

(iii) Theoretical analysis shows that the soft x-ray Cherenkov yield is typically between 10^{-4} and 10^{-3} photon per electron. Although this seems a relatively low number, the use of commercially available accelerators with average current in the order of 0.1 mA, i.e. 10^{15} electrons per second, leads to a usable output of 10^{12} soft x-ray photons per second.

(iv) The soft x-ray source size is mainly determined by the electron beam spot size on the target foil. An electron beam can be focused by dedicated charged particle optics to a spot size of about 10 μm.

(v) The energy of the electron source required to generate the soft x-ray Cherenkov radiation is determined by the Cherenkov condition ($v > v_\varphi$), i.e. typically between 2 MeV and 10 MeV. We show that optimal generation of soft x-ray Cherenkov radiation require electron energies of a few times the minimal value. This means that compact accelerators of 5 to 25 MeV are sufficient.

All these characteristics determine together the source brightness, which is a figure of merit for the source quality expressed in the number of photons per second, per steradian, per micron squared source area and per 0.1% bandwidth. Especially the narrow bandwidth and forward directed emission, which are intrinsically coupled to Cherenkov radiation in the soft x-ray region, contribute to a potentially high value of the brightness.

In conclusion, using a tabletop accelerator to generate Cherenkov radiation a possible high-brightness, narrowband, and compact source in the soft x-ray region may be realized. The main advantages of this source compared to other compact sources are that it does not produce any debris and that the radiation produced may be collected completely by, for instance, grazing-incidence optics. As in many other sources, the strong narrowband

Cherenkov emission is superimposed on a broad, continuous background. This background consists of hard x-ray Bremsstrahlung and transition radiation, which are an unavoidable byproduct of the passage of relativistic electrons through a foil. This thesis describes ways to isolate the soft x-ray component in case of the measurements on the Cherenkov effect, and to deal with the hard x-ray background in a real source design.

1.3   Laboratory-sized, soft x-ray sources

Ever since the discovery in 1895 of x-rays by Röntgen, x-ray tubes are applied as compact x-ray sources in many fields of research. The spectrum consists of a continuous part of Bremsstrahlung up to the kinetic energy of the electrons and superimposed a series of fluorescence lines that are characteristic for the anode material. The photon energy and the intensity of the fluorescence line increase with the atomic number. The emission intensity in the soft x-ray region, which requires low-Z materials, is very low. Recently, an EUV tube[13] and a liquid-water-anode tube[14] have been investigated for the production of silicon L-band fluorescence radiation (centered at 92 eV) and oxygen K_α-fluorescence radiation (525 eV), respectively.

An alternative is the use of plasma-based sources. These sources cover the range from visible radiation up to x-rays of a few kilo-electron-volts. X-ray emission is generated by bound-bound and free-bound transitions from a wide range of ionization states. These plasma-based sources can be divided into two groups: electrical-discharge produced and laser produced. The first group covers electrical discharges that are called, for instance, X- or Z-pinches depending on the shape of their electrodes, in which a high current pulse is sent through a plasma to make it collapse. At this moment, these kinds of sources are considered as the only solution for EUV-lithography[15], because they might be capable of producing the very intense radiation at 13.5-nm required for this application.

The latter group covers laser-produced plasmas, in which high-power laser pulses are fired at a target. For relative long laser pulses (in the order of nanoseconds) the emission spectrum is comparable with the discharge-produced plasmas and depends on illumination conditions as well as target material. Solid targets have the disadvantage that a large amount of debris is produced that spoils all the optics near the plasma. Therefore, gas and liquid jets, e.g. xenon gas, ethanol[16] or liquid nitrogen[17], have been applied as target, which reduces the debris production considerably, but not to zero.

A third group of compact sources is high-harmonic generation with femtosecond laser pulses. When such a very short, highly intense, laser pulse is sent through a gas, very high odd harmonics of the incident laser pulse are generated by non-linear interaction. These harmonics typically emerge as a coherent, low-divergence beam. The conversion efficiency at high photon-energies is limited by the lack of phase matching and therefore these harmonics merge into a quasi-continuum that extends into the water-window region[18].

Recently, it has been shown that laser-produced plasmas and high-harmonic generation are sufficiently bright for practical imaging in the water window[19] and at 13 nm[20], respectively. In Chapter 6 the brightness of these compact soft x-ray sources is compared with our proposed Cherenkov source.

1.4   Applications of compact, soft x-ray sources

Applications generally set the demands for the source. Imaging in the soft x-ray region is very interesting, because the short wavelength enables higher resolution than can be obtained with visible light. Roughly, imaging applications can be divided in two groups: production and analyzing tools. For lithography, which is an example of the first group, one of the challenges is the development of a production machine that operates at 13.5 nm to produce very small integrated circuits. This requires, among other problems, a high-power source to get a profitable throughput of wafers. Additionally, the power requirement is extra high to compensate the reflection losses at the optics. A simple estimate shows that the proposed Cherenkov source, which can produce 12.4-nm radiation with silicon, can never reach these power values (typically, 100 W of collected, in-band radiation).
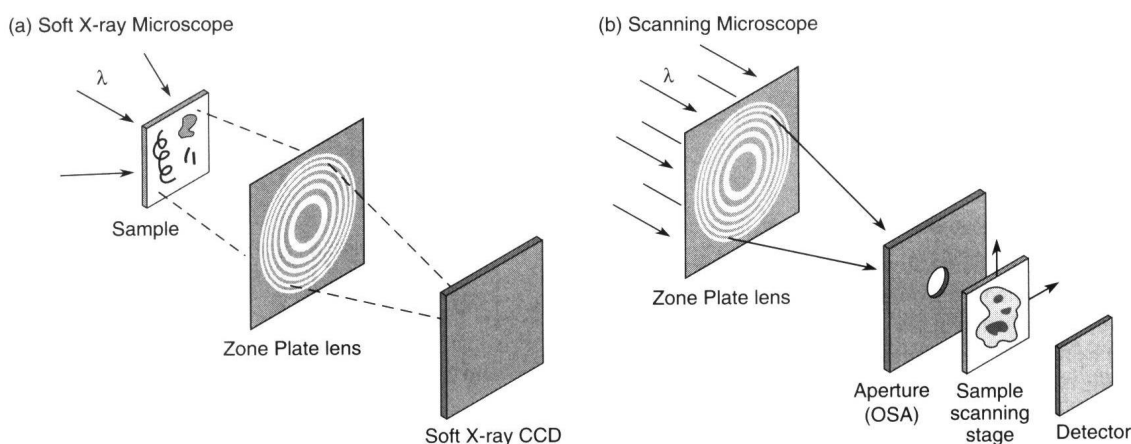
Figure 1.4: (a) Scheme of a soft x-ray microscopy in which a complete image is formed at the CCD. (b) Scheme of a scanning soft x-ray microscope in which the sample is scanned past a focused spot. From Ref. 22.

Analyzing tools generally put less demands on the power, but still require light of high quality. Each analyzing technique puts constrains on one or a combination of the following parameters, such as bandwidth, solid angle and intensity that is required at the sample position. Applications in the soft x-ray region are found in element and chemical analysis, for instance, photoelectron or x-ray spectroscopy in combination with microscopy to obtain spatial information. A soft x-ray Cherenkov source operates mainly at discrete energies from 100 eV up to 1 keV determined by absorption edges of the target material. Therefore, applications are limited to those requiring a monochromatic source. In this section two applications are discussed in some detail: soft x-ray microscopy[21,22], which up to now are mostly operated at synchrotrons, and x-ray photoelectron spectroscopy (XPS), which is mainly operated with an x-ray tube in laboratory-scale instruments.

The soft x-ray microscope[†] technique has been developed in the 1970s. In Fig. 1.4(a) the schematic layout of a microscope is shown, in which the incident x-ray beam passes through the sample and is partially absorbed with a spatial variation depending on the local

---

[†] Sometimes called a transmission x-ray microscope (TXM).

composition. The emerging radiation is then diffracted by the zone plate lens to form a first order image on a CCD chip to create a high-resolution image. In Fig. 1.4(b) the schematic layout of a scanning soft x-ray microscope‡ is shown, which is often applied in combination with analyzing techniques such as x-ray fluorescence and photoelectron spectroscopy.
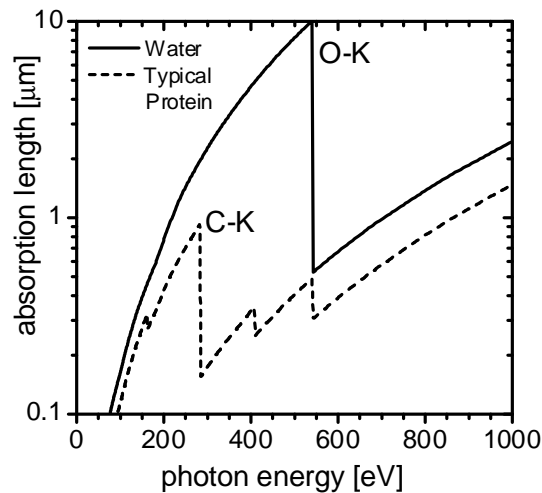
Figure 1.5: The absorption length for soft x-rays in water and a typical protein as a function of photon energy. The natural contrast is obtained in the water window, between the carbon and oxygen absorption edge, where the high carbon content protein is absorbing but where water is relatively transparent.

For biological studies soft x-ray microscopy provides a unique set of capabilities in between those of visible light and electron microscopy. Nature provides a 'water-window' spectral region between the K absorption-edge of carbon (284 eV) and of oxygen (543 eV), where organic materials show strong absorption and phase contrast, while water is relatively non-absorbing (see Fig. 1.5). This enables imaging of specimens that are several microns thick with high intrinsic contrast, such as animal cells that are typically 10-30 μm in size and contain a large fraction of water (70%). The photon energy used is sufficient to break chemical bonds and to ionize atoms, which can cause chemical and structural damage, which is called radiation damage. Typically, to make a high-resolution image a radiation dose of 10^6–10^8 Gray is required and therefore living specimens can be imaged only once. Such problems can be reduced by using very short exposure times (faster than structural changes appear) or using chemically fixed, frozen-hydrated or dehydrated specimens.

X-ray photoelectron spectroscopy§ (XPS) is based on the photoelectric effect, in which an incident x-ray photon transfers its energy to a bound electron near the material-vacuum interface, resulting in a transition to a free electron state in the continuum above the vacuum level [see Fig. 1.6(a)]. The electrons emitted from the surface obtain a kinetic energy equal to that of the incident photon minus the binding energy of the electron in its initial state. From the kinetic-energy spectrum of the emitted electrons [see Fig. 1.6(b)], the different elements

---

‡ Often referred to as a scanning transmission x-ray microscope (STXM).
§ XPS is also referred to as electron spectroscopy for chemical analysis (ESCA).

and their concentration can be determined, as well as the nature of the chemical environment from the energy shift of the binding energy. Due to the limited range of the electrons in the solid, this technique provides information on the surface and on a thin layer below the surface of typically a few ångströms. By focusing the incident radiation to a small spot on the target surface, also spatial information is obtained; this technique is often called photoemission microscopy or spectromicroscopy. Commercially available XPS-systems use often Al K_α (1486.6 eV) or Mg K_α-lines (1253.6 eV) generated with x-ray tubes.
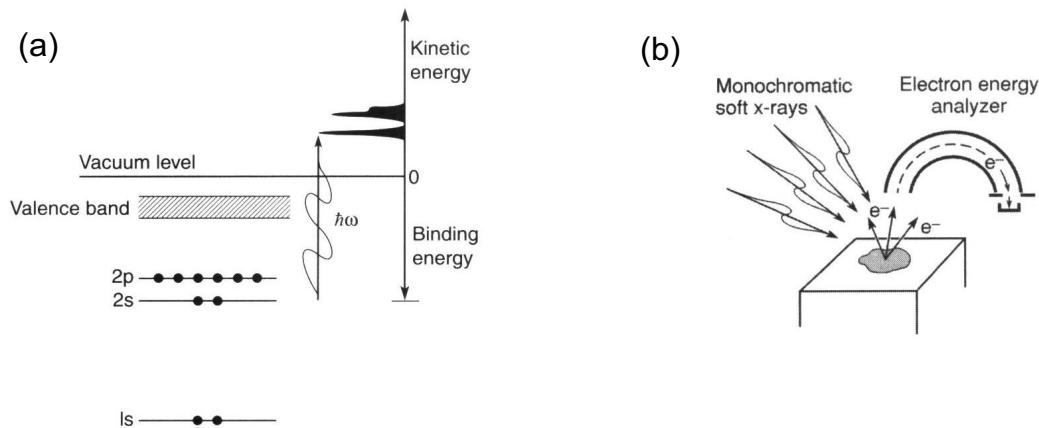
Figure 1.6: (a) The process of photoemission, in which an absorbed photon transfers its energy to a bound electron near the material-vacuum interface, results in a transition to a free electron state in the vacuum. (b) Monochromatic x-rays are incidenting on the target surface and the emitted electrons are analyzed by an electron energy spectrometer. From Ref. 22.

1.5   Scope of this thesis

Narrowband soft x-ray Cherenkov radiation is the theme of this thesis and is discussed from a theoretical and experimental point of view. The electromagnetic theory of Cherenkov radiation is already established for a long time. However, soft x-ray Cherenkov radiation sheds new light on this theory. In Chapter 2 we compare the electromagnetic theory of Cherenkov radiation with the theory of transition radiation. We show that especially in the soft x-ray region the accurate description of the Cherenkov radiation is given, due to the high absorption, by the theory that is initially intended for transition radiation. In the last section of Chapter 2 the soft x-ray Cherenkov radiation is presented for the case of a grazing-incident electron beam on the foil. A previous investigation[9] shows that 75-MeV electrons at grazing-incidence enhance the soft x-ray Cherenkov intensity. We discuss phenomenologically grazing-incidence Cherenkov radiation for 5-MeV to 10-MeV electrons, for which intensity enhancement is much more subtle. Different aspects are discussed, such as external generation, absorption, total internal reflection and transmission through the interface between an absorbing medium and vacuum.

Soft x-ray Cherenkov radiation is generated by relativistic electrons in micrometer thick foils. While passing through the foil the electrons are mainly scattered elastically. Therefore,

the characteristic of the produced radiation is influenced by the angular distribution of the electron beam. This is very important for analyzing the influence of the scattering on the brightness of the narrowband soft x-ray Cherenkov source. In Chapter 3 the elastic scattering theory of relativistic electrons is reviewed and a summation method is introduced for efficiently calculating the angular scattering distribution after passing through an arbitrary thin foil or multilayer structure.

In Chapter 4 the two experimental setups, respectively at a 5-MeV and a 10-MeV electron accelerator are presented, which have been used to analyze soft x-ray Cherenkov radiation generated in different materials. Each setup is equipped with a detection system that is dedicated for a certain photon-energy region, respectively, around 100 eV and from the water window upwards. The method to separate the soft x-ray component from the visible and hard x-ray background is specific for each detection setup. In Chapter 5 the measurements of the Cherenkov radiation are discussed. The purpose of the experiments is to demonstrate that moderate electron energies are already sufficient to generate soft x-ray Cherenkov radiation in different materials. We have firmly established the generation of silicon L-edge, titanium L-edge and vanadium L-edge Cherenkov radiation with 5-MeV electrons for the first case and 10-MeV electrons for the last two cases. In addition, some serious attempts have been made to establish Cherenkov radiation at carbon-K and nickel-L and from the chemical compound silicon nitride. The fact that, in contract to theory, we did not observe Cherenkov radiation using carbon put a new upper limit on the refractive index at the K-edge.

On the basis of the measured soft x-ray Cherenkov lines, the brightness is presented in Chapter 6 for the case of an optimum electron beam. As is discussed in this chapter the maximum current density that can be sent through a target foil is limited by the heat load and the quality of the accelerator. This analysis presents the maximum achievable brightness. Compared with other compact soft x-ray sources, our Cherenkov source in water-window spectral region has an estimated brightness that is comparable to the best laser-produced plasma sources. In the second part of that chapter optical design issues are discussed for constructing a compact soft x-ray Cherenkov source. An important aspect is the collection of soft x-ray Cherenkov radiation and focusing it into point where a sample can be placed. This chapter is concluded by showing that the proposed soft x-ray Cherenkov source fulfills the requirements for the application as the source for soft x-ray microscopy and x-ray photoelectron spectroscopy.

References

1   J. Verhoeven, B. Lastdrager, A. Tip and D.K.G. de Boer, International Patent No. WO 00/36471 (22 June 2000).

2   J. Braat and J. Verhoeven, International Patent No. WO 00/38015 (29 June 2000).

3   B. Lastdrager, *Transition radiation and Cherenkov radiation. Classical and quantum mechanical calculations*, Graduation Report Universiteit van Amsterdam, Amsterdam, 1997.

4   M.A. Piestrup, D.G. Boyers, C.I. Pincus, J.L. Harris, H.S. Caplan, R.M. Silzer and D.M. Skopik, "Beryllium foil transition-radiation source for x-ray lithography", *Appl. Phys. Lett.* **59**, 189-191 (1991).

5   M. Uesaka, H. Kotaki, K. Nakajima, H. Harano, K. Kinoshita, T. Watanabe, T. Ueda, K. Yoshii, M. Kando, H. Dewa, S. Kondo and F. Sakai, "Generation and application of femtosecond X-ray pulse", *Nucl. Instrum. Methods* **A455**, 90-98 (2000).

6   W. Knulst, O.J. Luiten, M.J. van der Wiel and J. Verhoeven, "A tabletop soft x-ray source based on 5-10 MeV LINACs", *Proceeding of EPAC 2000*, Vienna, 2000.

7   C. Grupen, *Particle Detectors*, Cambridge University Press, Cambridge, 1996.

8   V.A. Bazylev, V.I. Glebov, E.I. Denisov, N.K. Zhevago, M.A. Kumakhov, A.S. Khlebnikov and V.G. Tsinoev, "X-ray Cerenkov radiation. Theory and experiment", *Sov. Phys. JETP* **54**, 884-892 (1981).

9   M.J. Moran, B. Chang, M.B. Schneider and X.K. Maruyama, "Grazing-incidence Cherenkov X-ray generation", *Nucl. Instrum. Methods* **B48**, 287 (1990).

10 A.E. Kaplan, C.T. Law and P.L. Shkolnikov, *Phys. Rev.* **E52**, 6795-6808 (1995).

11 B. Lastdrager, A. Tip and J. Verhoeven, *Phys. Rev.* **E61**, 5767-5778 (2000).

12 J.V. Jelley, *Cherenkov radiation and its applications*, Pergamon Press, London, 1958.

13 A. Egbert, B. Mader, B. Tkachenko, A. Ostendorf, C. Fallnich, B.N. Chichkov, T. Missalla, M.C. Schürmann, K. Gäbel, G. Schriever and U. Stamm, "Compact electron-based extreme ultraviolet source at 13.5 nm", *J. Microlith., Microfab., Microsyst.* **2**, 136-139 (2003).

14 B. Buijsse, "A keV-electron-based tabletop soft X-ray source", in Proceedings of SPIE Vol. 4502, 74-81 (2001).

15 R. Struik, *Characterisation of XUV Sources*, Technische Universiteit Eindhoven, Eindhoven, 2002.

16 L. Malmqvist, L. Rymell, M. Berglund and H.M. Hertz, "Liquid-jet target for laser-plasma soft x-ray generation", *Rev. Sci. Instrum.* **67**, 4150-4153 (1996).

[17] R. Lebert, G. Schriever, T. Wilhein and B. Niemann, "Soft x-ray emission of laser-produced plasmas using a low-debris cryogenic nitrogen target", *J. Appl. Phys.* **84**, 3419-3421 (1998).

[18] E.A. Gibson, A. Paul, N. Wagner, R. Tobey, D. Gaudiosi, S. Backus, I.P. Christov, A. Aquila, E.M. Gullikson, D.T. Attwood, M.M. Murnana and H.C. Kapteyn, "Coherent soft x-ray generation in the water window with quasi-phase matching", Science **302**, 95-98 (2003).

[19] M. Berglund, L. Rymell, M. Peuker, T. Wilhein and H. M. Hertz, "Compact water-window x-ray microscopy", *J. Microscopy* **197**, 268 (2000).

[20] M. Wieland, R. Frueke, T. Wilhein, C. Spielmann, M. Pohl and U. Kleineberg, "Submicron extreme ultraviolet imaging using high-harmonic radiation", Appl. Phys. Lett. **81**, 2520-2522 (2002).

[21] C. Jacobsen, "Soft x-ray microscopy", *trends Cell Biol.* **9**, 44-47 (1999).

[22] D.T. Attwood, *Soft X-rays And Extreme Ultraviolet Radiation: Principles And Applications*, Cambridge University Press, Cambridge, 2000.

2 Theoretical aspects of Cherenkov radiation

When a relativistic electron is send through a foil, several radiation phenomena occur. In this chapter we concentrate on Cherenkov radiation in the x-ray region. Due to the fact that the Cherenkov radiation is generated in a foil, it is always accompanied by transition radiation, which is generated by the electron at the interfaces of the foil. Therefore, this effect has also to be taken into account in this chapter. All other radiation phenomena, such as fluorescence radiation, Bremsstrahlung and visible transition radiation are discussed in Chapter 4 and Chapter 5 in the context of experiments and in Chapter 6 at the source design, in which the soft x-ray component has to be isolated from the background.

The Cherenkov effect depends strongly on the dielectric constant of a medium, which is discussed extensively in Sec. 2.1 for ultraviolet photon-energies and higher. A simple atomic model is presented that describes the dependence of the dielectric constant on the frequency of the electromagnetic fields, which is called dispersion. Besides being dispersive, a medium is generally absorbing and therefore the dielectric constant is a complex number of which the imaginary part is proportional to the absorption length. Absorption has a particularly strong influence on Cherenkov radiation in the soft x-ray region, since only radiation generated within a few absorption lengths from the surface can exit the material.

In Sec. 2.2 the electromagnetic theory of Cherenkov radiation is treated in some detail. In this chapter the electromagnetic description of purely Cherenkov radiation is presented together with the description of transition radiation, which in principle also includes Cherenkov radiation. In literature, the two radiation phenomena are normally discussed separately. However, in the soft x-ray region, due to the high absorption of materials and the refractive index being close to unity, both are mixed. Therefore, both descriptions are presented together to give a complete picture from a phenomenological and exact point of view.

First, in Sec. 2.2.1 the derivation of the Cherenkov radiation intensity from an infinite medium by Frank and Tamm[1,2,3,4] is followed. This description is in principle only applicable to transparent media, but it has the advantage that it gives adequate physical insight in Cherenkov radiation. This description is applied to the soft x-ray region by taking the absorption into account using a phenomenological approach.

Then, in Sec. 2.2.2 we present an exact and more extensive approach to soft x-ray Cherenkov radiation, which is based on the description of transition radiation that is generated at the interface between the medium and vacuum. For this approach the description by Ginzburg and Frank[3,4,5,6], which is intended for transition radiation, is followed. This exact method confirms the results of the phenomenological approach of Sec. 2.2.1 in the case that transition radiation is negligible compared to Cherenkov radiation. This extensive theoretical description is also essential for the analysis of the experimental results.

The absorption limits the Cherenkov radiation output from a material. There is no use in making the foil any thicker. In Sec. 2.3 grazing-incidence Cherenkov radiation is discussed. This effect has only been experimentally studied before using 75-MeV electrons and in this case the intensity enhancement originates from Cherenkov radiation that is generated just outside the foil. However, using electron energies between 5 and 25 MeV also internal-generated Cherenkov radiation contributes significantly to the radiation output, which we have analyzed in detail.

2.1 Light propagation in a dispersive and absorbing medium

2.1.1 Maxwell's equations and the plane wave solution

Maxwell's equations connect six basic quantities, **B** (magnetic induction), **E** (electric field), **H** (magnetic field), **D** (electric displacement), **J** (electric current density) and ρ (charge density):

$$\nabla \times \mathbf{H} - \frac{\partial \mathbf{D}}{\partial t} = \mathbf{J} , \tag{2.1}$$

$$\nabla \times \mathbf{E} + \frac{\partial \mathbf{B}}{\partial t} = 0 , \tag{2.2}$$

$$\nabla \cdot \mathbf{B} = 0 , \tag{2.3}$$

$$\nabla \cdot \mathbf{D} = \rho . \tag{2.4}$$

The following field relations apply for a linear and isotropic medium,

$$\mathbf{D} = \varepsilon \mathbf{E} , \tag{2.5}$$

$$\mathbf{B} = \mu \mathbf{H} \tag{2.6}$$

with ε the permittivity and μ the magnetic permeability[*]. The permittivity can be expressed as

$$\varepsilon = \varepsilon_0 \varepsilon_r \tag{2.7}$$

with ε_r the dielectric constant (relative permittivity) and ε_0 the permittivity of vacuum. The induced polarization is taken linear with the applied electric field:

---

[*] In the scope of this thesis we deal only with materials of which the magnetic permeability is practically equal to that of vacuum: $\mu \approx \mu_0$.

$$\mathbf{P} = \varepsilon_0 \chi \mathbf{E} \qquad (2.8)$$

with χ the electric susceptibility. Consequently, the dielectric constant is related to the susceptibility by

$$\varepsilon_r = 1 + \chi. \qquad (2.9)$$

Maxwell's equations can be combined to form a vector wave equation describing the propagation of an electromagnetic wave:

$$\left(\nabla^2 - \frac{\varepsilon_r}{c^2} \frac{\partial^2}{\partial t^2} \right) \mathbf{E}(\mathbf{r}, t) = \mu_0 \frac{\partial \mathbf{J}(\mathbf{r}, t)}{\partial t} + \frac{1}{\varepsilon_0 \varepsilon_r} \nabla \rho \qquad (2.10)$$

with $c = \left(\varepsilon_0 \mu_0 \right)^{-1/2}$ the speed of light in vacuum. On the left side the factor ε_r / c^2 is identified as the square of the phase velocity of the wave v_φ of which the value is determined by the dielectric constant:

$$v_\varphi = \frac{c}{\sqrt{\varepsilon_r}} = \frac{c}{n} \qquad (2.11)$$

with $n = \sqrt{\varepsilon_r}$ the index of refraction.

The harmonic plane wave is a well-known homogeneous solution of the wave equation, i.e. with source terms $\mathbf{J}$ and ρ equal to zero:

$$\mathbf{E}(\mathbf{r}, t) = \mathbf{E}_0 e^{-i(\omega t - \mathbf{k} \cdot \mathbf{r})}. \qquad (2.12)$$

By substituting this solution back into the homogenous wave equation and eliminating the exponential the Helmholtz equation is obtained, which can only be satisfied for arbitrary amplitude $\mathbf{E}_0$, if the following dispersion relation is satisfied:

$$\mathbf{k}^2 = \varepsilon_r \frac{\omega^2}{c^2}. \qquad (2.13)$$

A propagating wave in a medium can suffer from absorption. The distance over which the intensity (i.e. $I \propto |\mathbf{E}|^2$) has dropped with $1/e$ is called the absorption length l_{abs}. This linear absorption along the propagation direction z can be accounted for by introducing a complex refractive index $n = n_R + i \cdot n_I$ into Eq. (2.12):

$$E(z, t) = E_0 e^{-i \omega (t - \frac{n_R}{c} z)} e^{-\frac{n_I \omega}{c} z}. \qquad (2.14)$$

The first exponent describes the phase propagation through the medium with the velocity v_φ. The second exponent describes the absorption of the wave through the medium in the direction of propagation with

$$l_{abs} = \frac{c}{2 n_I \omega}. \qquad (2.15)$$

2.1.2   Simple model for dielectric constant

Generally, the value of the dielectric constant depends on the field frequency, which is called dispersion. In this section a simple model[7] of the dielectric constant is presented, which is based on the scattering of electromagnetic plane waves by atomic electrons in the medium [see Fig. 2.1(a)]. The medium is modeled by a vacuum volume containing atomic scatter centers. The atom is represented by a positively charged ($+Ze$) nucleus surrounded by several (Z) electrons. In this model the relatively massive nucleus does not respond dynamically to the high frequency incident fields, but the electrons are caused to oscillate at the frequency ω of the incident field ($\mathbf{E}_i$, $\mathbf{B}_i$) of the passing electromagnetic plane wave. The multi-electron atom is treated as a collection of Z harmonic oscillators, each with its own frequency ω_s, which can be associated in this simple model with the binding energy of the electron s. The equation of motion of an atomic electron can be written as follows:

$$m\frac{d^2\mathbf{x}_s}{dt^2} + m\gamma_s\frac{d\mathbf{x}_s}{dt} + m\omega_s^2\mathbf{x}_s = -e\left(\mathbf{E}_i + \mathbf{v}_s \times \mathbf{B}_i\right) \tag{2.16}$$

with γ_s a damping factor[†] representing the emission of radiation. The magnetic Lorentz force is negligible with respect to the electric force for low enough incident electromagnetic field intensities.
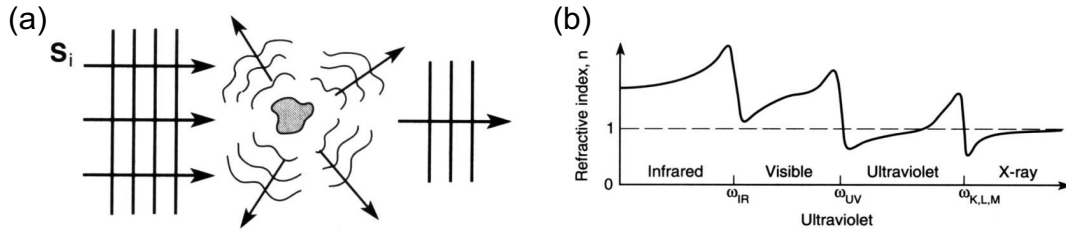
Figure 2.1: (a) Scattering of incident radiation into many directions, leaving a less intense and phase-shifted wave in the forward direction. (b) A sketch of refractive index showing the strong variations near IR, UV, and x-ray resonances (ω_s), and general tendency toward unity for very short wavelengths where the frequencies are higher than all atomic resonances. Only the real part of the refractive index is shown here.

Due to the forced oscillation of the atomic electron it emits dipole radiation, which is the scattered radiation. By evaluating the scattered radiation into the forward direction, the well-known forward scattering amplitude of a multi-electron atom can be derived[7]:

$$E^0(\mathbf{r},t) = -\frac{r_e}{r}f^0(\omega)E_i e^{-i\omega\left(t-\frac{r}{c}\right)} \tag{2.17}$$

with the classical electron radius

[†] Note that the symbol γ only appears in this particular section as the damping factor, while throughout the thesis it will be used as the Lorentz contraction factor.

$$r_e = \frac{e^2}{4\pi\varepsilon_0 mc^2} , \tag{2.18}$$

and with forward scattering factor

$$f^0(\omega) = \sum_s \frac{g_s \omega^2}{\omega^2 - \omega_s^2 + i\gamma_s \omega} , \tag{2.19}$$

which is summed over the individual scatterings by all electrons (total number Z). The coefficients g_s in the forward scattering factor (2.19) are often referred to as oscillator strengths, which in this simple atomic model are integers that indicate the number of electrons associated with a given resonance frequency ω_s. The sum of the oscillators strengths is equal to the total number of electrons in the atom Z.

The propagation of an electromagnetic wave in a medium is described by the forward-scattered radiation from all atoms that interfere with the incident wave to produce a modified propagating wave compared to that in vacuum. As a result, the complex scattering factor can be coupled to the macroscopic parameter: the dielectric constant. This derivation starts from the inhomogeneous wave equation (2.10) in vacuum ($\varepsilon_r = 1$), in which the source terms $\mathbf{J}$ and ρ due to the incident field have to be substituted. For the propagation in the forward direction of a transverse wave $\mathbf{E}_T$ ($\mathbf{E}$ perpendicular to $\mathbf{k}$), the $\nabla\rho$ term and the component of $\mathbf{J}$ in the direction of propagation do not contribute[7]. Therefore, the wave equation (2.10) reduces to

$$\left(\nabla^2 - \frac{1}{c^2}\frac{\partial^2}{\partial t^2} \right)\mathbf{E}_T(\mathbf{r},t) = \mu_0 \frac{\partial \mathbf{J}_T(\mathbf{r},t)}{\partial t} . \tag{2.20}$$

The total current density $\mathbf{J}(\mathbf{r},t)$ is the sum of the contributions of all electrons within an atom and the sum over all atoms. The fact that propagation in the forward direction is considered, simplifies this summation enormously, because the position of the electrons is irrelevant. All atoms contribute identically and the summation is only over the atomic electrons s, that is,

$$\mathbf{J}^0(\mathbf{r},t) = -en_a \sum_s g_s \mathbf{v}_s(\mathbf{r},t) \tag{2.21}$$

with n_a the average atom density containing Z atomic electrons and

$$\mathbf{v}_s(\mathbf{r},t) = \frac{e}{m}\frac{1}{\omega^2 - \omega_s^2 + i\gamma_s \omega}\frac{\partial \mathbf{E}_i(\mathbf{r},t)}{\partial t} . \tag{2.22}$$

By substituting this into the inhomogeneous wave equation (2.20) and reordering the terms to a homogeneous wave equation, one obtains:

$$\left[\left(1 - \frac{e^2 n_a}{\varepsilon_0 m}\sum_s \frac{g_s}{\omega^2 - \omega_s^2 + i\gamma_s \omega} \right)\frac{\partial^2}{\partial t^2} - c^2\nabla^2 \right]\mathbf{E}_T(\mathbf{r},t) = 0 . \tag{2.23}$$

Consequently, the dielectric constant is identified as

$$\varepsilon_r(\omega) \equiv 1 - \frac{e^2 n_a}{\varepsilon_0 m} \sum_s \frac{g_s}{\omega^2 - \omega_s^2 + i\gamma_s\omega} \,, \qquad (2.24)$$

or

$$\varepsilon_r(\omega) \equiv 1 - \frac{e^2 n_a}{\varepsilon_0 m\omega^2} f^0(\omega) \qquad (2.25)$$

with the complex scattering factor $f^0(\omega) = f_1(\omega) + if_2(\omega)$. Because the scattering factor is a complex number, the dielectric constant is written in terms of the complex susceptibility: $\varepsilon_r(\omega) = 1 + \chi'(\omega) + i\chi''(\omega)$.

The dispersion of the dielectric constant in Eq. (2.24) based on this model predicts both positive and negative dispersion [see Fig. 2.1(b)], depending on whether the frequency ω is smaller or larger than the resonance frequency ω_s. In the visible region this is called normal and anomalous dispersion, respectively. For frequencies higher than the highest resonance frequency, the dielectric constant takes on a simple form:

$$\varepsilon_r(\omega) \approx 1 - \frac{\omega_p^2}{\omega^2} \,, \qquad (2.26)$$

in which ω_p is the plasma frequency, defined as

$$\omega_p^2 \equiv \frac{e^2 n_a Z}{\varepsilon_0 m} \,. \qquad (2.27)$$

The plasma frequency is introduced, because the atomic electrons behave like free electrons for frequencies higher than their resonance frequency, i.e. at photon energies that are higher than the binding energy of the electrons. Equation (2.26) shows that the dielectric constant is smaller than unity for high frequencies, typically x-ray photon energies and higher, and approaches unity in the limit.

2.1.3   Tabulated dielectric constant data in the x-ray region

Experimental data of the complex dielectric constant in the x-ray region are scarce. Materials are highly absorbing and therefore it is very difficult to measure phase shifts of radiation transmitted through a sample. At this moment there are two large databases of x-ray atomic scattering factors. First, the Chantler database[8], which is available online at the NIST‡-website, contains mainly calculated data. The stated error in the database is 50%-100% below 200 eV and 20%-50% between 200 eV and 500 eV. Second, the Henke database[9], which is available online at the CXRO§-website, is based on a compilation of photo-absorption measurements of elements in their elemental state and of theoretical calculations. The latter are added because for many elements there are little or no experimental data and in such cases it is necessary to rely on theoretical calculations and interpolations between data of neighboring elements in the periodic system. Both databases have rather large errors around

---

‡ National Institute of Standards and Technology
§ Center for X-Ray Optics of the Lawrence Berkeley National Laboratory

absorption edges. In this thesis we use the Henke database, because it largely based on experimental absorption measurements, which is important for Cherenkov radiation at the soft x-ray edges.

Table 2.1: Table of suitable monochromatic Cherenkov emitters.

Z	Element	Edge	$E_{ph} = \hbar\omega$ [eV]	ΔE^* [eV]	ρ [g/cm^3]	χ'_{max}	$E_{min}^\dagger$ [MeV]	$\theta_{max}^\ddagger$ [deg]	Yield§ [ph/el]
3	Li	K	54.7	1.0	0.534	$6.98 \cdot 10^{-2}$	1.4	14.9	$1.3 \cdot 10^{-2}$
4	Be	K	111.5	0.3	1.848	$5.11 \cdot 10^{-2}$	1.7	12.6	$2.5 \cdot 10^{-3}$
5	B	K	188.0	1.3	2.34	$2.45 \cdot 10^{-2}$	2.8	8.5	$1.5 \cdot 10^{-3}$
6	C	K	284.2	1.0	2.2	$7.64 \cdot 10^{-3}$	5.3	4.2	$4.8 \cdot 10^{-4}$
13	Mg	L$_{II,III}$	49.5	1.1	1.738	$6.59 \cdot 10^{-2}$	1.5	14.4	$5.9 \cdot 10^{-3}$
14	Al	L$_{II,III}$	72.6	1.3	2.699	$7.57 \cdot 10^{-2}$	1.3	15.5	$4.3 \cdot 10^{-3}$
15	Si	L$_{II}$	99.8	1.0	2.33	$4.33 \cdot 10^{-2}$	1.9	11.6	$1.7 \cdot 10^{-3}$
16	P	L$_{III}$	135.0	1.1	2.20	$3.16 \cdot 10^{-2}$	2.4	9.8	$8.0 \cdot 10^{-4}$
17	S	L$_{III}$	162.5	1.5	2.05	$2.78 \cdot 10^{-2}$	2.6	9.1	$1.3 \cdot 10^{-3}$
19	K	L$_{III}$	294.6	1.2	0.862	$4.31 \cdot 10^{-3}$	7.3	2.5	$2.0 \cdot 10^{-4}$
20	Ca	L$_{III}$	346.2	1.6	1.55	$4.92 \cdot 10^{-3}$	6.8	2.9	$2.0 \cdot 10^{-4}$
21	Sc	L$_{III}$	398.7	1.9	2.989	$6.81 \cdot 10^{-3}$	5.7	3.8	$2.6 \cdot 10^{-4}$
22	Ti	L$_{III}$	453.8	2.0	4.54	$7.01 \cdot 10^{-3}$	5.5	3.9	$2.4 \cdot 10^{-4}$
23	V	L$_{III}$	512.1	1.2	6.11	$6.86 \cdot 10^{-3}$	5.7	3.8	$1.2 \cdot 10^{-4}$
24	Cr	L$_{III}$	574.1	1.5	7.19	$6.66 \cdot 10^{-3}$	5.8	3.8	$1.3 \cdot 10^{-4}$
25	Mn	L$_{III}$	638.7	0.5	7.30	$4.88 \cdot 10^{-3}$	6.8	2.9	$3.6 \cdot 10^{-5}$
26	Fe	L$_{III}$	706.8	1.1	7.874	$4.22 \cdot 10^{-3}$	7.4	2.5	$4.9 \cdot 10^{-5}$
27	Co	L$_{III}$	778.1	0.8	8.900	$3.45 \cdot 10^{-3}$	8.2	1.9	$2.1 \cdot 10^{-5}$
28	Ni	L$_{III}$	852.7	0.3	8.902	$2.87 \cdot 10^{-3}$	9.0	1.3	$3.8 \cdot 10^{-6}$
29	Cu	L$_{III}$	932.7	3.3	8.960	$2.43 \cdot 10^{-3}$	9.9	2.6	$1.9 \cdot 10^{-4}$
30	Zn	L$_{III}$	1021.8	1.9	7.133	$1.34 \cdot 10^{-3}$	13.5	1.8	$6.8 \cdot 10^{-5}$
31	Ga	L$_{III}$	1116.4	1.7	6.095	$6.21 \cdot 10^{-4}$	20.0	0.8	$1.6 \cdot 10^{-5}$
32	Ge	L$_{III}$	1217.0	0.6	5.323	$5.09 \cdot 10^{-4}$	22.1	0.6	$3.7 \cdot 10^{-6}$

Note: $Z \leq 28$ 10-MeV electrons are used; $Z > 28$ 25-MeV electrons are used.

*: ΔE is the FWHM; †: E_{min} is given by Cherenkov condition: $\gamma^2 = \chi_{max}'$; ‡: $\theta_{max} = \sqrt{(\chi' - \gamma^2)}$; §: Yield is integral of Eq. (2.59) over photon energy.

In Fig. 2.2 the complex atomic scattering factor of silicon is plotted, as is given in both databases. In the imaginary part clearly the L$_{II,III}$-edge (at 99.7 eV) and the K-edge (at 1.838 keV) are visible. The Henke database shows much more detail at the L-edge than the Chantler database. In the real part the resonances that are associated with the absorption edges, are

visible. These resonances can be so strong that the real part of the scattering factor becomes negative, e.g. at the $L_{II,III}$-edge of silicon. Far from resonance the real part of the scattering factor will approach the value of the number of atomic electrons $Z_<$ with a binding energy smaller than the photon energy [see Eq. (2.19)]. The dashed curve indicates the value of $Z_<$.
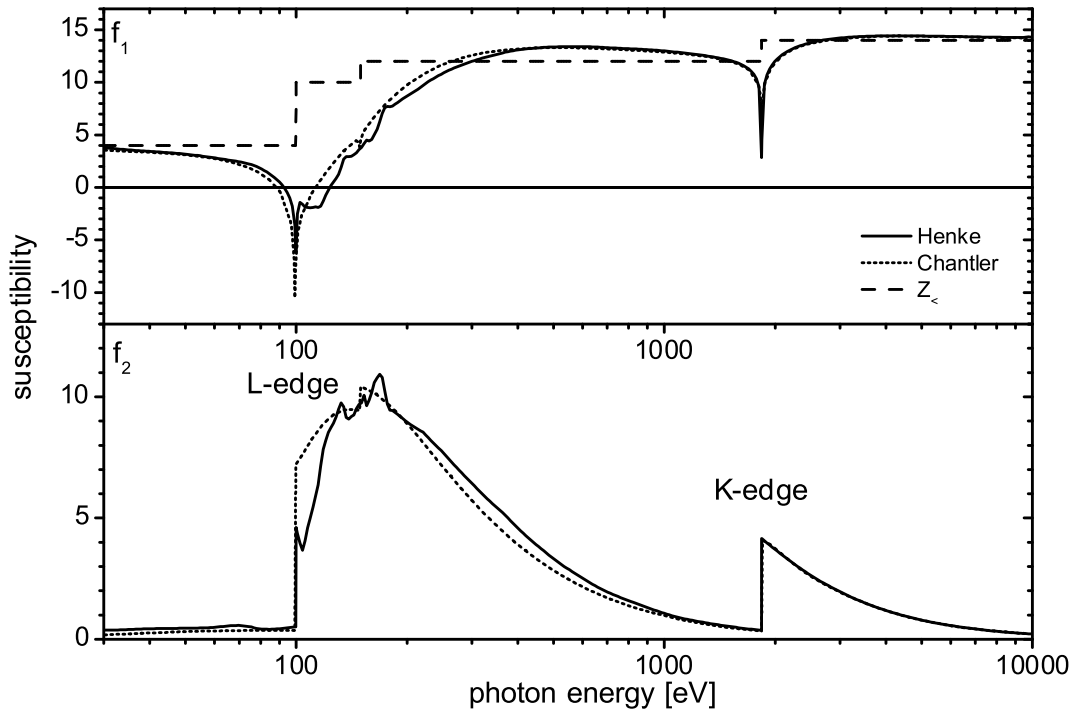
Figure 2.2: Scattering factor of silicon taken from the Henke database (solid curve) and Chantler database (dotted curve). The simple model (dashed curve) indicates $Z_<$.

The regions of anomalous dispersion are essential for the generation of Cherenkov radiation in the x-ray region. The Cherenkov condition requires a negative value of the real part of the scattering factor, because then the real part of the dielectric constant is larger than unity. In an article by Smith and Barkyoumb[10] such strong resonances are discussed. They discuss the conditions that determine whether elements will show sign change of the real part of the scattering factor in the x-ray region. First, an element should have a strong absorption edge with a sharp onset. This condition does not favor edges originating from levels with only a few electrons, especially s-like levels with two electrons like for instance K-, L_I- and M_I-edges. More likely candidates are $L_{II,III}$ and $M_{IV,V}$-edges, which involve a large number of electrons. A possible exception may be K-edges in the second-period elements, which lack a well-developed L-shell. Second, the edge must be sufficient isolated such that the high-energy absorption tails belonging to lower-energy edges are small at the edge. Otherwise, the step at the edge is not large enough and not sufficiently steep to induce a strong anomalous dispersion. Third, absorptions at lower energies must have sufficiently low total oscillator strength. This condition does not favor 3d-transition metals in which a strong, broad M-shell absorption extends throughout the extreme ultraviolet. These conditions suggest that the $L_{II,III}$-edges of the third-period elements such as Si, Al and P, are among the most favorable

candidates for sign change of the real part of the scattering factor. Other possible candidates are isolated $M_{IV,V}$-edges of fourth-period elements and K-edges of second-period elements.

Starting from the above predictions for favorable elements we used the Henke database to select suitable elements for line-like Cherenkov emission. The refractive index must be sufficiently larger than unity to get significant yield. Therefore, solid-state materials are preferred, because the deviation of the refractive index from unity is proportional to the density of the material [see Eq. (2.25)]. It appears that K-edges of second period elements and L_{III}-edges of third-period elements with atomic numbers lower than 30 are suitable candidates for generating narrowband Cherenkov radiation. In Table 2.1 a summary is given of the Cherenkov radiation properties of these elements. As can be seen from this table, all Cherenkov photon energies lie within the soft x-ray region (30 eV – 1 keV) and can be generated by electrons of moderate energy (lower than 25 MeV). In the Henke database the refractive index of more high-Z elements (e.g. Fe, Cr at their M-edge) also exceed unity, but these resonances are much broader and are therefore not suitable for narrowband soft x-ray Cherenkov sources.

2.2 Theory of Cherenkov radiation

2.2.1 Simple theory of Cherenkov radiation

The first observations of "Cherenkov" radiation date back to 1934, when Cherenkov published an article[11] about the observation of a faint light in solvents caused by gamma rays from radium. After the characteristic forward direction of the emission with respect to the gamma ray beam was observed in 1936[12], Frank and Tamm formulated a theory[1] in 1937 that explained the observed phenomenon. This light is produced by electrons traveling uniformly at a speed exceeding the phase velocity of light in that medium. It is an interesting fact that as early as 1901, Lord Kelvin[13] maintained that emission of radiation was possible at a particle speed greater than that of light. Somewhat later, in 1904 to 1905, shortly before the theory of relativity was formulated, Sommerfeld theoretically established the hypothetical case of an electron moving at a speed greater than that of light in vacuum[14,15]. After the theory of relativity was accepted, the findings of Sommerfeld were overshadowed and forgotten.

Nowadays, Cherenkov radiation is widely used in high-energy particle detectors. These detectors operate in the visible region of the spectrum. Cherenkov radiation in the x-ray region was excluded ever since the discovery of the phenomenon, because the refractive index in this spectral region is generally smaller than unity. Although it was known that regions of anomalous dispersion should exist in the x-ray region, observable Cherenkov radiation at a reasonable distance from the particle trajectory was excluded due to high absorption in the x-ray region. Until recently, Cherenkov radiation in these regions has therefore only been considered as a source of energy loss of the particle[16].

In 1981 Bazylev *et al.*[17] were the first to realize that x-ray Cherenkov radiation, which is generated in the spectral regions of anomalous dispersion, should be observable for certain material properties. Their conclusion was based on detailed absorption measurements from which the real part of the dielectric constant can be calculated using the Kramers-Kronig

relations. These calculations show that in small spectral regions at absorption edges the real part of the dielectric constant exceeds unity, leading to observable Cherenkov radiation outside the material.

The theoretical description of Cherenkov radiation in this thesis follows first the Frank-Tamm approach (Sec. 2.2.1.1), which assumes a charged, point-like particle, traveling with a constant velocity through a uniform and isotropic dielectric medium with a real dielectric constant $\varepsilon_r(\omega)$. This electromagnetic theory has a few simplifying assumptions: (i) radiation recoil of the particle is neglected, (ii) there is no slowing down of the particle due to energy loss, (iii) Coulomb scattering of the particle is ignored, (iv) there is no absorption of the emitted radiation and (v) the medium is unbounded. Quantum mechanical calculations using energy and momentum conservation show that assumption (i) is correct for photon energies much lower than the kinetic energy of the particle. Assumption (ii) and (iii) are satisfied when Cherenkov radiation is generated in a thin foil. Assumption (iv) is not fulfilled in the soft x-ray region and is therefore first phenomenologically addressed in Sec. 2.2.1.2 and then treated exactly in Sec. 2.2.2. In the latter the Cherenkov radiation is described by following the Ginzburg-Frank approach, which also treats exactly the boundary of the foil that is excluded by assumption (v) in the first approach.
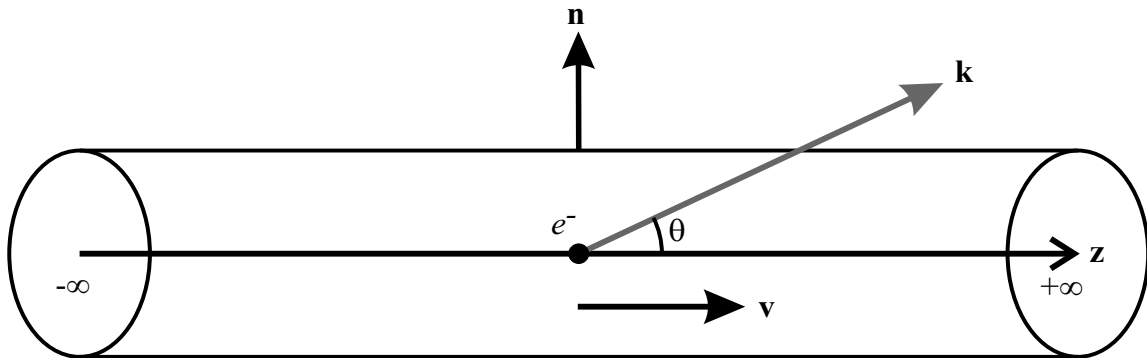
Figure 2.3: Cherenkov geometry: An electron travels with velocity v along the z-axis from $-\infty$ to $+\infty$ emitting Cherenkov radiation with wave vector **k** at an angle θ with respect to the electron trajectory. The radiated Cherenkov energy per unit length is integrated over the cylindrical interface with normal unit vector **n**.

2.2.1.1 Frank-Tamm approach

The description of Cherenkov radiation by Frank and Tamm starts by solving the field of a charged particle moving at a constant velocity from $z = -\infty$ to $+\infty$ in a dielectric medium, as is shown in Fig. 2.3. Therefore, the wave equations are written in terms of the potentials **A** and Φ, which are defined by

$$\mathbf{B} = \nabla \times \mathbf{A}, \tag{2.28}$$

$$\mathbf{E} = -\nabla \Phi - \frac{\partial \mathbf{A}}{\partial t}, \tag{2.29}$$

using the Lorentz condition

$$\nabla \cdot \mathbf{A} + \frac{\varepsilon_r}{c^2} \frac{\partial \Phi}{\partial t} = 0 . \tag{2.30}$$

As a result the potential wave equations are obtained:

$$\nabla^2 \mathbf{A} - \frac{\varepsilon_r}{c^2} \frac{\partial^2 \mathbf{A}}{\partial t^2} = -\mu_0 \mathbf{J} , \tag{2.31}$$

$$\nabla^2 \Phi - \frac{\varepsilon_r}{c^2} \frac{\partial^2 \Phi}{\partial t^2} = -\frac{\rho}{\varepsilon_0 \varepsilon_r} . \tag{2.32}$$

To deal with the frequency dependence of $\varepsilon_r(\omega)$ the potentials are Fourier-transformed from t-space to ω-space:

$$\mathbf{A}_\omega(\mathbf{r}) = \frac{1}{\sqrt{2\pi}} \int_{-\infty}^{+\infty} \mathbf{A}(\mathbf{r},t) e^{i\omega t} dt , \tag{2.33}$$

$$\Phi_\omega(\mathbf{r}) = \frac{1}{\sqrt{2\pi}} \int_{-\infty}^{+\infty} \Phi(\mathbf{r},t) e^{i\omega t} dt . \tag{2.34}$$

Then, the potential wave equations (2.31) and (2.32) are transformed into the Helmholtz wave equations by applying the Fourier transform:

$$\nabla^2 \mathbf{A}_\omega + \frac{\varepsilon_r}{c^2} \omega^2 \mathbf{A}_\omega = -\mu_0 \mathbf{J}_\omega , \tag{2.35}$$

$$\nabla^2 \Phi_\omega + \frac{\varepsilon_r}{c^2} \omega^2 \Phi_\omega = -\frac{\rho_\omega}{\varepsilon_0 \varepsilon_r} . \tag{2.36}$$

In these equations the proper functions of the charge and current density due to the charged particle (q) moving with velocity $\mathbf{v}$ have to be introduced:

$$\rho(\mathbf{r},t) = q\delta(\mathbf{r} - \mathbf{v}t) , \tag{2.37}$$

$$\mathbf{J}(\mathbf{r},t) = q\mathbf{v}\delta(\mathbf{r} - \mathbf{v}t) . \tag{2.38}$$

Only the vector potential wave equation (2.35) is solved and then the scalar potential Φ is obtained from the Lorentz condition (2.30). Because the particle moves along the z-axis, the current density as well as the vector potential only have a z-component: $\mathbf{J}_z = J_z \mathbf{e}_z$ and $\mathbf{A}_z = A_z \mathbf{e}_z$ [see Eq. (2.35)]. The Fourier component $J_{z,\omega}(\mathbf{r})$, which is defined like Eq. (2.33), is given by

$$J_{z,\omega}(\mathbf{r}) = q \frac{\delta(x)\delta(y)}{\sqrt{2\pi}} e^{i\omega\frac{z}{v}} . \tag{2.39}$$

This solution can be introduced into the vector potential wave equation (2.35). By transforming to cylindrical coordinates and introducing a forced oscillation solution of the vector potential $A_{z,\omega}(r,z) = u(r)e^{i\omega z/v}$, the wave equation takes the shape of a Bessel equation:

$$\frac{\partial^2 u(r)}{\partial r^2} + \frac{1}{r}\frac{\partial u(r)}{\partial r} + s^2 u(r) = -\mu_0 q \frac{\delta(r)}{(2\pi)^{3/2} r} \tag{2.40}$$

with

$$s^2 = \omega^2 \left(\frac{\varepsilon_r}{c^2} - \frac{1}{v^2} \right). \tag{2.41}$$

The solution of the Bessel equation (2.40) depends on the sign of the quantity s^2. First, in case of $s^2 < 0$, which occurs when $v^2 < c^2/\varepsilon_r$, the wave equation takes the form of the modified Bessel equation with σ a real quantity that is defined as $\sigma^2 = -s^2$. The solution of the homogeneous modified Bessel equation[18] is the modified Bessel function $K_0(\sigma r)$, which can be expressed in terms of the Hankel function of the first kind $H_0^{(1)}$. The solution is normalized[19] to satisfy the inhomogeneous Bessel equation (2.40) at $r = 0$ by performing a surface integration and taking the limit for $r \to 0$. The solution is given by

$$u(r) = \frac{i\mu_0 q}{4\sqrt{2\pi}} H_0^{(1)}(i\sigma r). \tag{2.42}$$

In the far-field, i.e. $\sigma r \gg 1$, this solution represents an exponentially decaying amplitude of the potential $A_{z,\omega}(r,z)$. Therefore, at large distances no radiation is observed.

Second, in case of $s^2 > 0$, which occurs when $v^2 > c^2/\varepsilon_r$ (which is called the Cherenkov condition), the normal Bessel equation is obtained. The general homogeneous solution is the Hankel function of either the first or the second kind[18]. In the far field, $sr \gg 0$, these functions represent propagating waves of which the direction depends on the Fourier definition [see Eq. (2.33)]. In our case $H_0^{(1)}$ and $H_0^{(2)}$ are outgoing and ingoing waves, respectively. After normalization[19] the solution is given by

$$u(r) = \frac{i\mu_0 q}{4\sqrt{2\pi}} H_0^{(1)}(sr). \tag{2.43}$$

In the far-field $sr \gg 1$, a propagating potential wave is obtained:

$$A_{z,\omega}(r,z) = \frac{\mu_0 q}{4\pi\sqrt{sr}} e^{i(sr + \frac{\omega}{v}z + \frac{1}{4}\pi)}. \tag{2.44}$$

When the phase factor of Eq. (2.44) is put equal to the phase factor of a freely propagating wave: $i(rs + z\omega/v) = i\mathbf{k} \cdot \mathbf{r} = ik(r\sin\theta + z\cos\theta)$ with $k^2 = \varepsilon_r \omega^2/c^2$, it becomes immediately clear that the wave propagates at an angle with respect to the electron trajectory that is given by the Cherenkov angular relation:

$$\cos\theta = \frac{c}{v\sqrt{\varepsilon_r}}. \tag{2.45}$$

The electric and magnetic fields of the emitted radiation can be derived from the vector potential by using the Eqs. (2.28)-(2.30). Only the terms that decay slowly enough as a function of r are taken into account:

$$B_{\varphi,\omega}(r,z) = -\frac{i\mu_0 q\sqrt{s}}{4\pi\sqrt{r}} e^{i(\sqrt{\varepsilon_r}\frac{\omega}{c}(r\sin\theta + z\cos\theta) + \frac{\pi}{4})}, \tag{2.46}$$

$$E_{z,\omega}(r,z) = \frac{i\mu_0 q}{4\pi\sqrt{sr}}\left(1 - \frac{1}{\varepsilon_r\beta^2}\right)\omega e^{i(\sqrt{\varepsilon_r}\frac{\omega}{c}(r\sin\theta + z\cos\theta) + \frac{\pi}{4})}, \tag{2.47}$$

$$E_{r,\omega}(r,z) = -\frac{i\mu_0 q\sqrt{s}c^2}{4\pi\sqrt{r}\varepsilon_r v} e^{i(\sqrt{\varepsilon_r}\frac{\omega}{c}(r\sin\theta + z\cos\theta) + \frac{\pi}{4})}. \tag{2.48}$$

The total energy W radiated by the charged particle is the integral of the Poynting vector **S** over a cylindrical surface around the trajectory and over time (see Fig. 2.3):

$$W = 2\pi r \int\limits_{-\infty}^{+\infty} dz \int\limits_{-\infty}^{+\infty} dt\, \mathbf{S}(\mathbf{r},t)\cdot\mathbf{n}. \tag{2.49}$$

The Poynting vector perpendicular to the cylindrical surface can be expressed in the electrical field E_z and magnetic field B_φ:

$$\mathbf{S}(\mathbf{r},t)\cdot\mathbf{n} = \frac{1}{\mu_0}E_z(\mathbf{r},t)B_\varphi(\mathbf{r},t), \tag{2.50}$$

or

$$\mathbf{S}(\mathbf{r},t)\cdot\mathbf{n} = \frac{1}{\mu_0}\frac{1}{2\pi}\int d\omega\int d\omega' E_{z,\omega}(r,z)B_{\varphi,\omega}(r,z)e^{i(\omega+\omega')t} \tag{2.51}$$

After substituting Eq. (2.51) in Eq. (2.49) and performing the integration over time t and frequency ω', the radiated energy is expressed per unit path length and per unit frequency interval, which is the well-known Frank-Tamm equation:

$$\frac{d^2W}{d\omega dz} = \frac{q^2}{4\pi\varepsilon_0 c^2}\left(1 - \frac{c^2}{\varepsilon_r v^2}\right)\omega. \tag{2.52}$$

By dividing Eq. (2.52) by the photon energy $\hbar\omega$, the spectral yield, i.e. the number of photons N emitted per electron ($q = -e$), per unit frequency interval and per unit path length, is obtained

$$\frac{d^2N}{d\omega dz} = \frac{\alpha}{c}\left(1 - \frac{c^2}{v^2\varepsilon_r}\right), \tag{2.53}$$

with the fine structure constant $\alpha = e^2/4\pi\varepsilon_0\hbar c \approx 1/137$ and e the elementary charge. By substituting Eq. (2.45) in Eq. (2.53), the Cherenkov spectral yield can also be expressed in terms of emission angle θ:

$$\frac{d^2N}{d\omega dz} = \frac{\alpha}{c}\sin^2\theta. \tag{2.54}$$

Note, that the angle θ is a function of frequency due to the frequency dependence of the dielectric constant.

2.2.1.2   Cherenkov radiation in the soft x-ray region

In the soft x-ray region the dielectric constant is a complex number with the real part close to unity and the imaginary part describing the absorption. Soft x-ray Cherenkov radiation is however not simply calculated by substituting the complex dielectric constant in the Frank-Tamm equation (2.52), because strictly speaking this equation only holds for transparent media. In this section a phenomenological approach is presented in which the generation and absorption of Cherenkov radiation is separated. First, the generation is discussed for real $\varepsilon_r \approx$ 1, i.e. $\chi' \ll 1$. Then, the absorption is taken into account separately.

Because the dielectric constant is close to unity, the Cherenkov condition is only fulfilled if the speed of the charged particle is close to the speed of light in vacuum c. This favors using electrons, because it requires a relatively small amount of energy to accelerate them to relativistic velocities. The speed of the electron can be expressed in terms of the relative velocity $\beta = v/c$, or, alternatively, in terms of the Lorentz contraction factor

$$\gamma \equiv \frac{1}{\sqrt{1-\beta^2}} = 1 + \frac{E_{kin}}{E_0} \tag{2.55}$$

with $E_0 = m_0 c^2 = 0.511$ MeV for electrons.
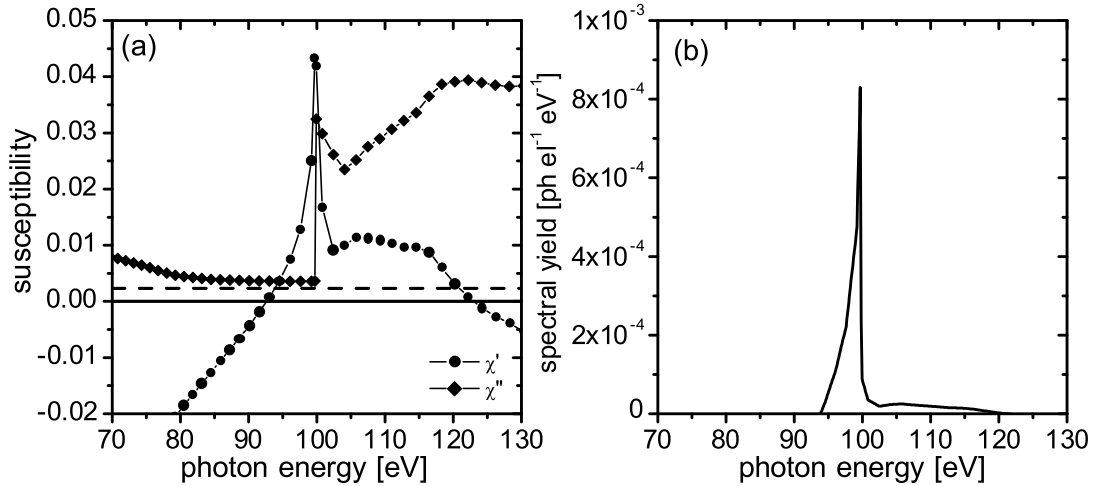
Figure 2.4: (a) Complex susceptibility of silicon around the L-edge. The dashed curve indicates the Cherenkov condition for 10-MeV electrons. (b) The spectral Cherenkov yield calculated with the Frank-Tamm equation (2.59).

By substituting the Lorentz contraction factor (2.55) and the (real) susceptibility χ' [see Eq. (2.9)] into the Cherenkov angle (2.45) and taking $\gamma^{-2} \ll 1$ and $\chi' \ll 1$, the small angle approximation is obtained:

$$\theta = \sqrt{\chi' - \gamma^{-2}} \ . \tag{2.56}$$

In this equation the Cherenkov condition is expressed by $\chi' - \gamma^{-2} > 0$. The spectral Cherenkov yield is obtained by substituting the Cherenkov angle approximation (2.56) into Eq. (2.54):

$$\frac{d^2 N}{d\omega dz} = \frac{\alpha}{c}\left(\chi' - \gamma^{-2}\right). \tag{2.57}$$

The total yield N (photons per electron) is proportional to the area under the curve $\chi' - \gamma^{-2}$ [e.g. Fig. 2.4(a)] and to the path length through the medium.
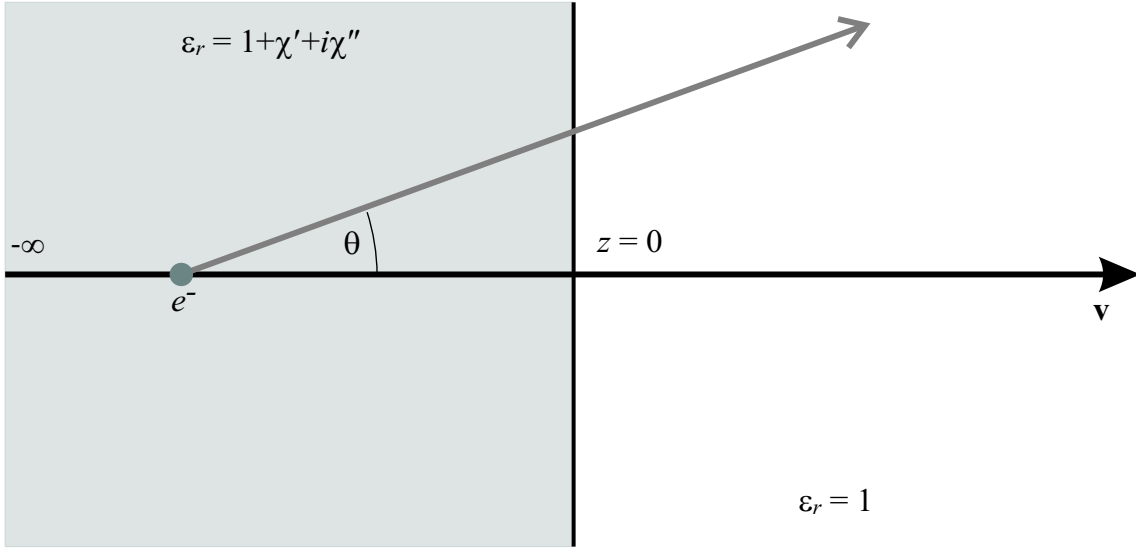
Figure 2.5: An electron with velocity v passes from an absorbing medium with a complex dielectric constant into vacuum. Cherenkov intensity generated at a depth $-z$ in an absorbing medium will decay on the way to the surface.

The latter does not hold for an absorbing medium, where the generated photons can be re-absorbed by the medium before reaching the surface (see Fig. 2.5). Therefore, the spectral yield exiting the material from a depth $-z$ in the material is the yield of Eq. (2.57) times an exponential decay factor characterized by the absorption length l_{abs}:

$$\frac{dN}{d\omega} = \frac{\alpha}{c}\left(\chi' - \gamma^{-2}\right)\int_{-\infty}^{0} e^{\frac{z}{l_{abs}}\frac{1}{\cos\theta}} dz. \tag{2.58}$$

The cosine term is in small-angle approximation equal to unity and the absorption length (2.15) is in approximation equal to $l_{abs} \approx c/\omega\chi''$. As a result the observable Cherenkov radiation emerging from the material is given by

$$\frac{dN}{d\omega} = \frac{\alpha}{\omega}\frac{\chi' - \gamma^{-2}}{\chi''}. \tag{2.59}$$

Equation (2.59) shows the condition for Cherenkov radiation in the soft x-ray region: The spectral yield is high when $\chi' - \gamma^{-2} \gg \chi''$. From the anomalous dispersion at the absorption edge [see Fig. 2.4(a)] can be concluded that this is mainly fulfilled at the low-energy side of the absorption edge.

2.2.1.3   Characteristics of soft x-ray Cherenkov radiation

The special characteristics of Cherenkov radiation in the soft x-ray region, which are already summarized in Sec. 1.3, can now be based on Eq. (2.59).

(i) The Cherenkov radiation is characterized by a narrow bandwidth. The real part of the susceptibility χ' exceeds unity only in a narrow spectral region. The step in the imaginary part of the susceptibility χ'' narrows the Cherenkov spectrum even further to mainly the part at the low photon-energy side of the edge. Typically, the Cherenkov spectrum has a FWHM-width of a few electron-volts.

(ii) Equation (2.56) shows that the maximum emission angle is given by $\theta_{max} = \sqrt{\chi'_{max}}$, which is typically a few degrees. The Cherenkov radiation is therefore emitted in a narrow, forward-directed, angular profile. This angular profile is a hollow cone, because the spectral angular Cherenkov intensity (2.59) is proportional to the emission angle squared and therefore zero for $\theta = 0°$.

(iii) The Cherenkov condition ($\chi' - \gamma^{-2} > 0$) in Eq. (2.59) shows that the minimal Lorentz contraction factor required is $\gamma_{min} = 1/\sqrt{\chi'_{max}}$, which is typically in the range between 10 and 50, which corresponds to 5 and 25 MeV. Such energies can be generated with compact accelerators. Much higher electron energies are not necessary, because the Cherenkov spectral yield saturates for electron energies with 2 or 3 times γ_{min}.

These characteristics are illustrated with silicon of which the complex susceptibility around the L-edge ($\hbar\omega = 99.7$ eV) and the corresponding spectral yield calculated by Eq. (2.59) are plotted in Fig. 2.4(a) and 2.4(b), respectively. In Table 2.1 Cherenkov radiation properties are specified for all materials that have been selected in Sec. 2.1.3 as suitable Cherenkov emitters.

2.2.2   Extensive theory of Cherenkov radiation

2.2.2.1   Transition radiation

From the discussion in the previous section we have seen that a charged particle, which travels at a constant velocity smaller than the phase velocity of light through a medium, does not radiate. However, if a uniformly moving charged particle crosses the interface of two media with different refractive indices, there appears transition radiation. This radiation is produced because of the jump in the phase velocity of light at the interface of two media. When it is in the first medium and far from the interface, the Coulomb field of the particle has a shape that is determined by the particles velocity and by that medium. Later, when it is deep in the second medium, it has a Coulomb fields corresponding to its motion in that medium. Even if the motion is uniform throughout, the initial and final fields will be different if the two media have different electromagnetic properties. Evidently the fields must reorganize themselves as the particle passes through the interface. In this process of reorganization some energy of the particle field is lost into radiation, which is known as transition radiation.

This phenomenon is to some extent analogue to Bremsstrahlung that appears because of the jump in velocity of the particle. The similarity with Bremsstrahlung becomes complete in an extreme case, when the particle moves from vacuum into a perfect conductor. The intensity

of the transition radiation is at its maximum in this case and the radiation pulse is then exactly identical to that produced by two particles of opposite charge, which are moving towards each other and which are stopped instantaneously at the point of encounter.

Cherenkov radiation and transition radiation are both radiation phenomena determined by the dielectric constant value of media. Since in practice Cherenkov radiation is generated in a finite medium it is always accompanied by transition radiation, generated at the interface where the charged particle enters or leaves the medium. First, in Sec. 2.2.2.2 the intensity of Cherenkov radiation is presented following the description of Ginzburg and Frank[3,5,6], which is originally intended for transition radiation. Then, in Sec. 2.2.2.3 it is shown that the absorption of the soft x-ray region appears naturally in this derivation. When transition radiation is negligible compared to Cherenkov radiation, for instance at the low photon-energy side of an absorption edge, the equations of the simple Cherenkov radiation theory in Sec. 2.2.1.2 are retrieved.
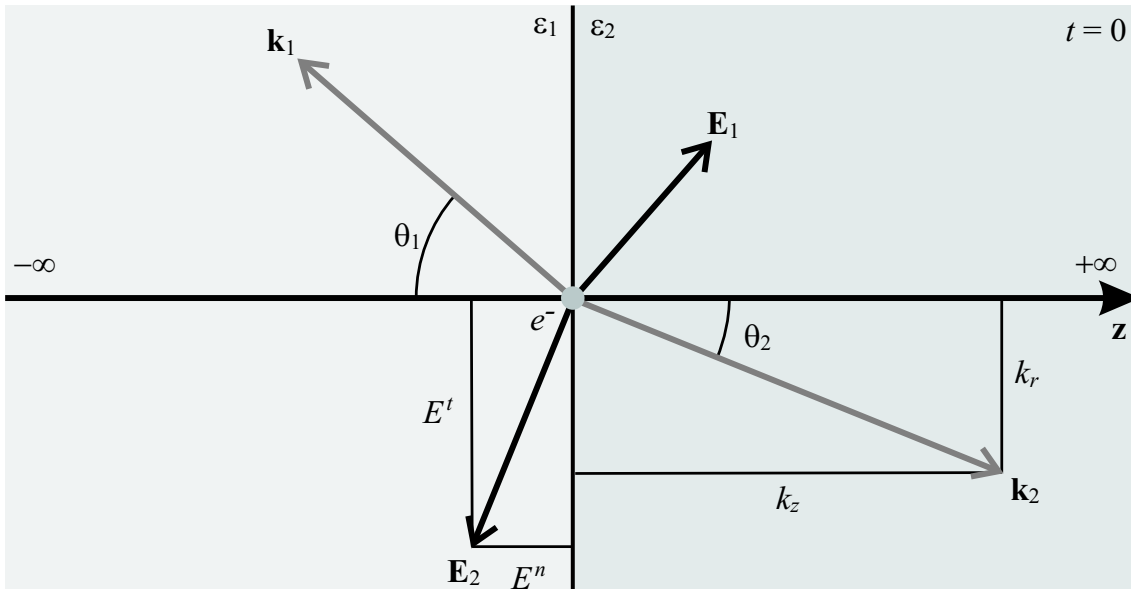
Figure 2.6: A charged particle passes an interface at $z = 0$ and at $t = 0$. Boundary conditions at $z = 0$ have to be satisfied for the field components normal and parallel to the interface.

2.2.2.2   Ginzburg-Frank approach

Consider a charged, point-like particle traveling from $z = -\infty$ to $+\infty$ with constant speed that passes at time $t = 0$ an interface at $z = 0$ between two semi-infinite dielectric media (see Fig. 2.6). Again we make the simplifying assumptions that the recoil of the radiation and elastic scattering are negligible. The derivation starts similar to the description of Cherenkov radiation by Frank and Tamm in Sec. 2.2.1.1, but the Fourier transformation [see Eq. (2.33)] is extended to also the **k**-space:

$$\mathbf{A}_{\omega,\mathbf{k}} = \frac{1}{(2\pi)^2} \int\int \mathbf{A}(\mathbf{r},t) e^{i(\omega t - \mathbf{k}\cdot\mathbf{r})} dt d\mathbf{r} , \qquad (2.60)$$

$$\Phi_{\omega,\mathbf{k}} = \frac{1}{(2\pi)^2} \int\int \Phi(\mathbf{r},t) e^{i(\omega t - \mathbf{k}\cdot\mathbf{r})} dt d\mathbf{r} \ . \tag{2.61}$$

From the Fourier-transformed, inhomogeneous wave equations, with $\mathbf{A}_{\omega,k} = A_{z,\omega,k}\mathbf{e}_z$,

$$k^2 A_{z,\omega,\mathbf{k}} - \frac{\varepsilon_r \omega^2}{c^2} A_{z,\omega,\mathbf{k}} = \frac{\mu_0 q}{2\pi} \delta(k_z - \frac{\omega}{v}) \ , \tag{2.62}$$

$$k^2 \Phi_{\omega,\mathbf{k}} - \frac{\varepsilon_r \omega^2}{c^2} \Phi_{\omega,\mathbf{k}} = \frac{q}{2\pi\varepsilon_0\varepsilon_r v} \delta(k_z - \frac{\omega}{v}) \ , \tag{2.63}$$

the potentials can be determined and the electric field of the charged particle is obtained by substituting these potentials into the Lorentz condition (2.30),

$$\mathbf{E}^q_{\omega,\mathbf{k}} = \frac{iq}{2\pi\varepsilon_0 v}\left(\frac{\omega}{c^2}v\mathbf{e}_z - \frac{1}{\varepsilon_r}\mathbf{k}\right)\frac{\delta(k_z - \frac{\omega}{v})}{\mathbf{k}^2 - \varepsilon_r\frac{\omega^2}{c^2}} \tag{2.64}$$

with $\varepsilon_r = \varepsilon_i$ the dielectric constant in medium i. This field is the inhomogeneous solution of the wave equation. The total field $\mathbf{E}$ at both sides of the interface is the sum of the inhomogeneous solution $\mathbf{E}^q$, which is the field of the charged particle [Eq. (2.64)], and the homogeneous solution $\mathbf{E}^{ph}$, which is a propagating plane wave,

$$\mathbf{E}^{ph}_{\omega,\mathbf{k}} = \boldsymbol{\mathcal{E}}_{\omega,\mathbf{k}} \delta(\mathbf{k}^2 - \varepsilon_r \frac{\omega^2}{c^2}) \ . \tag{2.65}$$

The transverse component of $\mathbf{E}$, i.e. E_r, and the normal component of $\mathbf{D}$, i.e. D_z, have to be continuous at the interface at $z = 0$,

$$\int (E^{1,q}_{r,\omega,\mathbf{k}} + E^{1,ph}_{r,\omega,\mathbf{k}}) e^{i(\omega t - \mathbf{k}\cdot\mathbf{r})} d\omega d\mathbf{k}\Big|_{z=0} = \int (E^{2,q}_{r,\omega,\mathbf{k}} + E^{2,ph}_{r,\omega,\mathbf{k}}) e^{i(\omega t - \mathbf{k}\cdot\mathbf{r})} d\omega d\mathbf{k}\Big|_{z=0} \ , \tag{2.66}$$

$$\int \varepsilon_1 (E^{1,q}_{z,\omega,\mathbf{k}} + E^{1,ph}_{z,\omega,\mathbf{k}}) e^{i(\omega t - \mathbf{k}\cdot\mathbf{r})} d\omega d\mathbf{k}\Big|_{z=0} =$$

$$\int \varepsilon_2 (E^{2,q}_{z,\omega,\mathbf{k}} + E^{2,ph}_{z,\omega,\mathbf{k}}) e^{i(\omega t - \mathbf{k}\cdot\mathbf{r})} d\omega d\mathbf{k}\Big|_{z=0} \ . \tag{2.67}$$

Additionally, the radiation field $\mathbf{E}^{ph}$, which is the homogeneous solution of the wave equation, has to satisfy Eq. (2.4) in each medium,

$$\nabla \cdot \mathbf{E}^{i,ph} = \frac{\partial}{\partial r} E^{i,ph}_r + \frac{\partial}{\partial z} E^{i,ph}_z = 0 \ , \tag{2.68}$$

or

$$\mathbf{k}_i \cdot \mathbf{E}^{i,ph}_{\omega,\mathbf{k}} = k_r E^{i,ph}_{r,\omega,\mathbf{k}} + k^i_z E^{i,q}_{z,\omega,\mathbf{k}} = 0 \tag{2.69}$$

with k_r the transverse or radial component and k_z the normal component of $\mathbf{k}$ with respect to the interface. The k_r component is equal in both media. The absolute value of k_z is defined as κ:

$$\kappa_i = \sqrt{\varepsilon_i \frac{\omega^2}{c^2} - k_r^{\,2}} \ . \tag{2.70}$$

By substituting the radiation electric field (2.65) into the set of equations (2.66-2.69) and performing the integration over dk_z, the field amplitudes $\mathcal{E}^1_{z,\omega,\mathbf{k}}$, $\mathcal{E}^2_{z,\omega,\mathbf{k}}$, $\mathcal{E}^1_{r,\omega,\mathbf{k}}$ and $\mathcal{E}^2_{r,\omega,\mathbf{k}}$ can be solved as a function of θ_i,

$$\mathcal{E}^1_{z,\omega,\mathbf{k}} = \frac{iq}{\pi\varepsilon_0 v} \frac{\kappa_1 k_r^{\,2}}{(\varepsilon_1\kappa_2 + \varepsilon_2\kappa_1)} \left(\frac{\dfrac{\varepsilon_2}{\varepsilon_1} - \dfrac{v}{\omega}\kappa_2}{\dfrac{\omega^2}{v^2} + k_r^{\,2} - \dfrac{\omega^2}{c^2}\varepsilon_1} + \frac{\dfrac{v}{w}\kappa_2 - 1}{\dfrac{\omega^2}{v^2} + k_r^{\,2} - \dfrac{\omega^2}{c^2}\varepsilon_2} \right), \tag{2.71}$$

$$\mathcal{E}^1_{r,\omega,\mathbf{k}} = \frac{\kappa_1}{k_r} \mathcal{E}^1_{z,\omega,\mathbf{k}}, \tag{2.72}$$

$$\mathcal{E}^2_{z,\omega,\mathbf{k}} = -\frac{iq}{\pi\varepsilon_0 v} \frac{\kappa_2 k_r^{\,2}}{(\varepsilon_1\kappa_2 + \varepsilon_2\kappa_1)} \left(\frac{\dfrac{\varepsilon_1}{\varepsilon_2} + \dfrac{v}{\omega}\kappa_1}{\dfrac{\omega^2}{v^2} + k_r^{\,2} - \varepsilon_2\dfrac{\omega^2}{c^2}} - \frac{\dfrac{v}{w}\kappa_1 + 1}{\dfrac{\omega^2}{v^2} + k_r^{\,2} - \dfrac{\omega^2}{c^2}\varepsilon_1} \right), \tag{2.73}$$

$$\mathcal{E}^2_{r,\omega,\mathbf{k}} = -\frac{\kappa_2}{k_r} \mathcal{E}^2_{z,\omega,\mathbf{k}}, \tag{2.74}$$

with $k_r = \sqrt{\varepsilon_1}\,\omega/c\sin\theta_1 = \sqrt{\varepsilon_2}\,\omega/c\sin\theta_2$ and $\kappa_i = \sqrt{\varepsilon_i}\,\omega/c\cos\theta_i$. Note that the electric field $\mathcal{E}^1_{z,\omega,\mathbf{k}}$ can be found easily from the electric field $\mathcal{E}^2_{z,\omega,\mathbf{k}}$ just by exchanging index 1 with 2 and v with $-v$.

The total energy of radiation emitted into medium i by the charged particle is calculated by integrating the Poynting vector over the interface at $z = 0$ (see Fig. 2.6) and over time t:

$$W_i = \int dx \int dy \int_{-\infty}^{+\infty} dt \, \mathbf{S}_i \cdot \mathbf{n} \ . \tag{2.75}$$

By substituting the Fourier transform of the electric and magnetic field [see Eq. (2.65)], the energy is given as function of the Fourier components of the fields,

$$W_i = \frac{1}{2\pi} \int d\omega \int dk_x \int dk_y \, \frac{1}{\mu_0} \frac{\mathcal{E}^i_{\omega,\mathbf{k}} \times \mathbf{B}^i_{\omega,\mathbf{k}}}{\left|2\kappa_i\right|^2} \cdot \mathbf{n} \ . \tag{2.76}$$

Because the radiation is a transverse plane wave, the z-component of the Poynting vector $\mathbf{S}^i_{z,\omega,k} = \mathbf{S}^i_{\omega,k}\cos\theta_i$ can be expressed in terms of the radial electric field,

$$\boldsymbol{S}_{z,\omega,\mathbf{k}}^{i} = \sqrt{\varepsilon_i}\sqrt{\frac{\varepsilon_0}{\mu_0}}\left|\boldsymbol{\mathcal{E}}_{\omega,\mathbf{k}}^{i}\right|^2\cos\theta_i = \sqrt{\varepsilon_i}\sqrt{\frac{\varepsilon_0}{\mu_0}}\frac{\left|\boldsymbol{\mathcal{E}}_{r,\omega,\mathbf{k}}^{i}\right|^2}{\cos\theta_i}. \tag{2.77}$$

When the z-component of the Poynting vector (2.77) is substituted into the equation of the radiation energy (2.76) and integration variables are changed: $dk_x dk_y = 2\pi k_i^{\,2}\sin\theta_i\cos\theta_i d\theta_i$, the spectral angular intensity is expressed as,

$$\frac{d^2 W_i}{d\omega d\Omega} = \frac{\sqrt{\varepsilon_i}}{\pi}\sqrt{\frac{\varepsilon_0}{\mu_0}}k_i^{\,2}\left|\frac{\boldsymbol{\mathcal{E}}_{r,\omega,\mathbf{k}}^{i}}{2\kappa_i}\right|^2. \tag{2.78}$$

By substituting the electric field of medium 2 $\boldsymbol{\mathcal{E}}_{r,\omega,\mathbf{k}}^{2}$ [Eq. (2.74)] in this equation, the spectral angular intensity radiated into that medium as a function of angle θ_2 is found, i.e. the Ginzburg-Frank equation:

$$\frac{d^2 W_2}{d\omega d\Omega} = \frac{q^2}{4\pi\varepsilon_0}\frac{\beta^2\sqrt{\varepsilon_2}\sin^2\theta_2\cos^2\theta_2}{\pi^2 c}\frac{\left|\varepsilon_2-\varepsilon_1\right|^2}{\left|\varepsilon_1\cos\theta_2+\sqrt{\varepsilon_1\varepsilon_2-\varepsilon_2\sin^2\theta_2}\right|^2}$$

$$\times\frac{\left|1-\varepsilon_2\beta^2-\beta\sqrt{\varepsilon_1-\varepsilon_2\sin^2\theta_2}\right|^2}{\left|(1-\varepsilon_2\beta^2\cos^2\theta_2)(1-\beta\sqrt{\varepsilon_1-\varepsilon_2\sin^2\theta_2})\right|^2}. \tag{2.79}$$

The spectral angular intensity radiated into the backward direction is found by exchanging ε_2 with ε_1, β with $-\beta$ and θ_2 with θ_1, which is also obvious from symmetry considerations. The Ginzburg-Frank equation includes transition radiation and Cherenkov radiation. On the one hand, the spectral angular intensity is proportional to the refractive index difference $|\varepsilon_2 - \varepsilon_1|$, which is typical for transition radiation. On the other hand, when the two denominators in the second line of Eq. (2.79) are put equal to zero, the Cherenkov angular relation (2.45) is obtained for each medium. Consequently, the spectral angular intensity becomes infinite at exactly the Cherenkov angle, because the energy is integrated from $t = -\infty$ to $+\infty$. However, in an actual medium either the path length is finite or the medium is absorbing, which both make the Cherenkov intensity finite. In Sec. 2.2.2.3 the soft x-ray Cherenkov contribution is analyzed in case medium 1 is an absorbing medium, which limits the Cherenkov spectral angular intensity.

It is well known that for relativistic electrons the transition radiation is emitted in a narrow cone centered around the electron trajectory. This can be easily illustrated by the case that electrons exit a metal, which has dielectric constant much larger than unity and Cherenkov radiation negligible due to the high absorption. The spectral angular intensity of transition radiation is approximated by

$$\frac{d^2 W_2}{d\omega d\Omega} = \frac{e^2}{4\pi\varepsilon_0}\frac{\beta^2\cos^2\theta_2}{\pi^2 c\left|1-\beta^2\cos^2\theta_2\right|^2}. \tag{2.80}$$

By differentiating with respect to θ_2 and for relativistic electrons ($\gamma \gg 1$), the peak intensity of transition radiation is found at

$$\theta_2 = \frac{1}{\gamma}. \tag{2.81}$$

This intensity maximum also applies to the x-ray region.
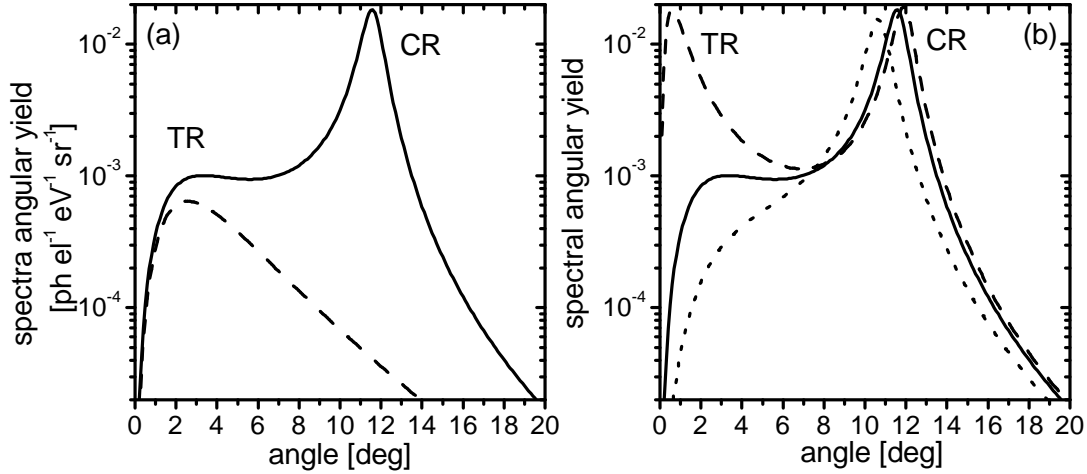
Figure 2.7: (a) Spectral angular yield calculated using Eq. (2.82). The solid curve represent the transition radiation (TR) and Cherenkov radiation (CR) generated by 10-MeV electrons in silicon at $\hbar\omega = 99.7$ eV. The dashed curve uses the same complex dielectric constant value with the real part reversed in sign ($\chi = -\chi' + i\cdot\chi''$), which excludes Cherenkov radiation at 99.7 eV, but which keeps the transition radiation part unaffected. (b) Spectral angular yield for silicon at 99.7 eV for different electron energies: 5 MeV (dotted curve), 10 MeV (solid curve) and 50 MeV (dashed curve).

2.2.2.3 Soft x-ray transition and Cherenkov radiation

In this section the Ginzburg-Frank equation (2.79) is applied to the soft x-ray region, where materials are highly absorbing. Note that the entire derivation of Eq. (2.79) is valid for complex values of ε_i. We consider the forward emitted radiation of a relativistic electron traveling near the speed of light exiting a foil with a thickness much larger than the absorption length, surrounded by vacuum ($\chi_2 = 0$). In the previous section it has already been shown that for relativistic electrons ($\gamma^{-2} \ll 1$) the emission angles are small ($\theta \ll 1$). Additionally, in the soft x-ray region also the dielectric constant is close to unity, i.e. the susceptibility is small ($|\chi_1| \ll 1$). The easiest way of obtaining the approximation is starting with the electric field solution [Eq. (2.74)] and substituting it into Eq. (2.78). By using Snell's law in this approximation ($\theta_1 \approx \theta_2$), we find for the forward emitted angular spectral yield:

$$\frac{d^2 N_2}{d\omega d\Omega} = \frac{\alpha \theta^2}{\omega} \left| \frac{1}{\theta^2 + \gamma^{-2}} - \frac{1}{\theta^2 + \gamma^{-2} - \chi_1} \right|^2. \tag{2.82}$$

Note that, when the denominator in the second term is put equal to zero, the Cherenkov angular relation is obtained [see Eq. (2.56)]. In the backward direction, which is on the vacuum side of the interface where the electron enters an optically thick foil ($\chi_1 = 0$ and $|\chi_2|$ << 1), the backward emitted angular spectral intensity is given by,

$$\frac{d^2W_1}{d\omega d\Omega} = \frac{e^2\theta^2}{4\pi\varepsilon_0}\left|\frac{\chi_2}{\theta^2 + \gamma^{-2}}\right|^2.$$ (2.83)

This intensity only describes transition radiation, because the denominator can never be equal to zero. In addition, the intensity emitted in the backward direction (2.83) is negligible compared to the radiation emitted in the forward direction (2.82), which is very different from the situation in the visible light region, where the transition radiation intensities in forward and backward direction are equal[6].
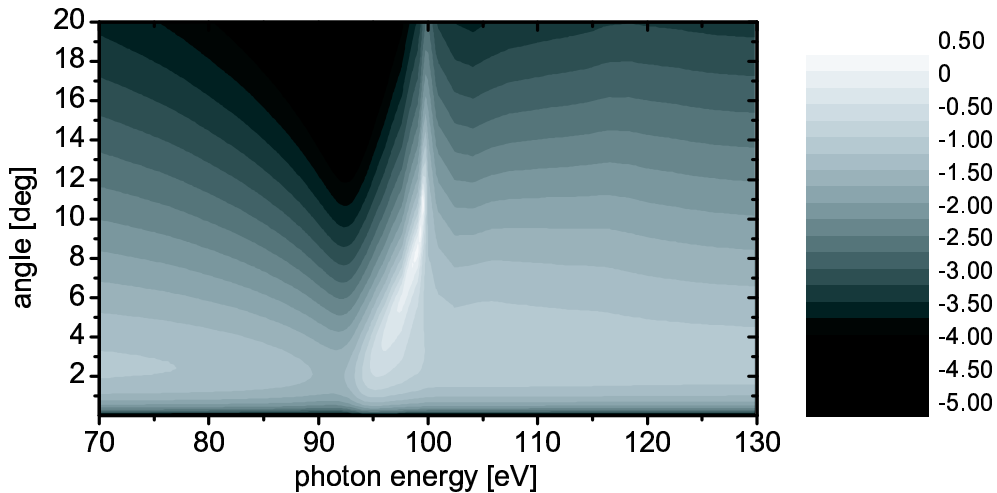
Figure 2.8: Contour plot of the spectral angular yield in log scale from a silicon foil using 10-MeV electrons given by Eq. (2.82). Most prominent is the Cherenkov radiation at 99.7 eV. To the left and the right a continuous spectrum of transition radiation is emitted at small angles.

The forward spectral angular yield (2.82) is often used to calculate the intensity of the transition radiation in the x-ray region. Generally, a simple plasma-frequency model of the dielectric constant [Eq. (2.26)] is used, which precludes the possibility of generating Cherenkov radiation. Such an approach is in fact only correct far from atomic resonances. To calculate the transition and Cherenkov radiation at regions of anomalous dispersion the complex dielectric constant has to be substituted into χ_1 in Eq. (2.82). The solid curve in Fig. 2.7(a) shows the result of such a calculation for the case of silicon at photon energy of 99.7 eV using 10-MeV electrons. Clearly a large peak is seen that is associated with silicon L-edge Cherenkov radiation. At smaller angles a secondary maximum is visible that can be identified with transition radiation. In Eq. (2.82) it is not possible to separate Cherenkov radiation from transition radiation. However, the transition-radiation contribution can be quantified in an artificial way by calculating the spectral angular yield for a hypothetical medium with a complex susceptibility, which is in magnitude identical but whose real part has the opposite

sign: $\chi = -\chi' + i{\cdot}\chi''$. In this way the Cherenkov contribution is eliminated without changing the contrast in dielectric constant or the absorption length. The transition radiation, thus calculated, is indicated by the dashed curve in Fig. 2.7(a). Now the transition radiation clearly peaks at the angle $\gamma^{-1} \approx 2.8°$ [see Eq. (2.81)].

The separation of Cherenkov radiation and transition radiation becomes clearer, when the angles of maximum intensity are more separated. For example, in Fig. 2.7(b) the electron energy is changed. For increasing electron energy the transition radiation peaks at smaller angles and the spectral angular yield increases. The Cherenkov angle on the other hand approaches a constant value for increasing electron energy. For a specific electron energy the angle of transition radiation (2.81) and the Cherenkov angle (2.56) coincide. At this electron energy the two radiation phenomena are indistinguishable.

In Fig. 2.8 the full spectral angular yield is plotted as a function of both emission angle and photon energy for 10-MeV electrons passing through a silicon foil. Between 95 eV and 100 eV the Cherenkov radiation is clearly visible. The Cherenkov angle (2.56) increases according to the dispersion [see Fig. 2.4(a)]. On the left and right side the continuous spectrum of transition radiation is seen which has its maximum at the angle of γ^{-1}.

It is instructive to calculate the spectral yield by integrating the spectral angular yield (2.82) over all emission angles[17],

$$\frac{dN}{d\omega} = 2\pi \frac{\alpha}{\pi^2 \omega} \int_0^\infty \theta^2 \left| \mathbf{I}(\omega, \theta) \right|^2 \theta\, d\theta \qquad (2.84)$$

with

$$\left| \mathbf{I}(\omega, \theta) \right|^2 = \frac{\chi'^2 + \chi''^2}{(\theta^2 + \gamma^{-2})((\theta^2 + \gamma^{-2} - \chi')^2 + \chi''^2)} . \qquad (2.85)$$

The resulting spectral yield is given by

$$\frac{dN}{d\omega} = \frac{\alpha}{\omega\pi} \left\{ \left(\frac{1}{2} - \frac{\gamma^{-2}\chi'}{|\chi|^2} \right) \ln\left(\frac{(\chi' - \gamma^{-2})^2 + \chi''^2}{\gamma^{-4}} \right) - 1 \right\} +$$

$$\frac{\alpha}{\omega} \frac{1}{\chi''} \left(\chi' - \gamma^{-2} \frac{\chi'^2 - \chi''^2}{|\chi|^2} \right) \left(\frac{1}{\pi} \arctan\left(\frac{\chi' - \gamma^{-2}}{\chi''} \right) + \frac{1}{2} \right) . \qquad (2.86)$$

Expression (2.86) consists of two terms: the first term is identified as transition radiation and the second term is identified as Cherenkov radiation. The condition for Cherenkov radiation is described by the arctangent, with the parameter $(\chi' - \gamma^{-2})/\chi''$ as argument. When $\chi' - \gamma^{-2}$ is much larger than χ'' (χ'' is by definition positive), the factor containing the arctangent approaches unity; when $\chi' - \gamma^{-2}$ is much smaller than $-\chi''$, it approaches zero. In the region where $\chi' - \gamma^{-2} \gg \chi''$ the arctangent can be roughly approximated by a Heaviside step function (η) with the Cherenkov condition $\chi' - \gamma^{-2}$ as argument. Using this approximation, Eq. (2.86) reduces to

$$\frac{dN}{d\omega} = \frac{\alpha}{\pi\omega}\left\{\left(\frac{1}{2} - \frac{\gamma^{-2}}{\chi'}\right)\ln\left(\frac{(\chi' - \gamma^{-2})^2}{\gamma^{-4}}\right) - 1\right\} + \frac{\alpha}{\omega}\frac{\chi' - \gamma^{-2}}{\chi''}\eta(\chi' - \gamma^{-2}). \tag{2.87}$$

The Cherenkov term in Eq. (2.87) is identical to the soft x-ray Cherenkov spectral yield (2.59) obtained using the phenomenological approach of Sec. 2.2.1.2. Therefore, we find that Eq. (2.59) is a valid approximation for photon energies that satisfy $\chi' - \gamma^{-2} \gg \chi''$, which is mainly at the low photon-energy side of an absorption edge. This is illustrated by Fig. 2.9(a), where two curves for the spectral yield are plotted for the case of 10-MeV electrons passing through a silicon foil, calculated by using Eq. (2.59), which is the Frank-Tamm approach, and by using Eq. (2.86), which is the Ginzburg-Frank approach, respectively. Clearly, for the Cherenkov peak at the low photon-energy side of the absorption edge the two spectral yields are equal.
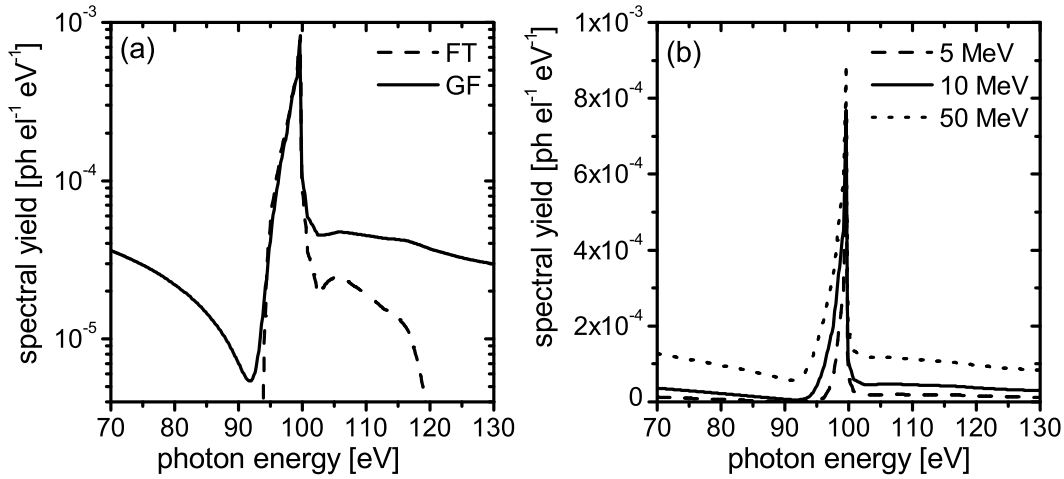
Figure 2.9: (a) Comparison between the spectral yield calculated with the Frank-Tamm equation (2.59) (FT) and with the Ginzburg-Frank equation (2.82) (GF) in case of 10-MeV electron passing through a silicon foil. (b) Spectral yield (GF) using different electron energies, namely 5, 10 and 50 MeV.

On the basis of Eq. (2.87) the intensity difference between the two radiation phenomena can be discussed. It is well known that transition radiation gives rise to the main intensity contribution in the x-ray region for high-energy electrons ($\gamma \gg 1$). For $\gamma^{-2} \ll \chi'$, Eq. (2.87) can be approximated by

$$\frac{dN}{d\omega} = \frac{\alpha}{\pi\omega}\ln\left(\frac{\chi'}{\gamma^{-2}}\right) + \frac{\alpha}{\omega}\frac{\chi'}{\chi''}\eta(\chi'). \tag{2.88}$$

The Cherenkov yield becomes constant in the high-energy limit, while the transition radiation part still increases with γ. For moderate electron energies (up to 25 MeV), however, the transition radiation spectral yield can be neglected with respect to the spectral Cherenkov yield as can be seen from Fig. 2.9(b) in case of silicon using 5 or 10-MeV electrons. The dotted curve indicates the spectral yield for 50-MeV electrons and the offset under the

Cherenkov peak is the contribution from transition radiation. Still in this case, the Cherenkov radiation spectral yield is higher than the transition radiation yield, while, as is indicated in Fig. 2.7(b), the spectral angular yield values are about equal. The reason is that Cherenkov radiation is emitted at a larger angle and therefore the integrated yield over the total solid angle is larger. The transition-radiation spectral yield increases rather slowly as function of electron energy, due to the logarithmic dependence in Eq. (2.88), because of the decreasing solid angle. From Eq. (2.88) it can be calculated that the transition radiation and Cherenkov radiation spectral yield from silicon at 99.7 eV are equal for $\gamma \approx 10^9$. The conclusion is that in the soft x-ray region the spectral yield of Cherenkov radiation is much larger than the spectral yield of transition radiation.
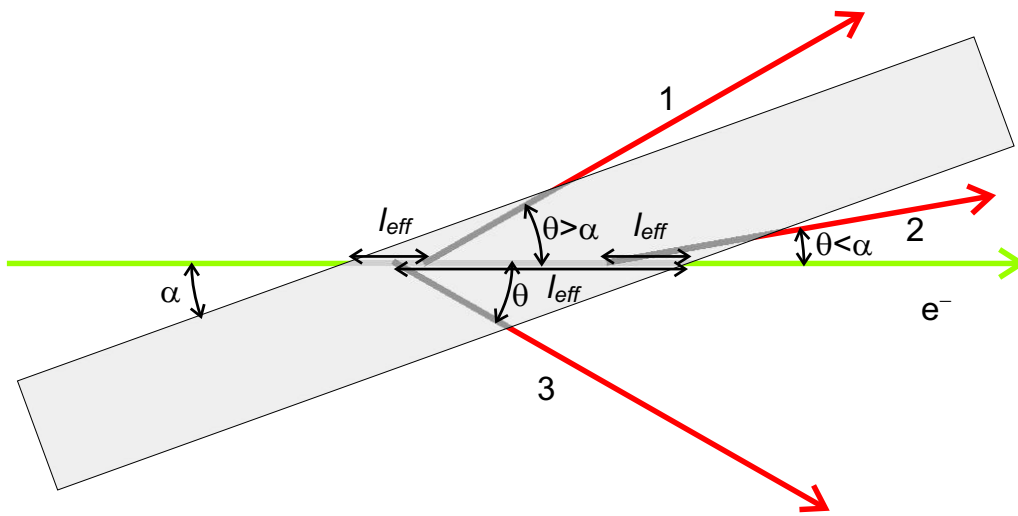
Figure 2.10: Cherenkov radiation generated by an electron beam that passes through the foil with a tilt angle α with respect to the electron beam. The directions 1, 2 and 3 indicate emission directions of the Cherenkov radiation.

2.3   Grazing-incidence Cherenkov radiation

The analysis in the previous section shows that the soft x-ray Cherenkov radiation yield is limited by the absorption length in the medium. Up to now only Cherenkov radiation has been considered produced under the condition where electrons travel in a direction perpendicular to the material-vacuum interface. Sending the electrons at oblique angles through the foil (see Fig. 2.10) may further enhance the Cherenkov radiation yield. Grazing-incidence Cherenkov radiation was experimentally investigated for the first time by Moral *et al.*[20] using 75-MeV electrons. They have observed intensity enhancement for silicon and carbon Cherenkov radiation at very small tilt angles α, which is the angle between the electron beam and the foil surface (see Fig. 2.10). The observed enhancement was due to external Cherenkov radiation that is generated when an electron grazes over the surface, which is discussed in Sec. 2.3.1. However, at moderate electron energies we are interested in, i.e. from 5 MeV to 25 MeV, this effect is less strong.

For these electron energies, the internal generated Cherenkov radiation contributes significantly to the total output, which is discussed in Sec. 2.3.2. So far, this effect has not been taken into account before. Therefore, we present in this section a detailed phenomenological analysis of the internal-generated Cherenkov radiation at grazing-incidence angles.

The analysis is started by reviewing the effect of absorption. For some emission angles the Cherenkov radiation is less absorbed, because the electrons travel a longer distance near the surface. In addition, due to the grazing angles the refraction and transmission of the internal-generated Cherenkov radiation through the interface have to be taken into account. At some combination of emission angles and tilt angles, total internal reflection occurs and the internal-generated Cherenkov radiation cannot exit the foil. Due to the fact that the medium is absorbing, the radiation is still transmitted at the angles of total internal reflection and contributes to the Cherenkov intensity. Taking these effects together, the enhancement of Cherenkov radiation at grazing incidence is a very subtle effect for moderate electron energies.
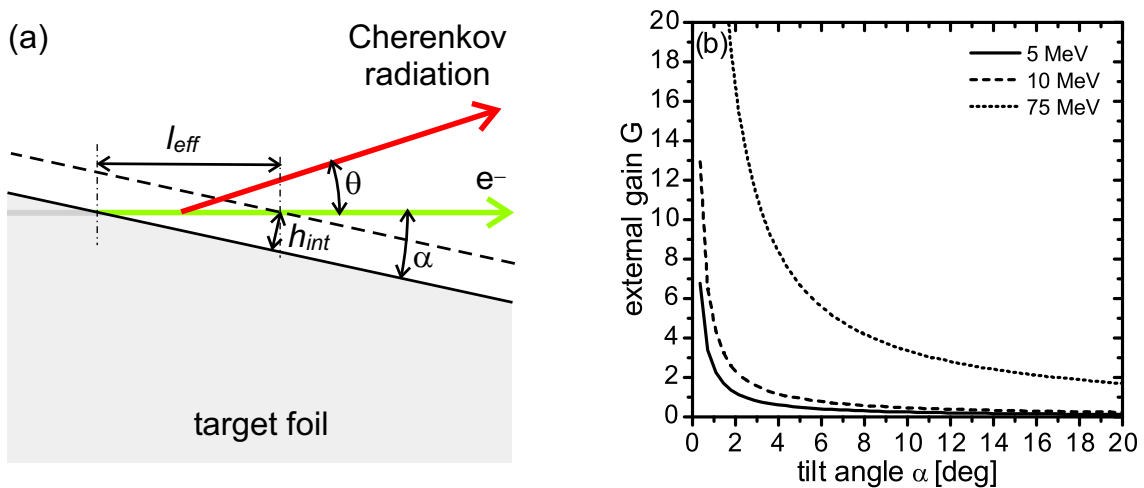
Figure 2.11: (a) When the electron is within a distance h_{int} from the surface of the foil, it emits Cherenkov radiation along a path length l_{eff}. (b) The gain factor, which is l_{eff} divided by l_{abs}, plotted for 12.4-nm silicon Cherenkov radiation for different electron energies.

2.3.1   External Cherenkov radiation

At grazing incidence the electrons travel just outside the material for a long distance very close to the surface [see Fig. 2.11(a)]. The Coulomb field of the electron extends a certain distance and can interact with the surrounding material. For instance, when an electron moves near a grating surface, it emits Smith-Purcell radiation[21,22]. If the surface consists of a flat dielectric medium with a refractive index that fulfills the Cherenkov condition, the electron emits radiation, which can be interpreted as zeroth-order Smith-Purcell radiation. The generation efficiency decreases exponentially with the distance to the surface, which can be characterized by an effective interaction height

$$h_{int} \approx \gamma \frac{\lambda}{2\pi} , \tag{2.89}$$

where λ is the wavelength of the emitted radiation. At grazing incidence an effective length [see Fig. 2.11(a)] can be calculated for which the electron is within a height h_{int} from the surface. A factor can be defined representing the gain in Cherenkov yield with respect to that for normal incidence, as the effective length divided by the absorption length:

$$G = \frac{h_{int}}{l_{abs} \sin \alpha} . \tag{2.90}$$

The gain factor for the case of silicon L-edge (i.e. 12.4 nm) Cherenkov radiation is plotted in Fig. 2.11(b) as a function of the tilt angle α for different electron energies. Because the effective interaction height is proportional to γ, the gain increases with electron energy. For 75-MeV electrons the gain factor exceeds unity over a large tilt angle range. For 5-MeV electrons, on the other hand, this effect is negligible for incidence angles $\alpha > 2°$.

2.3.2 Internal Cherenkov radiation

The analysis of the internal-generated Cherenkov radiation is split into three parts. First, in Sec. 2.3.2.1 the possible gain due to less absorption of the radiation along its path to the surface is analyzed for various tilt angles α. Next, in Sec. 2.3.2.2 the influence of refraction of the Cherenkov radiation at the surface, in particular total internal reflection, is presented. Finally, in Sec. 2.3.2.3 it is shown that Cherenkov radiation that propagates inside an absorbing medium and is incident on the interface at an angle larger than the angle of total internal reflection is still transmitted.

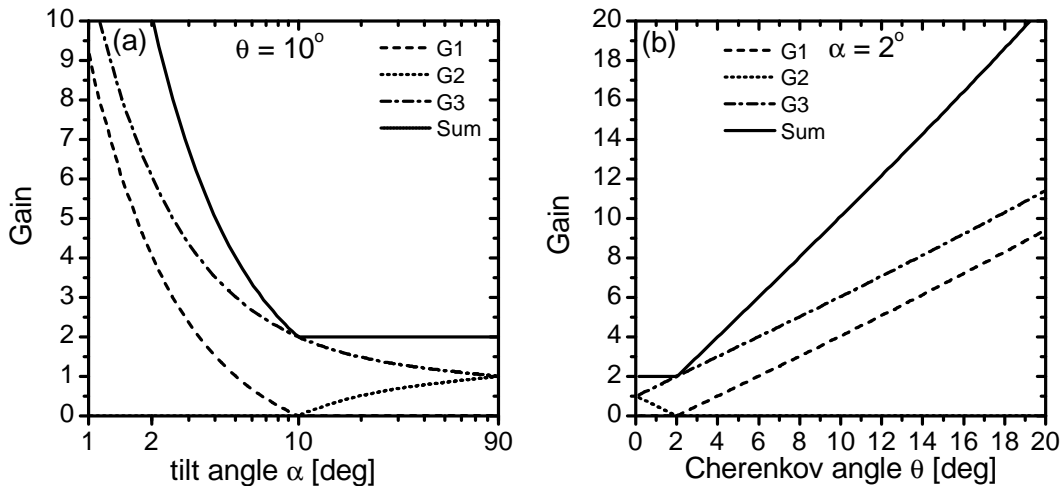Figure 2.12: (a) Gain factors for 3 different directions (see Fig. 2.10) plotted versus tilt angle α with Cherenkov angle fixed at $\theta = 10°$. (b) Gain factors plotted versus Cherenkov angle θ with tilt angle fixed at $\alpha = 2°$.

2.3.2.1   Effective generation length

At perpendicular incidence the Cherenkov output of a thick foil is limited by the absorption length. The emitted radiation originates from a thin layer: 90% of the radiation is generated within $2.3l_{abs}$ from the back of the foil. This can be characterized by an effective path length l_{eff} of the electron, for which the distance the radiation has to travel to the surface is equal to l_{abs}. For normal incidence, i.e. $\alpha = 90°$, the effective length is given by

$$l_{eff}^{\perp} = l_{abs} \cos\theta \,. \tag{2.91}$$

For grazing incidence the effective length can be much longer and therefore an enhancement of the Cherenkov intensity is expected. In Fig. 2.10 the three possible directions (1, 2 and 3) of Cherenkov radiation to the foil surface are indicated. For each direction a gain factor can be defined, which is the effective length l_{eff} divided by the perpendicular effective length $l_{eff}^{\perp}$. In direction 1, for emission angles larger than the tilt angle ($\theta > \alpha$), the gain factor is given by

$$G_1 = \frac{\tan\theta}{\tan\alpha} - 1 \,. \tag{2.92}$$

In the small angle approximation, it thus follows that the tilt angle α has to be at least twice as small as the Cherenkov angle θ to be more effective than in the case of perpendicular incidence. In direction 2, for emission angles smaller than the tilt angle ($0 < \theta < \alpha$), the gain is given by

$$G_2 = 1 - \frac{\tan\theta}{\tan\alpha} \,. \tag{2.93}$$

In this direction the gain is always smaller than unity. In direction 3, for any emission angle and tilt angle, the gain is given by

$$G_3 = 1 + \frac{\tan\theta}{\tan\alpha} \,. \tag{2.94}$$

Into this direction the gain is always larger than unity. In Figs. 2.12(a) and 2.12(b) the separate gain factors G_1, G_2 and G_3, and their sum are plotted as a function of Cherenkov angle θ and tilt angle α, respectively. The sum at emission angles smaller than the tilt angle ($\theta < \alpha$) is equal to 2 as can be seen in Fig. 2.12. This indicates that for these angles there is no enhancement compared to the perpendicular incidence, which is confirmed by an exact integration over the azimuth angle of the exponential absorption. The intensity gain in direction 3 is compensated by the loss in direction 2.

At emission angles larger than the tilt angle ($\theta > \alpha$), the gain in direction 3 exceeds the value 2, so a net enhancement of the Cherenkov radiation is obtained. Additionally, at these emission angles radiation is emitted from the back surface of the foil, i.e. in direction 1, instead of direction 2. This enhances the total intensity even further. For instance, for $\theta = 10°$ and $\alpha = 2°$ the sum of the gain factors is about 10.

2.3.2.2 Total internal reflection

So far, we have not taken refraction into account, but which becomes important for grazing incidence. The refractive index for Cherenkov photon-energies is larger than vacuum, so total internal reflection may also be relevant. The angles of incidence θ_i on the interface for the different directions are given by:

$$\theta_i^1 = \frac{\pi}{2} + (\alpha - \theta),$$
(2.95)

$$\theta_i^2 = \frac{\pi}{2} - (\alpha - \theta),$$
(2.96)

$$\theta_i^3 = \frac{\pi}{2} - (\alpha + \theta).$$
(2.97)

As an example, these angles are plotted in Fig. 2.13(a) for the case of silicon L-edge Cherenkov radiation as a function of photon energy using 5-MeV electrons and for a tilt angle $\alpha = 2°$. The emission angle θ with respect to the electron trajectory is calculated by the Cherenkov angular relation (2.56) using the refractive index of silicon and is plotted as a function of photon energy in Fig. 2.13(b) (solid curve).
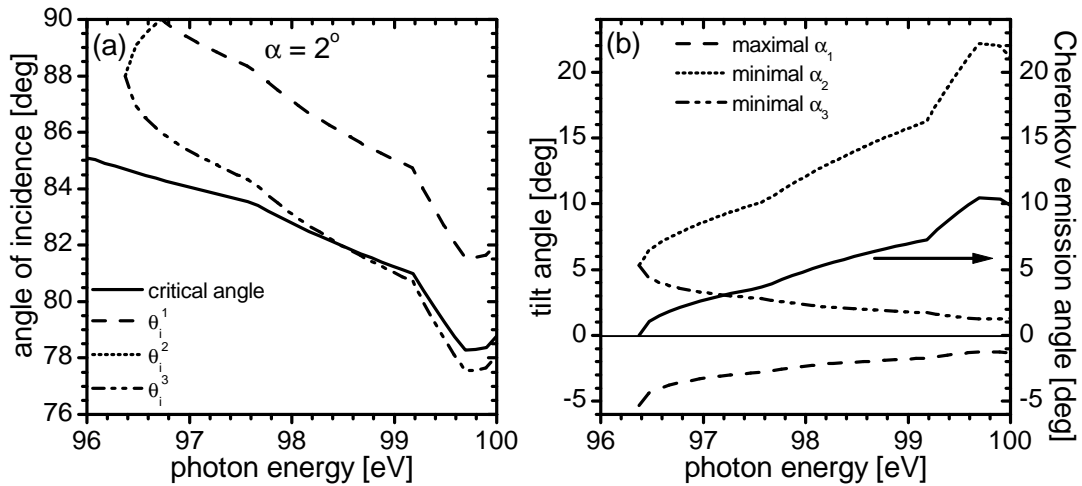
Figure 2.13: (a) Angle of incidence θ_i of the silicon Cherenkov radiation as function of photon energy calculated for the 3 different directions (see Fig. 2.10) and for $\alpha = 2°$. The solid curve indicates the critical angle. (b) The requirements of the tilt angle α to keep the angle of incidence below the critical angle as function of photon energy. The solid curve indicates the silicon Cherenkov emission angle for 5-MeV electrons.

In case of a transparent medium, i.e. with a real-valued refractive index n_i, the angle of refraction θ_t is given by Snell's law:

$$n_i \sin \theta_i = n_t \sin \theta_t,$$
(2.98)

with $n_t = 1$ in case of vacuum. The critical angle, which is the minimal angle of total internal reflection, is obtained when $n_i \sin\theta_i = 1$. By substituting the angle of incidence of Eqs. (2.95)-(2.97) in this condition, it can be written in terms of the tilt angle and the Cherenkov emission angle, i.e. for direction 1 and 2

$$\cos(\alpha - \theta) = \frac{1}{n_i}, \tag{2.99}$$

and for direction 3

$$\cos(\alpha + \theta) = \frac{1}{n_i}. \tag{2.100}$$

It thus follows that, when the foil is placed parallel to the electron beam, i.e. $\alpha = 0°$, the Cherenkov radiation for ultra-relativistic electrons $v/c \rightarrow 1$ will impinge on the interface at exactly the critical angle [see Eq. (2.45)]. The actual Cherenkov angle (for $v/c < 1$) is slightly smaller and thus the angle of incidence on the surface larger. Therefore, to stay below the critical angle the foil has to be slightly tilted with a maximal angle for direction 1 ($\theta > \alpha$) given by

$$\alpha^1_{max} = \theta - \arccos\frac{1}{n_i}, \tag{2.101}$$

and a minimal angle for direction 2 ($0 < \theta < \alpha$) given by

$$\alpha^2_{min} = \arccos\frac{1}{n_i} + \theta, \tag{2.102}$$

and for direction 3 given by

$$\alpha^3_{min} = \arccos\frac{1}{n_i} - \theta. \tag{2.103}$$

As an example, these minimal or maximal tilt angles are plotted for silicon L-edge Cherenkov radiation as a function of photon energy using 5-MeV electron in Fig. 2.13(b). Equation (2.101) shows that radiation in direction 1 can never exit the surface, because α has to be smaller than zero. Radiation in direction 2 [see Eq. (2.103)] can only exit for large values of tilt angle, i.e. $\alpha > 2\theta$. In direction 3 the minimal angle is given by the difference between the maximum Cherenkov angle ($v/c \rightarrow 1$) and the real emission angle determined by the value of v/c.

For the example of silicon L-edge Cherenkov radiation the angle of incidence θ_i as a function of photon energy is compared in Fig. 2.13(a) with the critical angle (solid curve) for a tilt angle $\alpha = 2°$. Only in direction 3 there is a limited photon energy range for which no total internal reflection occurs. The transmitted radiation has an angle of refraction that is larger than the angle of incidence and it is therefore grazing over the surface of the foil.

2.3.2.3 Refraction and transmission from complex medium

Absorbing media generally complicate the analysis of refraction and transmission considerably. Plane waves in absorbing media are described by the general formalism of harmonic inhomogeneous plane waves (HIPW)[23] and their refraction is described by the generalized Snell-Descartes laws of refraction[24,25,26]. However, in the specific case of Cherenkov radiation the planes of constant phase and amplitude in the incident medium are parallel [see Fig. 2.14(a)] and refraction is described by a complex version of Snell's law of refraction,

$$\tilde{n}_i \sin \theta_i = n_t \sin \tilde{\theta}_t. \tag{2.104}$$

where the angle of incidence θ_i and refractive index of vacuum $n_t = 1$ are real numbers, as usual, but $\tilde{n}_i$ and $\tilde{\theta}_t$ are complex numbers. The complex angle of refraction is defined as

$$\tilde{\theta}_t = \theta_t + i\beta_t, \tag{2.105}$$

with θ_t the angle of the phase refraction and β_t the so-called inhomogeneity parameter for the amplitude refraction. Given a certain angle of incidence θ_i and the known complex index of refraction $\tilde{n}_i$, the complex angle $\tilde{\theta}_t$ can be calculated. In Fig. 2.15 θ_t and β_t are plotted as a function of angle of incidence for 99.4-eV radiation from silicon into vacuum. As a result a critical angle for which total internal reflection occurs is not present. Instead the true angles of refraction are close to 90° for angles larger than what would be the critical angle ($\theta = 79.9°$) if only the real part of the refractive index is considered.
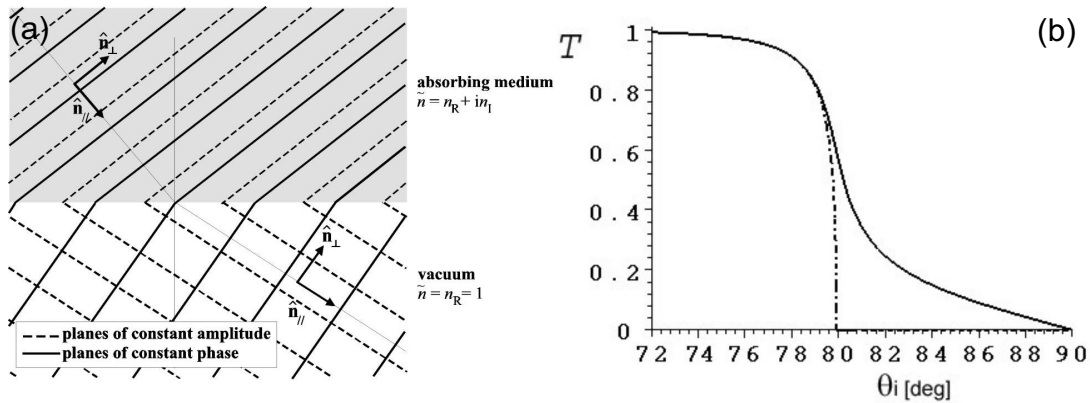
Figure 2.14: (a) Planes of constant phase and amplitude for refraction at an interface between an absorbing and a non-absorbing medium, such as vacuum. (b) Comparison between the transmission T for real refractive index (dashed curve) and complex refractive index (solid curve) for refraction from silicon into vacuum of 99.4-eV radiation as function of angle of incidence.

The transmission at these angles is calculated by the complex Fresnel coefficients,

$$T = 1 - |\tilde{r}|^2 \tag{2.106}$$

with the reflection coefficient for transverse magnetic polarization

$$
\tilde{r}_{TM} = \frac{\left(\dfrac{\tilde{n}_t}{\tilde{n}_i}\right)^2 \cos\theta_i - \sqrt{\left(\dfrac{\tilde{n}_t}{\tilde{n}_i}\right)^2 - \sin^2\theta_i}}{\left(\dfrac{\tilde{n}_t}{\tilde{n}_i}\right)^2 \cos\theta_i + \sqrt{\left(\dfrac{\tilde{n}_t}{\tilde{n}_i}\right)^2 - \sin^2\theta_i}} \,,
\tag{2.107}
$$

and plotted in Fig. 2.14(b) as function of angle of incidence for 99.4-eV radiation from silicon into vacuum. Combining this result with Fig. 2.13(a), it can be estimated that 20% of the radiation in direction 1 is transmitted, although the radiation hits the surface at an angle larger than the critical angle. The gain of about 4 in direction 1, plotted in Fig. 2.12(b), does not compensate this low transmission. Therefore, by placing a foil under grazing incidence the enhancement is mainly due to direction 3, but it is limited by the minimal tilt angle (e.g. $\alpha = 1.2°$ at 99.4 eV) to stay below the critical angle.
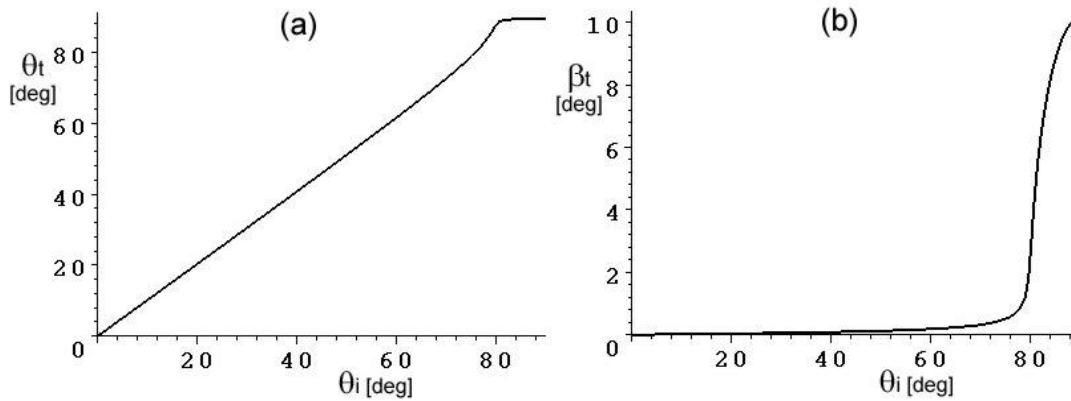
Figure 2.15: Solution of the complex angle of transmission $\theta_t + i\,\beta_t$ from the complex Snell's law for 99.4-eV radiation from silicon into vacuum as function of angle of incidence.

2.3.3   Conclusion grazing incidence

Based on the analysis of the previous sections we have seen that various factors influence the gain at grazing incidence for the electron energy range considered in this thesis (5 MeV to 25 MeV). In this phenomenological approach the generation, absorption and transmission have been analyzed separately. An exact treatment should involve solving the boundary conditions with an electron passing the interface at an oblique angle α, following the Ginzburg-Frank approach in Sec. 2.2.2.2. This analysis will include absorption, refraction, transmission and polarization.

So far, the electron scattering is not taken into account. For the case a very thin foil is put at grazing incidence, the electron path length through the foil can be large and consequently the average scattering angle as well. This angular distribution of the electron beam spoils the gain at grazing incidence. Especially in direction 3 where the electron beam first passes through the foil and then generates the Cherenkov radiation at the back surface. In direction 1

the foil does not disturb the electron beam at the front side, but grazing-incidence Cherenkov radiation has rather low gain.

An advantage of using a foil at grazing incidence might be that the radiation intensity is concentrated into direction 3, although the total enhancement of the Cherenkov yield at grazing incidence is rather low for the electron energies considered. This reduces the solid angle of the source and thus increases the radiation quality, which is expressed in the quantity brightness (see Sec. 6.1). Therefore it is worth doing experiments to measure the enhancement as a function of tilt angle.

References

1 I.M. Frank and I.E. Tamm, "Coherent visible radiation of fast electrons passing through matter", *Dokl. Akad. Nauk SSSR* **14**, 109-114, 1937.

2 J.V. Jelley, *Cherenkov radiation and its applications*, Pergamon Press, London, 1958.

3 M.L. Ter-Mikaelian, *High-Energy Electromagnetic Processes in Condensed Media*, Chap. 4, Wiley, Toronto, 1972.

4 R. Wolf, *Review of the general theory of Cherenkov transition and transition radiation*, Internal Traineeship Report FTV/TIB 2001-03, Eindhoven, 2001.

5 V.L. Ginzburg and I.M. Frank, *Zh. Eksp. Teor. Fiz.* **16**, 15 (1946) [short version: *J. Phys. USSR* **9**, 353 (1949)].

6 V.L. Ginzburg and V.N. Tsytovich, *Transition Radiation And Transition Scattering*, Chap. 2, Hilger, Bristol, 1990.

7 D.T. Attwood, *Soft X-rays And Extreme Ultraviolet Radiation: Principles And Applications*, Cambridge University Press, Cambridge, 2000.

8 C.T. Chantler, K. Olsen, R.A. Dragoset, A.R. Kishore, S.A. Kotochigova and D.S. Zucker (2003), *X-Ray form factor, attenuation and scattering tables* (version 2.0). [Online] Available: http://physics.nist.gov/ffast [Access date]. National Institute of Standards and Technology, Gaithersburg, MD. Originally published as C.T. Chantler, *J. Phys. Chem. Ref. Data* **29**(4), 597-1048 (2000); and C.T. Chantler, *J. Phys. Chem. Ref. Data* **24**, 71-643 (1995).

9 B.L. Henke, E.M. Gullikson and J.C. Davis, "X-ray interactions: photoabsorption, scattering, transmission, and reflection at E=50-30000 eV, Z=1-92", *At. Data and Nucl. Data Tables* **54**(2), 181-342 (1993). [Online] Available: http://www-cxro.lbl.gov.

10 D.Y. Smith and J.H. Barkyoumb, "Sign reversal of the atomic scattering factor and grazing-incidence transmission at x-ray-absorption edges", *Phys. Rev. B* **41**, 11529-11535, 1990.

11 P.A. Cherenkov, *Dokl. Akad. Nauk SSSR* **2**, 451 (1934).

12 P.A. Cherenkov, *Dokl. Akad. Nauk SSSR* **4**, 105 (1937).

13 Lord Kelvin, Nineteenth Century, Clouds over Dynamical Theory of Heat and Light, *Phil. Mag.*, July (1901).

14 A. Sommerfeld, *Götting. Nachricht.* **99**, 363 (1904).

15 A. Sommerfeld, *Götting. Nachricht.*, 201 (1905).

16 J.V. Jelley, *Cherenkov radiation and its applications*, Pergamon Press, London, 1958.

[17] V.A. Bazylev, V.I. Glebov, E.I. Denisov, N.K. Zhevago, M.A. Kumakhov, A.S. Khlebnikov and V.G. Tsinoev, "X-ray Cerenkov radiation. Theory and experiment", *Sov. Phys. JETP* **54**, 884-892, 1981.

[18] M. Abramowitz and I.A. Stegun, *Handbook of mathematical functions with formulas, graphs, and mathematical tables*, John Wiley, New York, 1972

[19] G.B. Arfken and H.J. Weber, *Mathematical methods for physicists*, Academic Press, San Diego, 1995, Table 8.5.

[20] M.J. Moran, B. Chang, M.B. Schneider and X.K. Maruyama, "Grazing-incidence Cherenkov X-ray generation", *Nucl. Instrum. Methods* **B48**, 287 (1990).

[21] S.J. Smith and E.M. Purcell, Phys. Rev. **92**, 1069 (1953).

[22] P. Rullhusen, X. Artru and P. Dhez, *Novel radiation sources using relativistic electrons: from infrared to X-rays*, World Scientific, Singapore, 1998.

[23] H.C. Chen, *Theory of Electromagnetic Waves - A Coordinate-Free Approach*, McGraw-Hill Book Company, 1983.

[24] M.A. Dupertuis, M. Proctor and B. Acklin, "Generalization of complex Snell-Descartes and Fresnel laws", *J. Opt. Soc. Am.* **A11**, 1159-1166, 1994.

[25] M.A. Dupertuis, B. Acklin and M. Proctor, "Generalized energy balance and reciprocity relations for thin-film optics", *J. Opt. Soc. Am.* **A11**, 1167-1174, 1994.

[26] R. Brummans, *Generation of soft x-ray Cherenkov radiation at grazing incidence*, Internal Graduation Report FTV/TIB 2003-01, Eindhoven, 2003.

3 Elastic scattering of relativistic electrons[*]

Abstract

The radiation characteristics of soft x-ray emission by relativistic electrons, which produce (resonant) transition radiation or Cherenkov radiation inside a foil or multilayer, is determined not only by the intrinsic emission process but also by the angular distribution of the electrons due to Rutherford scattering. The number of scattering events in these micron-thick foils or multilayers is smaller than about 20, the so-called plural scattering regime. We developed a numerical method to calculate very efficiently the angular distribution of relativistic electrons while passing through a single layer of any material and arbitrary thickness in the plural and part of the multiple scattering regime. The angular scattering distribution is a truncated weighted summation of universal distribution functions, each representing a fixed number of scattering events. These universal distribution functions have to be calculated only once and can be stored in a database for later use. This method of calculating the angular scattering distributions has also been extended to deal with multilayers and to take into account incident electron beams with an arbitrary angular distribution. The calculations have been validated by comparison with Monte Carlo simulations, which require much more computing time.

3.1 Introduction

When relativistic electrons travel through matter, they are scattered due to the interactions with the atomic nuclei and electrons. In foils of typically one micron thickness, the energy loss of electrons with an energy of a few MeV or more is negligible, and the scattering is mainly elastic. Recent developments in the generation of soft x-ray Cherenkov[1,2] and transition radiation[3,4] by MeV electrons has sparked new interest in this old field. Cherenkov and transition radiation are emitted in the forward direction at angles comparable to the average elastic scattering angle for MeV electrons in micron thick foils (i.e. typically in the order of degrees). For this reason, the angular radiation characteristics and thus the achievable brightness depend on the angular distribution of the high-energy electrons moving through

---

[*] Submitted to *Nucl. Instrum. Methods* B with the title: "An efficient method for calculating plural scattering of relativistic electrons in thin foils and multilayers."

these multilayers. For a realistic assessment of the radiation brightness that can be achieved, it is therefore essential to keep track of the evolution of the angular distribution, while the beam propagates through the medium.

An elastic scattering theory for charged particles, moving at high speed through matter, was developed by Molière[5] in 1947 and has been revisited by others[6]. The theory is exact for any number of scattering events in the small-angle approximation. However, the theory does not give the angular distribution explicitly. Therefore, Molière derived an approximate description of the angular distribution, which is valid for foils in which more than about 20 scattering events occur. The theory has also led to numerical methods[7,8] for the calculation of the angular distribution of scattered particles, which also treat the case of less than 20 scattering events. These methods are, however, quite time-consuming.

To efficiently calculate scattering distributions of charged particles in foils, in which the number of scattering events is less than about 20 and made of any type of material and for any relativistic electron energy, a new numerical method has been developed. This method is actually applicable to those foils in which the mean number of scattering events is up to 30-40. The method thus establishes a bridge between the screened elastic Rutherford single-scattering cross-section and the multiple scattering theory of Molière.

The new numerical method, presented in this paper, is based on a set of universal angular distribution functions $g_n(\xi)$, which depend on a normalized angle ξ and which give the angular distribution after exactly n scattering events. The scattering physics is represented by the screened Rutherford cross section. A database[9] of the distributions function values has been generated for the number of scattering events ranging from 1 to 50. The actual angular distribution function of scattered electrons in a single-element foil of a certain finite thickness can be obtained from the universal distribution functions, by a properly truncated summation of these functions with appropriate weighting factors.

The method is subsequently extended to the case of an electron beam with an arbitrary angular distribution. This extension allows the evaluation of the elastic electron scattering distribution at interfaces in multilayers. The numerical results based on our method were compared with the results of Monte Carlo simulations of scattering, again using the screened Rutherford cross-section. The agreement is good, both in the case of scattering in thin single foils and in multilayers. In the region of overlap with the Molière theory, the angular scattering distributions, as calculated with our numerical method, corresponds well with the distributions as obtained from the theory of Molière.

This paper is organized as follows: in Sec. 3.2, the scattering of unidirectional electron beams by single-element foils is treated. In Sec. 3.2.1, we describe the present status of theory and simulations. In Sec. 3.2.2, we describe our method, the summation approach. Sec. 3.2.3 gives the universal distribution functions, which are checked by Monte Carlo simulations. In Sec. 3.3, we apply our method to a two-element multilayer.

3.2   Scattering of unidirectional electron beams by single-element foils

Molière[5,6] modified the well-known Rutherford cross-section by introducing a screening angle. The screened Rutherford cross-section is given by the following:

$$\frac{d\sigma}{d\Omega} = \left(\frac{Ze^2}{2\pi\varepsilon_0 pv}\right)^2 \frac{1}{\left(\chi_\alpha^2 + \theta^2\right)^2}, \tag{3.1}$$

in which $p = \gamma mv$ is the electron momentum, m the rest mass, v the velocity, $\gamma = (1-v^2/c^2)^{-1/2}$ the relativistic Lorentz factor, e the elementary charge and Ze the charge of the nucleus. If N is the density of scatterers in the layer, the differential cross-section $d\sigma/d\Omega$ is defined such that $Nvd\sigma/d\Omega$ is the number of scattering events that occur per unit time, in a solid angle $d\Omega$ at polar angle θ and azimuthal angle φ. The screening angle χ_α depends on the atomic number Z and the kinetic energy $E = (\gamma - 1)mc^2$ of the electron. According to Bethe[6] $\chi_\alpha(Z,E) = \sqrt{1.13 + 3.76\eta^2}\chi_0$ with $\chi_0 = \hbar/0.885a_0 Z^{-1/3}p$ and $\eta = Z\alpha c/v$ with a_0 the Bohr radius and α the fine structure constant. The total cross-section σ is given by

$$\sigma = \int \frac{d\sigma}{d\Omega} d\Omega = \left(\frac{Ze^2}{2\pi\varepsilon_0 pv}\right)^2 \frac{\pi}{\chi_\alpha^2}. \tag{3.2}$$

The expectation value of the total number of scattering events λ in a layer of thickness t, with density of scatterers N is thus given by $\lambda = N\sigma t$.

     The classification of scattering processes due to the passage through a foil is usually divided into three categories: single, plural and multiple scattering. Single scattering by an atom is described by the screened Rutherford cross-section (3.1). Plural scattering is defined as the regime in which between 1 and about 20 scattering events occur, ($\lambda = 1$-20) while multiple scattering describes the scattering events with more than about 20 events. ($\lambda > 20$) This paper is concerned with the regime of plural scattering. Inelastic collisions, i.e. energy losses, are not taken into account. This approximation can be justified by the fact that we consider 50 scattering events at most.

3.2.1   Existing theory for plural and multiple scattering

To describe elastic scattering of electrons in single-element foils, we start on the basis of the theory of multiple scattering of electrons by atoms according to Molière[5] and Bethe[6]. The scattering of electrons by many atoms in a foil can be described by an angular distribution function $f(\theta)$, independent of the azimuth φ. It is normalized in the small-angle approximation in the following way:

$$\int f(\theta)\, d\Omega \approx 2\pi \int_0^\infty \theta f(\theta)\, d\theta = 1. \tag{3.3}$$

     In the small-angle approximation, the angular distribution function $f(\theta)$, after traversing a thickness t, is given by:

$$f(\theta) = \int_0^\infty du\, u J_0(u\theta) \exp\left(-Nt \int_0^\infty d\theta'\theta' \frac{d\sigma}{d\Omega}(\theta')(1 - J_0(u\theta')) \right), \tag{3.4}$$

with $J_0(u)$ the zeroth-order Bessel function of the first kind. This solution is exact in the small-angle approximation. Molière substituted the screened Rutherford cross-section into Eq. (3.4) to evaluate $f(\theta)$. The derived approximated angular distribution function is given by the sum of a Gaussian distribution and correction terms. Molière's approach is valid for an average number of scattering events of $\lambda \geq 20$.

In the plural regime the Molière approach does not work, because the probability that an electron passes the layer without scattering becomes significant. The latter possibility is not taken into account in the Molière approximation. For scattering in this regime, Bielajew[7] derived from Eq. (3.4) the exact expression for the angular distribution with the screened Rutherford differential cross-section. This expression is given by:

$$f(\theta) = \frac{e^{-\lambda}\dfrac{\delta(\xi)}{\xi} + \left(1 - e^{-\lambda}\right)\displaystyle\int_0^\infty du\, u J_0(u\xi) j(\lambda,u)}{2\pi\chi_\alpha^2}, \tag{3.5}$$

where

$$j(\lambda,u) = \frac{e^{\lambda u K_1(u)} - 1}{e^\lambda - 1}, \tag{3.6}$$

with $K_1(u)$ the modified first-order Bessel function of the second kind. The normalized angle is given by $\xi = \theta/\chi_\alpha$. The factor $1/(2\pi\chi_\alpha^2)$ is due to the normalization [see Eq. (3.3)]. The angular distribution function is split into two parts: a part containing a Dirac delta function, describing the unscattered part, and a part describing the distribution after at least one scattering event. Bielajew[7] gave an approximate numerical treatment of Eq. (3.5), for both the plural and the multiple scattering regime. The essence of our numerical approach, which we call the summation approach and which is limited to the plural and part of the multiple scattering regime, is that it is less time consuming than that of Bielajew.

3.2.2   The summation approach

The angular distribution function (3.5) can be further analyzed by expanding the numerator of $j(\lambda,u)$ into a Taylor series with respect to λ:

$$f(\theta) = \frac{e^{-\lambda}}{2\pi\chi_\alpha^2}\left(\frac{\delta(\xi)}{\xi} + \sum_{n=1}^\infty \frac{\lambda^n}{n!} g_n(\xi) \right), \tag{3.7}$$

with

$$g_n(\xi) = \int_0^\infty du\, u \left(u K_1(u)\right)^n J_0(u\xi). \tag{3.8}$$

The first term on the right hand side of Eq. (3.7) describes the non-scattered part of the electron beam: the probability that an electron does not scatter, after passing a thickness $t = $

$\lambda/(N\sigma)$, is given by $e^{-\lambda}$, according to the continuous Poisson distribution[8]. The probability that it scatters exactly n times is given by

$$P(n) = \frac{\lambda^n}{n!} e^{-\lambda}. \tag{3.9}$$

The second term on the right-hand side of Eq. (3.7) is therefore given by a summation of functions $g_n(\xi)/2\pi\chi_\alpha^2$, weighted by the probability that exactly n scattering events occur within a thickness of λ mean free paths. The function $g_n(\xi)/2\pi\chi_\alpha^2$ may thus be interpreted as the angular distribution after exactly n scattering events. Because the dependence on material properties and electron velocity only enters through χ_α, the function $g_n(\xi)$ is a universal distribution function. It only has to be calculated once, using Eq. (3.8), and can then be applied to any material and to any relativistic electron energy.
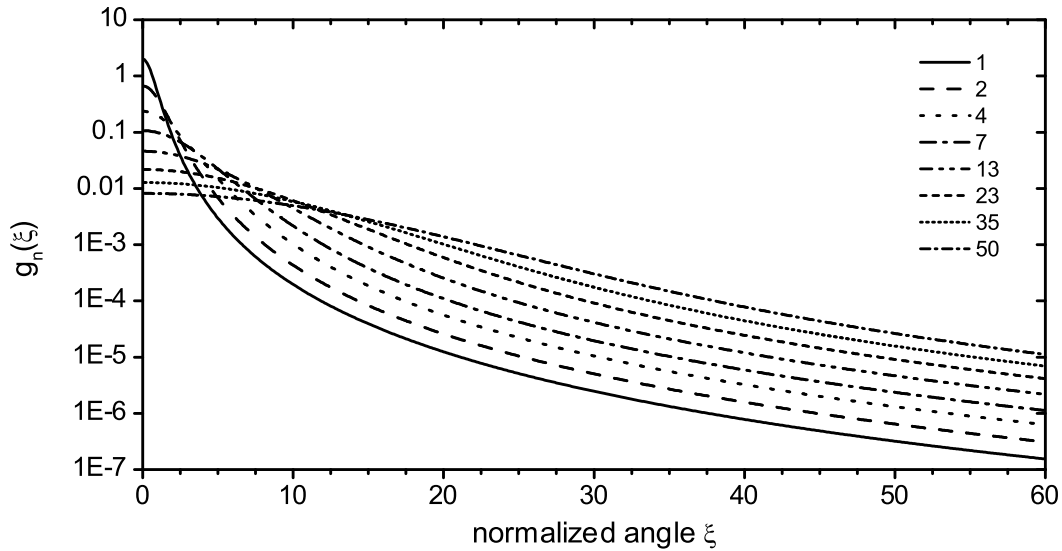

Figure 3.1: Angular distribution functions $g_n(\xi)$ representing a fixed number of scatterings as a function of normalized angle for number of scatterings of $n = 1$, 2, 4, 7, 13, 23, 35 and 50.

3.2.3   Numerical calculation and use of normalized distribution functions

In practice, the summation in Eq. (3.7) is truncated for a sufficiently large value of n. Typically, for a layer thickness t corresponding to $\lambda \le 35$, the summation has sufficiently converged for $n = 50$. For $\lambda > 35$, the scattering process is well into the multiple scattering regime, which is adequately described by Molière's theory. For this reason, we only need to calculate the universal distribution functions $g_n(\xi)$ up to $n = 50$.

The angular distribution functions $g_n(\xi)$ are calculated by evaluating the integral of Eq. (3.7), for $n = 1$ to 50. By definition the angular distribution function $g_1(\xi)$, which is the distribution function of one single scattering, is proportional to the screened Rutherford distribution:

$$g_1(\xi) = \frac{2}{\left(1 + \xi^2\right)^2}. \tag{3.10}$$

In addition, $g_2(\xi)$ can be evaluated analytically[7] by solving the integral in Eq. (3.8) for $n = 2$. For $n > 2$, the functions $g_n(\xi)$ have to be calculated numerically.

In Fig. 3.1, the universal distribution functions $g_n(\xi)$ are plotted as a function of the normalized angle ξ, for different values of the number of scattering events n. The functions $g_n(\xi)$ were calculated for $n = 1$ to 50, with ξ running from 0.1 to 60 with steps in ξ of 0.1, by numerically evaluating the integral given in Eq. (3.8). The upper limit of the integral was set at 20, which is sufficient for convergence. Because of the strong oscillatory behavior of the integrand of Eq. (3.8), very small integration steps have been taken.

Figure 3.2: Angular distribution functions $g_n(\xi)$ calculated by numerical evaluation of Eq. (3.8) (dotted curve) and by Monte Carlo simulations (solid curve), for a number of scatterings of $n = 1, 10, 25, 50$.

Monte Carlo simulations with the differential cross-section $d\sigma/d\Omega$ proportional to $1/(\sin^2(\theta/2) + \chi_\alpha^2)^2$ has been performed to check the validity of our approach. Thus, no small-angle approximation was applied in the Monte Carlo simulations, but energy loss has been neglected. In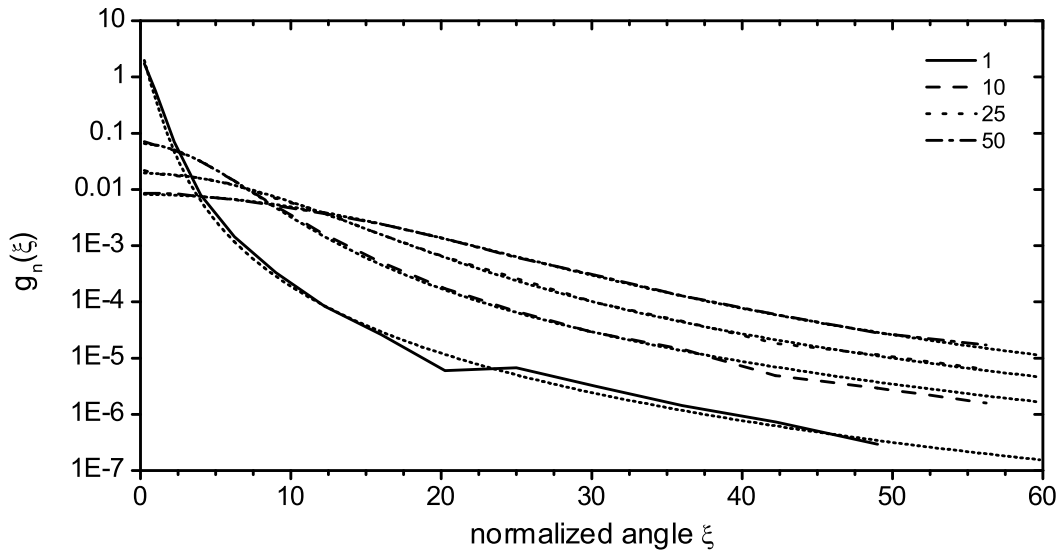 Fig. 3.2 the angular distribution functions $g_n(\xi)$ calculated by numerical evaluation of Eq. (3.8) and by Monte Carlo simulations, using 10^4 electrons, are plotted as a function of the normalized angle ξ. Good agreement is observed between the two curves, which justifies the small-angle approximation for the given range.

3.3   Scattering of electron beams with arbitrary angular distributions by multi-element foils.

The method described in the previous section is suitable for calculating the angular distribution, which results from scattering of a unidirectional electron beam by a single-element foil. In this section, the scattering is extended to electron beams of arbitrary angular distribution on multilayer structures. First in Sec. 3.3.1, scattering is presented for the case of an electron beam with an arbitrary angular distribution, scattered by a single-element foil. This requires a two-dimensional convolution between the incoming angular distribution, and the angular distribution, which results from scattering of a unidirectional beam. Second, in Sec. 3.3.2, the scattering is presented for the case of an incident unidirectional electron beam on a multilayer structure. Using the same 2-D convolution for all interfaces in the multilayer, this can be calculated for an arbitrary multilayer, i.e. a non-uniform 1-dimensional M-element system, with partial densities N_m, $(m = 1, .. ,M)$, cross-sections $d\sigma_m/d\Omega$, and total thickness t. In the small-angle approximation, a general 1-dimensional M-element system is equivalent to an M-multilayer system, each layer having a different element m and a thickness t, and density N_m. Finally, both can be combined to obtain the final electron distribution.
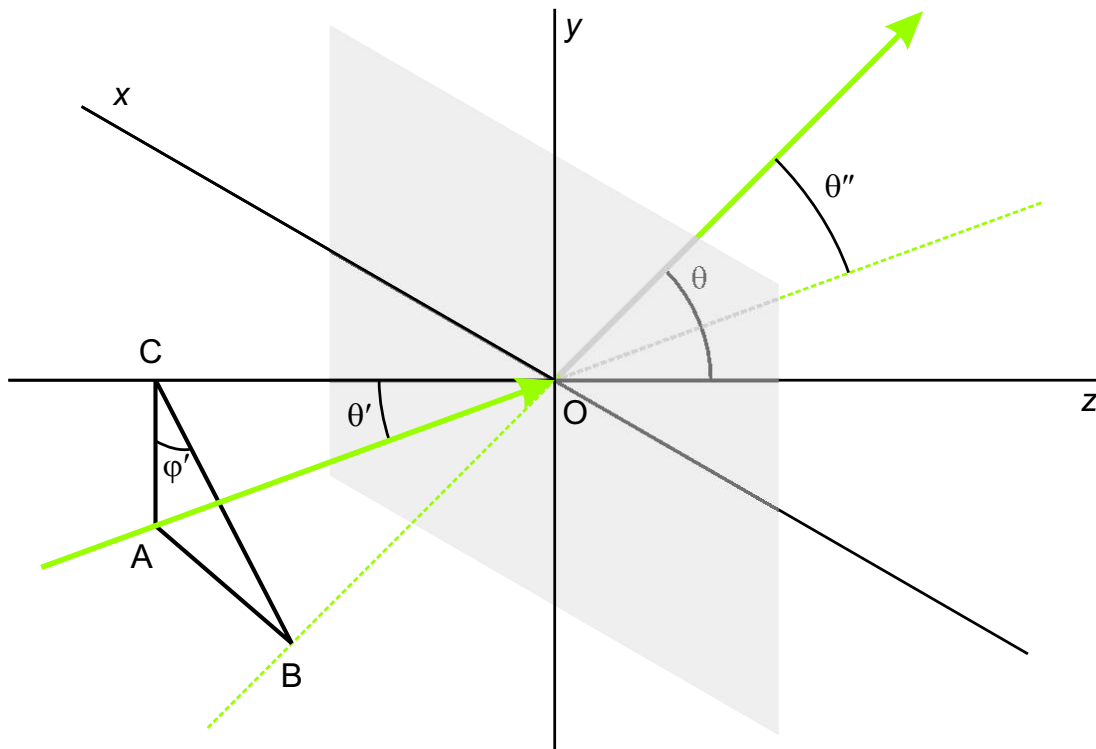

Figure 3.3: Geometric representation of scattering in a foil of a beam with angular distribution $h_0(\theta')$.

3.3.1   Scattering for arbitrary incoming angular distributions

Suppose an electron beam incident on a foil, with a cylindrically symmetrical angular distribution $h_0(\theta)$, centered around the z-axis (see Fig. 3.3). Let us define the direction of a specific incoming electron, in terms of a polar angle θ', with respect to the xyz-coordinate axes (see Fig. 3.3). The electron is scattered under a polar angle θ'' with respect to the incoming direction, and an azimuthal angle φ'. The scatter direction can also be described in terms of the angles θ and φ, with respect to the xyz-coordinate system. Let us now consider, without loss of generality, a fixed scatter direction θ, with $\varphi = 0$. One may then show straightforwardly that in the small angle approximation θ'', θ', θ, and φ' are related by (see Fig. 3.3)

$$\theta'' = \sqrt{\theta'^2 + \theta^2 - 2\theta'\theta\cos(\varphi')} \tag{3.11}$$

It follows now that if $f_0(\theta)$ is the angular scattering distribution with respect to the incoming direction of a unidirectional beam, then the angular scattering distribution function $f_1(\theta)$, for an arbitrary incoming angular distribution $h_0(\theta)$, is given by:

$$f_1(\theta) = \int_0^\infty d\theta'\,\theta'\,h_0(\theta')\int_0^{2\pi} d\varphi'\, f_0(\theta''). \tag{3.12}$$
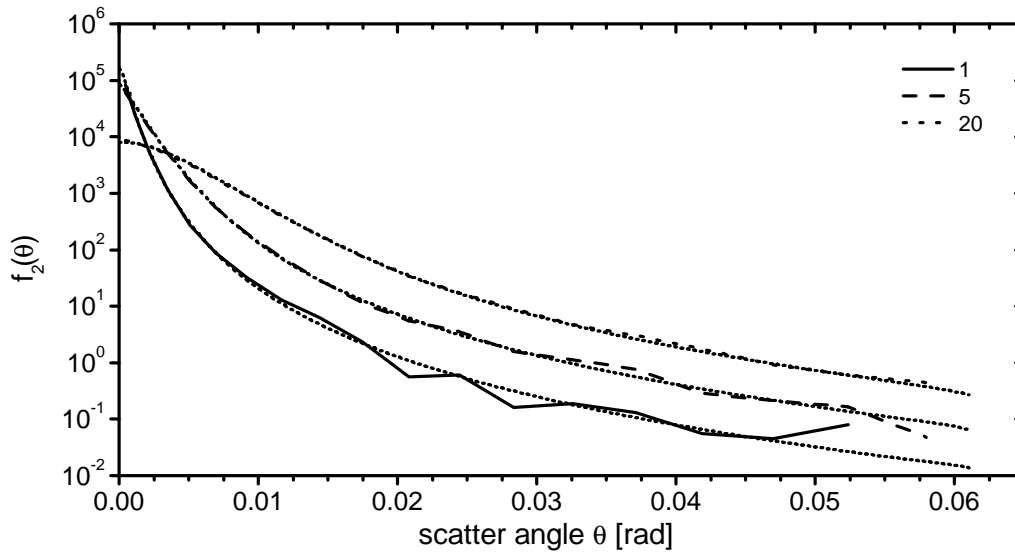
Figure 3.4: Angular distribution function $f_2(\theta)$ (dotted curve) and Monte Carlo simulations (solid curve) of a 10-MeV, unidirectional electron beam after passing, respectively, 1, 5 and 20 bilayers of 165.5-nm Al and 286.3-nm C.

3.3.2   Plural scattering in a two-element multilayer

Suppose a unidirectional electron beam passes through a multilayer. The resulting angular distribution $f_m(\theta)$ after layer m is then calculated by

$$f_m(\theta) = \int_0^\infty d\theta' \theta' f_{m-1}(\theta') \int_0^{2\pi} d\varphi' g_m(\theta''), \tag{3.13}$$

with $g_m(\theta)$ the angular distribution function of layer m for the case of a unidirectional electron beam. This recurrent algorithm is sensitive to cumulative errors. We can eliminate this error, in a structure of alternating layers, by re-ordering the layers in the calculation. All the layers of the same element are collected into one single layer; its thickness is the sum of the individual layers. For instance, a multilayer of 50 layer pairs can be reduced to a bilayer system in the calculation. This re-ordering is allowed, because the scattering process is a series of independent scattering events. As a result, the angular distribution for a bilayer is given by (see Appendix in Sec. 3.5):

$$f_2(\theta) = \frac{e^{-\lambda_A - \lambda_B}}{4\pi^2 \chi_{\alpha,A}^2 \chi_{\alpha,B}^2} \int_0^\infty d\theta' \theta' \sum_{n=1}^\infty \frac{\lambda_A^n}{n!} g_n(\xi_A') \int_0^{2\pi} d\varphi' \sum_{k=1}^\infty \frac{\lambda_B^k}{k!} g_k(\xi_B'') +$$

$$e^{-\lambda_B} \frac{e^{-\lambda_A}}{2\pi\chi_{\alpha,A}^2} \sum_{n=1}^\infty \frac{\lambda_A^n}{n!} g_n(\xi_A) + e^{-\lambda_A} \frac{e^{-\lambda_B}}{2\pi\chi_{\alpha,B}^2} \sum_{n=1}^\infty \frac{\lambda_B^n}{n!} g_n(\xi_B) + \frac{e^{-\lambda_A - \lambda_B}}{2\pi} \frac{\delta(\theta)}{\theta}. \tag{3.14}$$

The indices A and B are related to the two different layers. Four terms can be identified that contribute to the final distribution function. These terms refer to, respectively:

     (1) The electrons that are scattered in both foils.
     (2) The electrons that are scattered only in the first foil.
     (3) The electrons that are scattered only in the second foil.
     (4) The electrons that are neither scattered in the first nor in the second foil.

    Equation (3.14) is very efficient to follow the evolution of the angular distribution of an electron beam, passing through a multilayer structure, consisting of two elements. This is of relevance for the generation of resonant transition radiation[3,4].

    As an example, we have taken an Al-C multilayer with layer thicknesses of 165.5 nm and 286.3 nm, respectively. In Fig. 3.4, the angular distribution function $f_2(\theta)$ is plotted after 1, 5 and 20 bilayers of Al-C. These curves are calculated by Eq. (3.14) for a unidirectional beam of 10-MeV electrons, just by changing the λ_A and λ_B, according to the number of layers that have been passed. To validate this calculation, Monte Carlo simulations have been performed on these multilayer structures. Notice the good agreement between the simulations and the distribution function $f_2(\theta)$.

    The numerical evaluation of Eq. (3.14) has the difficulty that the normalized angles do not map θ the same way, because each layer has a different value of χ_α. The angular distribution function $f_2(\theta)$ can only be used up to the angle $\theta = 60\chi_\alpha$ for carbon, which has the smallest χ_α. To get a final distribution function that is accurate up to higher values of θ the $g_n(\xi)$ would have to be extended to larger values of ξ. Finally, the angular distribution after scattering of an arbitrary incident electron beam with angular distribution $h_0(\theta)$, passing through a multilayer structure, can now be calculated straightforwardly by the 2D-convoution (3.12) of $h_0(\theta)$ with the result of Eq. (3.14).

3.4   Conclusions

A new method was developed, which is suitable for calculation of angular elastic scattering distribution functions of single layers in the plural scattering regime and in part of the multiple scattering regime. Our method uses tabulated universal distribution functions $g_n(\xi)$, $n = 1, 2, \ldots$, which describe the angular distribution function after exactly n scattering events, as a function of the normalized angle $\xi = \theta/\chi_\alpha$ The parameter χ_α depends on the energy of the electrons and on material properties. The angular distribution functions $g_n(\xi)$ have been calculated for $n = 1$ to 50 for values of ξ ranging from 0.1 to 60 in steps of 0.1. The method is also suitable for performing calculations on (periodic) multilayers with a limited number of interfaces. The validity of our approach has been confirmed by Monte-Carlo simulations, which do not use the small-angle approximation.

3.5   Appendix: Angular distribution of a bilayer

The angular scattering distribution function of layer A, for the case of a unidirectional beam is given by Eq. (3.7):

$$f_A(\theta) = \frac{e^{-\lambda_A}}{2\pi\chi_{\alpha,A}^2}\left(\sum_{n=1}^{\infty}\frac{\lambda_A^n}{n!}\, g_n(\xi_A) + \frac{\delta(\xi_A)}{\xi_A}\right),\tag{3.15}$$

and the same holds for layer B, with A replaced by B and with the function $g_n(\xi_i)$ given by Eq. (3.8), which is tabulated.

The angular scattering distribution function of a multilayer, consisting of two layers, for the case of a unidirectional electron beam, is given by Eq. (3.13), with $m = 2$, and layer 1 equal to A, and layer 2 equal to B. Substituting Eq. (3.15) for layer A and layer B in Eq. (3.13) results in:

$$f_2(\theta) = l\int_0^{\infty} d\theta'\,\theta'\left(\sum_{n=1}^{\infty}\frac{\lambda_A^n}{n!}\, g_n(\xi_A') + \frac{\delta(\xi_A')}{\xi_A'}\right)\int_0^{2\pi} d\varphi'$$

$$\left(\sum_{k=1}^{\infty}\frac{\lambda_B^k}{k!}\, g_k(\xi_B'') + 2\pi\delta(\varphi')\frac{\delta(\xi_B'')}{\xi_B}\right),\tag{3.16}$$

with

$$l = \frac{e^{-\lambda_A-\lambda_B}}{4\pi^2\chi_{\alpha,A}^2\chi_{\alpha,B}^2}\,.\tag{3.17}$$

Note that the distribution function $f_B(\theta)$ is integrated over the azimuth φ. Therefore, the proper substitution of the Dirac delta function has to be made: $2\pi\delta(\varphi)\delta(\xi_B'')/\xi_B$.

Expanding Eq. (3.16), the angular scattering distribution function $f_2(\theta)$ is the sum of four terms. The first term is:

$$l\int\limits_{0}^{\infty} d\theta'\theta'\sum_{n=1}^{\infty}\frac{\lambda_{A}^{n}}{n!}g_{n}(\xi_{A}')\int_{0}^{2\pi}d\varphi'\sum_{k=1}^{\infty}\frac{\lambda_{B}^{k}}{k!}g_{k}(\xi_{B}'').\tag{3.18}$$

The second term:

$$2\pi l\int\limits_{0}^{\infty} d\theta'\theta'\sum_{n=1}^{\infty}\frac{\lambda_{A}^{n}}{n!}g_{n}(\xi_{A}')\frac{\delta(|\xi_{B}'-\xi_{B}|)}{\xi_{B}}=2\pi\chi_{\alpha,B}^{2}\,l\sum_{n=1}^{\infty}\frac{\lambda_{A}^{n}}{n!}g_{n}(\xi_{A}).\tag{3.19}$$

The third term:

$$l\int\limits_{0}^{\infty} d\theta'\theta'\frac{\delta(\xi_{A}')}{\xi_{A}'}\int_{0}^{2\pi}d\varphi'\sum_{k=1}^{\infty}\frac{\lambda_{B}^{k}}{k!}g_{k}(\xi_{B}'')=2\pi\chi_{\alpha,A}^{2}\,l\sum_{n=1}^{\infty}\frac{\lambda_{B}^{n}}{n!}g_{n}(\xi_{B}).\tag{3.20}$$

The fourth term:

$$l\int\limits_{0}^{\infty} d\theta'\theta'\frac{\delta(\xi_{A}')}{\xi_{A}'}\int_{0}^{2\pi}d\varphi'2\pi\delta(\varphi')\frac{\delta(\xi_{B}'')}{\xi_{B}}=2\pi\chi_{\alpha,A}^{2}\,l\frac{\delta(\xi_{B})}{\xi_{B}}.\tag{3.21}$$

References

1 W. Knulst, O.J. Luiten, M.J. van der Wiel and J. Verhoeven, "Observation of narrow band Si L-edge Cerenkov radiation generated by 5-MeV electrons", *Appl. Phys. Lett.* **79**, 2999 (2001).

2 W. Knulst, M.J. van der Wiel, O.J. Luiten and J. Verhoeven, "High-brightness, narrowband, and compact, soft x-ray Cherenkov sources in the water window", *Appl. Phys. Lett* **83**, 4050-4052 (2003).

3 B. Lastdrager, A. Tip and J. Verhoeven, "Theory of Cherenkov and transition radiation from layered structures", *Phys. Rev.* **E61**, 5767-5778 (2000).

4 A.E. Kaplan, C.T. Law and P.L. Shkolnikov, "X-ray narrow line transition radiation source based on low energy electron beams traversing a multilayer nanostructure", *Phys. Rev.* **E52**, 6795-6808 (1995).

5 G. Molière, "Theorie der Streuung schneller geladener Teilchen I", *Z. Naturforsch.* **2a**,133 (1947).

6 H.A. Bethe, "Molière's Theory of Multiple Scattering", *Phys. Rev.* **89**, 1256 (1953).

7 A.F. Bielajew, "Plural and multiple small-angle scattering from a screened Rutherford cross-section", *Nucl. Instrum. Methods* **B86**, 257 (1994).

8 X. Ning, L. Papiez and G. Saudison, "Compound Poisson process method for the multiple scattering of charged particles", *Phys. Rev.* **E52**, 5621 (1995).

9 This database is available at the TU/e-website: http://www.ftv.phys.tue.nl/research/Cherenkov/Cherenkov_Index.html

4   Experimental setup

The main objective of the experiments is to prove that moderately relativistic electrons generate Cherenkov radiation in the soft x-ray spectral region. These experiments should confirm the characteristics of the soft x-ray Cherenkov radiation, which are predicted by theory as is discussed in Chapter 2. Two experimental setups have been used: a setup with 5-MeV electrons (Sec. 4.1.1) and one with 10-MeV electrons (Sec. 4.2.1). The first setup is used to demonstrate that an electron energy as low as 5 MeV is already sufficient to generate silicon L-edge Cherenkov radiation with sufficiently high yield. The latter setup is used to investigate Cherenkov-emitting materials in the water-window spectral region that have not been observed before. These materials require 10-MeV electrons.

The soft x-ray Cherenkov radiation is experimentally characterized on three main aspects, i.e. photon energy, angular profile and photon yield. For each setup a dedicated detection system has been used. The silicon L-edge Cherenkov radiation is analyzed by a crude spectrometer based on a multilayer mirror (Sec. 4.1.3) and photodiode (Sec. 4.1.4). The water-window Cherenkov radiation is detected by a dedicated soft x-ray CCD camera, which is able to determine the spectrum of the radiation (Sec. 4.2.3).

During all the measurements the separation of the soft x-ray radiation from the background played a crucial role. This background originates from two sources, namely the part that is generated in the target foil, such as Bremsstrahlung, transition radiation and fluorescence radiation, and the part consisting of penetrating x-rays that is generated everywhere the electron beam is stopped or lost. Each detection system is designed to enable a specific background correction method. Especially in case of the spectrometer, the understanding of the background contribution to the photodiode signal has occupied quite a long time. In case of the CCD camera the separation of the soft x-ray part from the background was relatively simple due to the photon-counting operation mode, in which both are spectrally distinguished. However, the soft x-ray CCD camera could not be used to detect silicon L-edge Cherenkov radiation, because the photon energy is too low as is explained in Sec. 4.2.3.
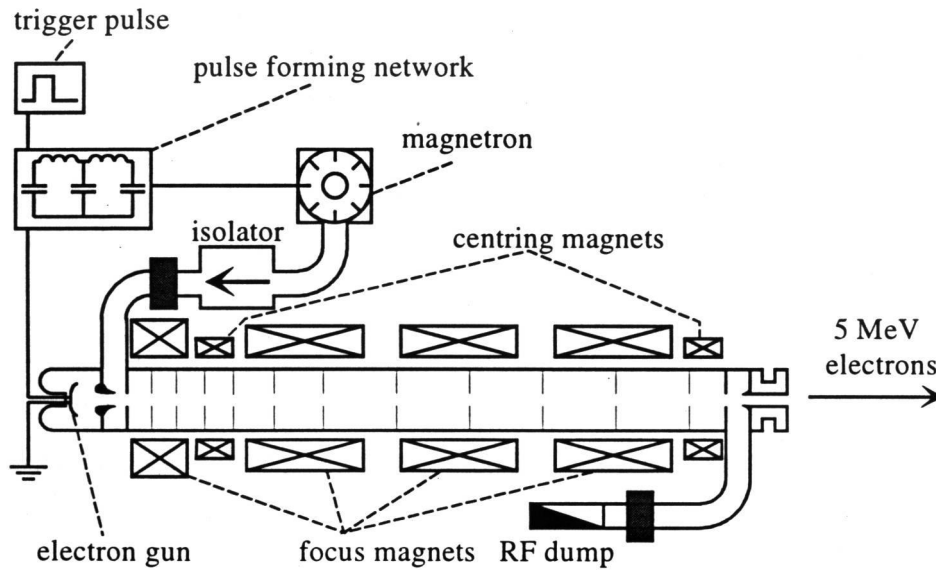
Figure 4.1: Schematic layout of the LINAC-5. Electrons are generated by the thermionic gun and accelerated by a traveling RF wave in the waveguide, while being focused by solenoidal magnets.

4.1 5-MeV electron accelerator setup

4.1.1 LINAC-5

The 5-MeV electrons are produced by a traveling wave linear accelerator (LINAC)[1], which is part of a former medical radiation treatment machine (M.E.L.* SL75/5). In Fig. 4.1 a schematic overview of the accelerator is given. A high-voltage pulse (40 kV) is generated by a modulator and sent to the magnetron and the electron gun. The frequency of these pulses can be set with a pulse generator from single up to 300 Hz. The magnetron produces a 2-MW, 3-GHz RF pulse of 4-µs duration, which is sent through a rectangular waveguide to the accelerator tube, which is a circular disk-loaded traveling waveguide. The electrons are generated by a thermionic gun and injected into the tube by the high-voltage pulse. The heating current through the electron gun filament determines the electron emission and thereby the electron beam current. This accelerator can produce electrons with energies between 4 MeV and 6 MeV with an energy spread of about 4%. The solenoidal magnets around the tube focus the beam. At the beginning and end of the tube two sets of centering magnets are mounted to control the direction of the electron beam.

4.1.2 Foil chamber and detection unit

Directly at the end of the accelerator tube the experimental setup is placed, which is shown in Fig. 4.2. The electron beam is focused by the solenoids of the accelerator to a spot size of

---

* This company has been taken over by Elekta: http://www.elekta.com

about 2 mm on the silicon target foil. After the beam has passed through the foil a dipole magnet bends the electron beam downwards. A set of three quadrupoles focuses the beam onto a beam dump, where the current is measured. When the electron beam is stopped Bremsstrahlung is emitted in the forward direction of the beam. Because the electron beam is directed downwards, this intense hard x-ray radiation is absorbed into the floor.
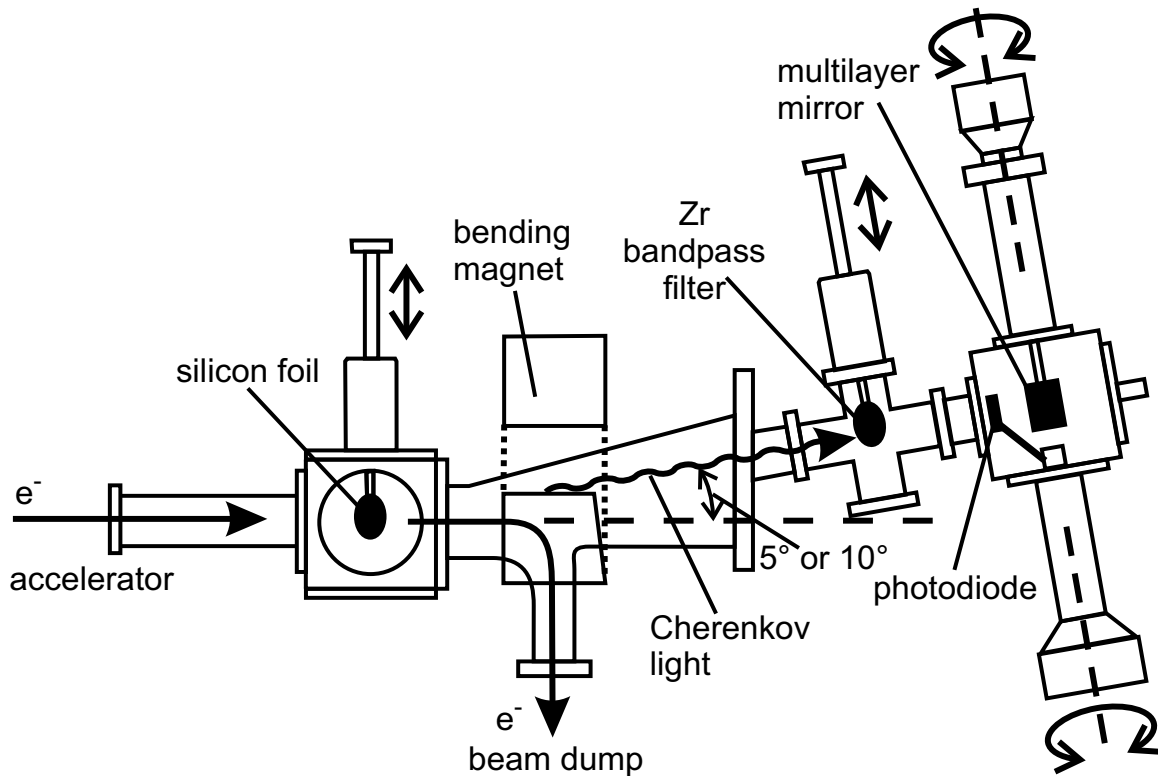

Figure 4.2: Side view of the experimental setup, which is placed directly behind the LINAC-5.

The narrow gap in the iron yoke of the dipole magnet allows only a slice of the full Cherenkov cone to be analyzed. The flat vacuum chamber, which fits into the dipole magnet gap, has a triangular shape (see Fig. 4.2). The vacuum chamber has several observation ports, which enable analysis of the Cherenkov radiation at fixed angles $\Theta = 2°$, 5° and 10°.

The detection unit consists of two parts. In the first part, a filter can be inserted into the photon path by means of a linear motion feedthrough. A 150-nm zirconium bandpass filter (Luxel Inc.[2]), which has a transmission of 55% for 100-eV radiation, is used to block visible (transmission $= 5\times10^{-6}$) and ultraviolet transition radiation that is also generated at the target foil. In the second part, a Mo/Si-multilayer mirror and a silicon photodiode are mounted on two vacuum rotation feedthroughs in a "theta-2theta" configuration (see Fig. 4.3), thus forming a crude spectrometer. The multilayer mirror is a wavelength dispersive element, which is explained in Sec. 4.1.3. By changing the angle of incidence a different wavelength is reflected. This reflected signal is then measured with an absolutely calibrated photodiode, which is presented in Sec. 4.1.4.

4.1.3 Multilayer mirror

A multilayer mirror[3] is an interference coating consisting of multiple, alternating layers of two materials of different refractive index, deposited on a substrate. Typically, the two materials are of alternating high and low atomic number in order to maximize the difference in electron density. In the soft x-ray region the multilayer mirrors are the only optics available with sufficiently high reflectivity at normal incidence (5-70%). The reflection of soft x-ray radiation by multilayer interference coatings is described by Bragg's law,

$$2d \cos \theta_i = m\lambda \tag{4.1}$$

with d the period thickness (i.e. one bilayer pair), θ_i the angle of incidence measured with respect to the normal of the multilayer and m the diffraction order. By changing the angle of incidence the reflection profile shifts in wavelength. Therefore the multilayer can be used as a dispersive element in a spectrometer.
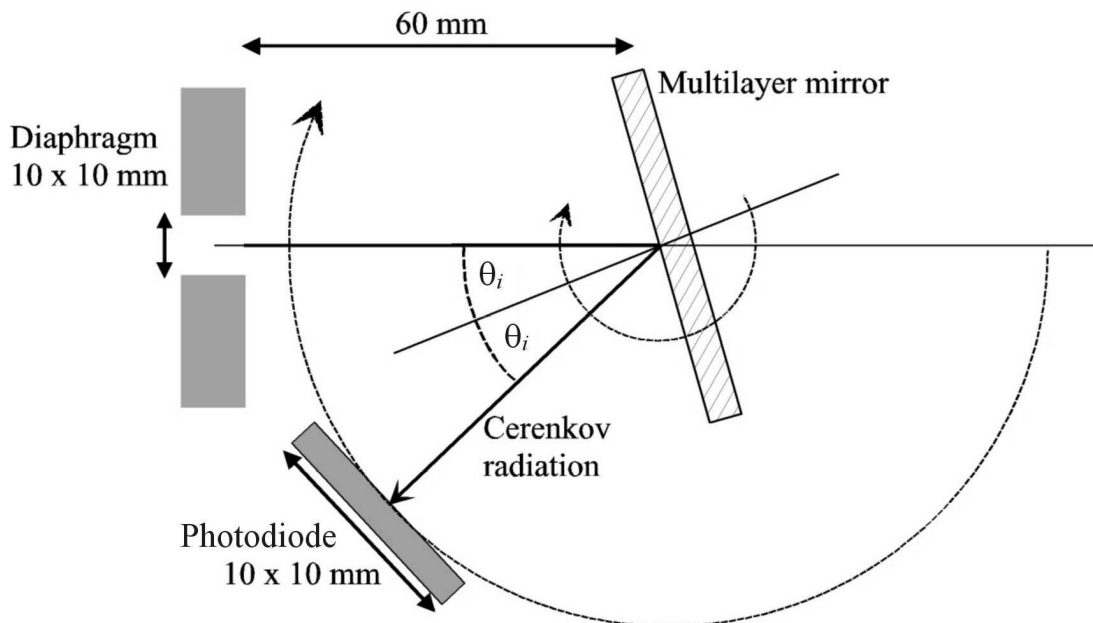

Figure 4.3: The top view of the spectrometer consisting of a multilayer mirror and a silicon photodiode in θ-2θ configuration.

The spectral reflection bandwidth of these mirrors is of order $1/N_m$, where N_m is the number of layer pairs, typically between 30 and 50 for high reflectivity. The complete reflection profile as function of wavelength can be calculated by using the CXRO-webpage[4] of the Lawrence-Berkeley-Laboratory website. A very successful multilayer mirror is the combination of molybdenum and silicon, which has reflectivity of nearly 70% at normal incidence for 13.5-nm radiation[3].

In the spectrometer a Mo/Si-multilayer mirror is used, which is supplied by the FOM-institute for Plasma Physics[†]. The mirror specifications are listed in Table 4.1. For simulations of these mirrors, the interdiffusion thickness is adjusted to fit the calculated

---

[†] FOM-institute for Plasma Physics, Nieuwegein, The Netherlands, http://www.rijnh.nl

reflectivity to the measured value. In Fig. 4.4 the reflectivity profiles calculated using Ref. 4 are plotted as function of photon energy for several angles of incidence. Due to the silicon absorption edge the reflection profiles are strongly dependent on the angle of incidence. The silicon Cherenkov radiation is mainly generated at photon energies between 98 eV and 100 eV (see Fig. 2.4). The Mo/Si multilayer mirror reflects this radiation at angles of incidence ranging from 20° to 28º. The widths of the reflection profiles, and thus the resolution of the spectrometer, are on average about 3 eV. This is in the same order of magnitude as the spectral width of the generated Cherenkov radiation.
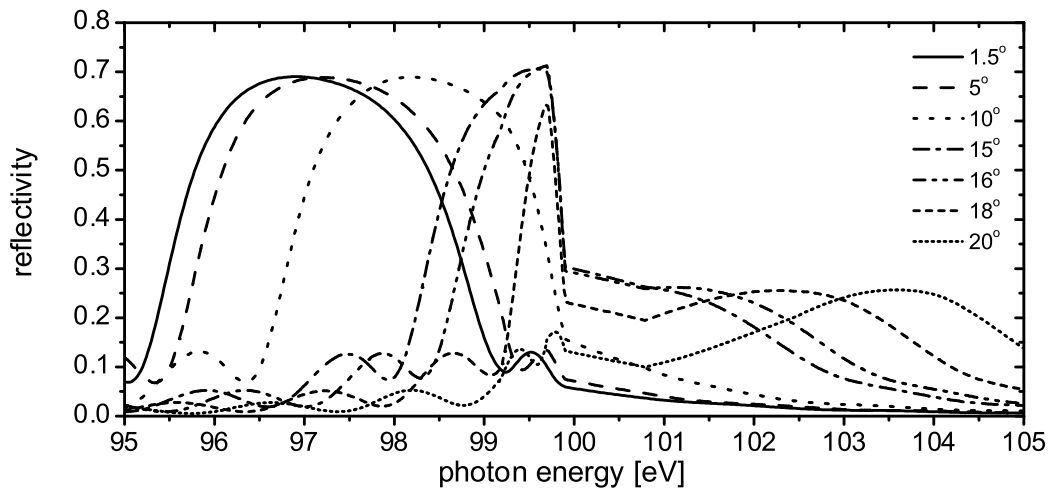

Figure 4.4: The calculated reflectivity of the Mo/Si-multilayer mirror with parameters specified in Table 4.1 as a function of photon energy for different angles of incidence θ_i.

Table 4.1: Parameters of the Mo/Si and Mo/B$_4$C-multilayer mirror.

	Mirror 1	**Mirror 2**
top layer material	Mo	Mo
bottom layer material	Si	B$_4$C
multilayer period	6.52 nm	7.44 nm
ratio of bottom/period	0.617	0.5
number of periods	51	50
substrate material	Si	Si
measured reflectivity	68%	53%
at specified wavelength	12.8 nm	6.76 nm
at specified angle of incident θ_i	1.5°	27.03°
interfusion thickness	0.76 nm	0.1 nm

This multilayer spectrometer only supplies spectral information between 98 eV and 99.7 eV. Lower photon-energies than 98 eV cannot be measured, because geometric constraints

limit the minimal angle of incidence θ_i (see Fig. 4.3). Higher photon-energies than 99.7 eV cannot be measured, because the reflectivity of the multilayer mirror decreases due to the silicon L absorption-edge (see Fig. 4.4). In order to obtain spectral information beyond the L-edge, a multilayer mirror has to be used with another material than silicon. The multilayer combination of Mo and B_4C will provide the required reflectivity around 100 eV. This material combination has been used before to make multilayer mirrors. In Table 4.1 the parameters are given of the Mo/B_4C-multilayer mirror purchased at Osmic Inc.[5]. The calculated reflectivity as a function of photon energy for several angles of incidence are shown in Fig. 4.5. The shape of the different profiles is very constant. The optimal reflectivity of the mirror for silicon L-edge Cherenkov radiation is expected at 27°. The spectral resolution of this mirror is about 3 eV. The maximum reflectivity ($\approx 30\%$) of this mirror is less than the Mo/Si-multilayer mirror. Although this mirror has been purchased, Cherenkov measurements have not yet been performed.
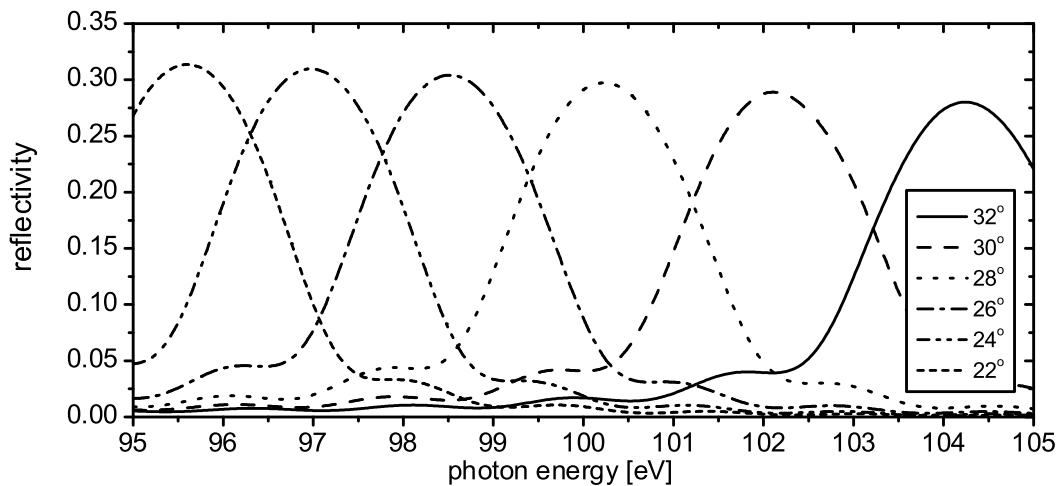

Figure 4.5: The calculated reflectivity of the Mo/B_4C-multilayer mirror with parameters specified in Table 4.1 as a function of photon energy for different angles of incidence θ_i.

4.1.4 Silicon soft x-ray photodiode

A silicon photodiode with a sensitive area of 10×10 mm^2 is used to detect the radiation reflected from the multilayer mirror. This silicon p-n-junction photodiode of the AXUV-100 series purchased from International Radiation Detectors (IRD) Inc.[6] has been developed for applications in the vacuum ultraviolet, extreme ultraviolet and soft x-ray spectral region. Unlike common p-n junction diodes, these diodes do not have a doped dead-region. Because the absorption length in silicon is less than 1 μm for photon energies lower than 700 eV, the absence of this dead region yields complete collection of the photo-generated carriers resulting in 100% carrier collection efficiency and a nearly theoretical quantum efficiency of about 3.7 eV per electron-hole pair. In Fig. 4.6 the quantum efficiency of the AXUV photodiode is plotted as a function of photon energy. The AXUV diodes are internal

photoelectric devices and are therefore less sensitive to surface contamination than conventional detectors based on the external photoelectric effect.

These photodiodes are available with an integrated filter deposited on top of the diode surface to suppress the sensitivity to visible radiation with a few orders of magnitude and providing a bandpass around certain photon energies depending on the filter materials. In combination with the Mo/Si-multilayer mirror a Si/Zr filter is used with layer thicknesses of, respectively, 100 nm and 200 nm (see solid curve in Fig. 4.6). This diode with integrated Si/Zr filter has a quantum efficiency of about 5 electrons per photon at 99 eV. However, due to the silicon in the filter the quantum efficiency drops enormously for photon energies higher than the L-edge and therefore the spectrometer has no sensitivity in this spectral region. When using the Mo/B$_4$C-multilayer mirror a filter without silicon has to be selected to extend the spectrometer sensitivity to higher photons energies. The combination of Ti, Zr, and C with layer thicknesses of, respectively, 6 nm, 200 nm and 50 nm, gives a continuous quantum efficiency of about 8 electrons per photon around 100 eV (see dotted curve in Fig. 4.6).
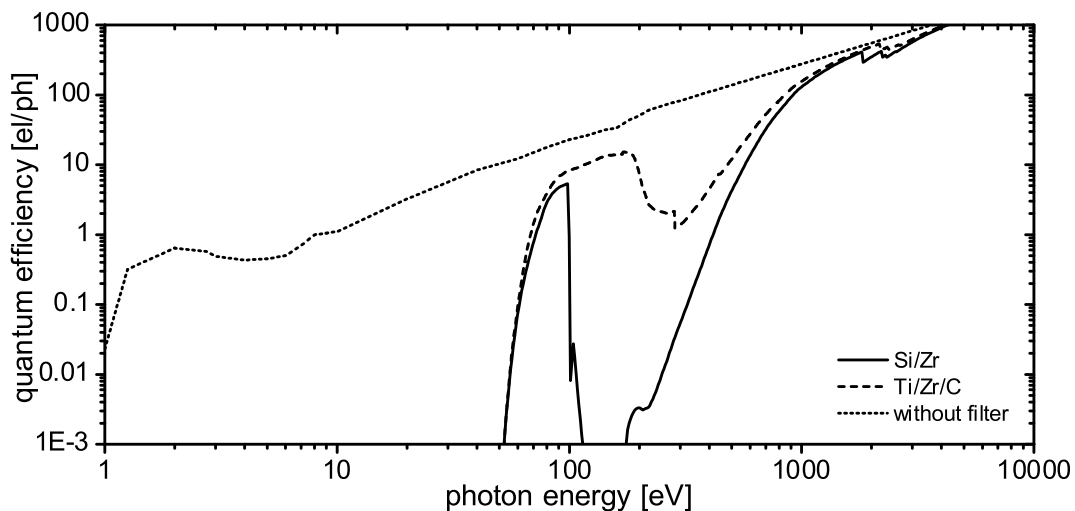

Figure 4.6: Quantum efficiency of the AXUV-100 photodiode without filter (dotted curve), with 100-nm Si/ 200-nm Zr filter (solid curve) and with 6-nm Ti/ 200-nm Zr/ 50-nm C filter (dashed curve).

The quantum efficiency of these photodiodes (without filter) increases proportionally to the photon energy up to approximately 6 keV. For higher photon-energies the diode starts to become transparent and the quantum efficiency drops again. The high sensitivity to hard x-rays makes it impossible to put the photodiode directly into the Cherenkov radiation cone. In this case the contribution of the narrow Cherenkov line to the photodiode current is very small compared to the integrated contribution of the Bremsstrahlung radiation. Therefore, the multilayer mirror serves a second purpose besides the spectral information: it also spatially separates the Cherenkov radiation from the high photon-energy background radiation, because the latter is not reflected by the mirror.

The photodiodes are used without bias voltage and with the cathode (n-region) grounded. The signal is read from the anode (p-region). The photodiode current is converted to a voltage, which is digitally recorded. This converter is a trans-impedance amplifier with a time constant of 0.3 s and an equivalent resistance of 1 GΩ (note that the actual input impedance of the converter is very low), which gives 1 V per nA[7].

4.2   10-MeV electron accelerator setup

4.2.1   LINAC-10 and bending section

The 10-MeV electrons are generated by a LINAC-10 (M.E.L. SL75/10), which is of the same type as the LINAC-5. The RF pulse length is 2 μs. The electron beam energy can be varied from 9 to 11 MeV by changing the beam current, which is determined by the gun filament current. The energy spread is also 4%.
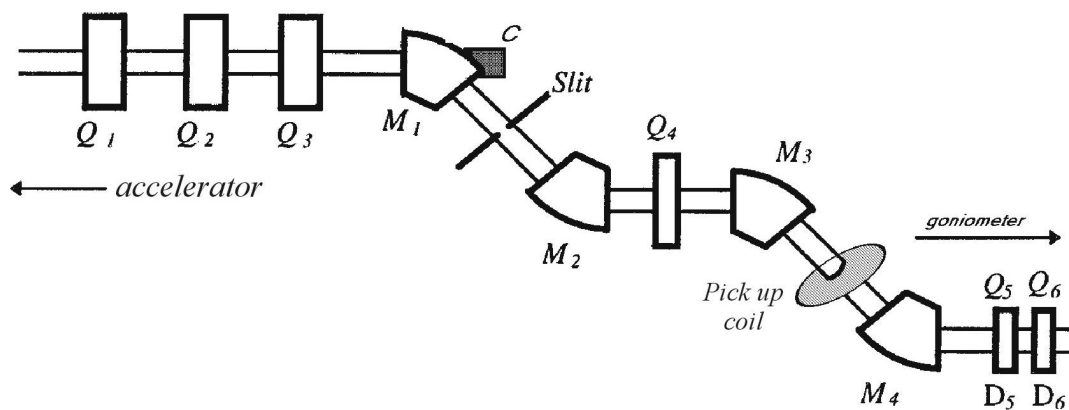

Figure 4.7: Schematic overview of the double achromatic bending section, which is directly placed after the accelerator. It contains 4 dipole magnets (*M*), 6 quadrupoles (*Q*) and two steering dipoles (*D*).

After acceleration the electron beam passes through a double achromatic bending section (see Fig. 4.7). This bending section was originally designed as the injection beamline from the LINAC-10 into a racetrack microtron[8] to bridge a height difference. The beamline consists of 4 bending magnets to make the passage of the electron beam achromatic. Additionally, two sets of quadrupoles before and after the bending section allow focusing of the electron beam onto the target foil.

4.2.2   Goniometer

A goniometer has been used to take angular scans of the soft x-ray Cherenkov radiation in the 10 MeV setup. The goniometer is a device that rotates the CCD-camera at a fixed distance from the foil in the vertical plane as is shown schematically in Fig. 4.8. The target foil is thus the center of rotation of the goniometer. The angular range extends from $\Theta = -20°$ to $\Theta = +20°$, which amply covers the emission range of Cherenkov radiation from various materials.

The angular resolution of the goniometer depends on four parameters: the source size (which is determined by the electron beam spot size), the electron beam divergence (because the Cherenkov radiation is emitted with respect to the electron direction), the distance from the source to the detector and the detector area. The distance from the source to the detector is 1 m, which gives, in combination with a 1-mm source diameter, an angular resolution of 1 mrad. The area of the used pixels on the CCD chip determines the detector area. Limiting the electron beam divergence to 1 mrad is much more difficult, because the electron beam is elastically scattered while passing through the target foil. Typically, to stay in the order of 1-mrad RMS scattering angle for 10-MeV electrons the thickness has to be less than 5 nm for the case of aluminum[9]. During the experiments presented in this thesis no attempts were made to optimize the angular resolution.
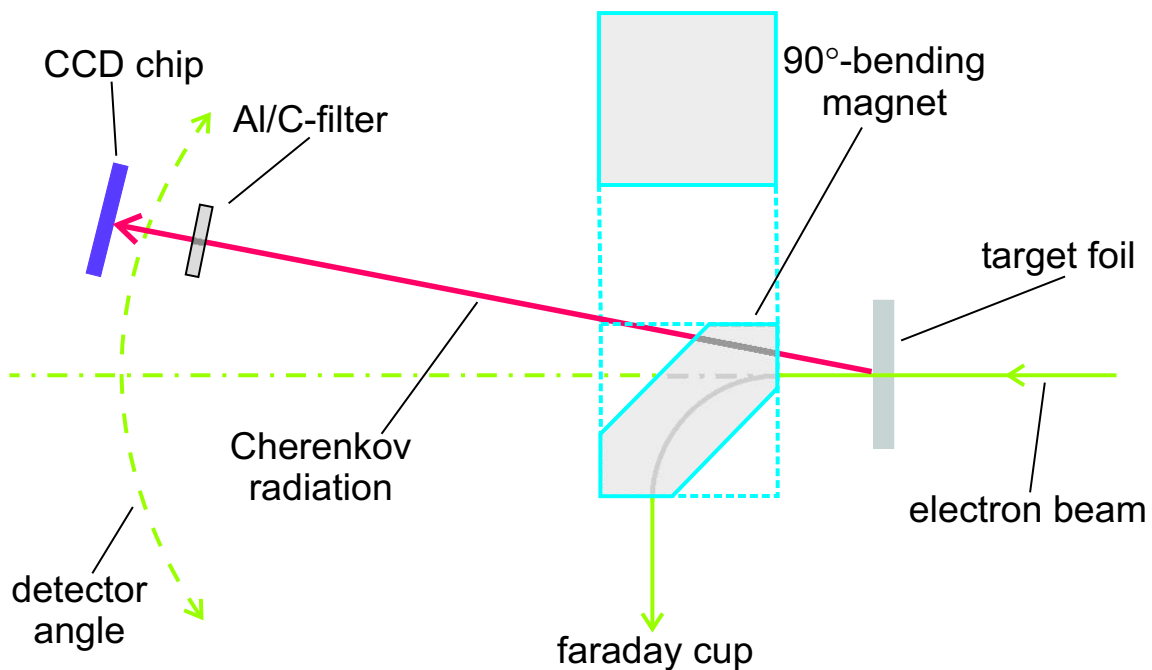

Figure 4.8: Schematic overview of the goniometer setup. The electron beam enters from the right.

During the design process of the goniometer (see Fig. 4.9) three technological issues had to be solved. The first issue is the fact that the electron beam trajectory is fixed and the detector position has to be varied while both are part of the same vacuum system. The solution is found by placing the target foil in the center of bellows, which allows the detector to move along an arc. By making this choice a specially shaped vacuum chamber is needed to accommodate the trajectory of the electron beam through the bending magnet at all goniometer angles.

The second issue is the influence of the magnetic field of the bending magnet at the position of the target foil, which could influence the electron beam trajectory through the foil. This would suggest placing the magnet at large distance, but then the size of the bellows becomes too large. Therefore, the magnet coils are shielded by iron to decrease the fringe field. Calculations showed that iron shielding around the coils is effective in reducing the fringe field of the magnetic field.

In Fig. 4.10 a contour map of the magnetic field is shown, which is based on a 2D-scan measured in the center of the gap at a fixed current. Clearly the shape of the pole is visible. In principle it is a square-shaped pole, which is a normal 90°-bending magnet where the electron beam enters and exits the magnetic field perpendicularly. To save space the corners far from the electron beam trajectory are cut off. The measured magnetic field strength at 10.0 cm from the magnet center (at horizontal = 350 mm and vertical = 23.5 mm in Fig. 4.10) is 15 Gauss. This value is low enough and does not influence the electron beam direction at the target foil position.
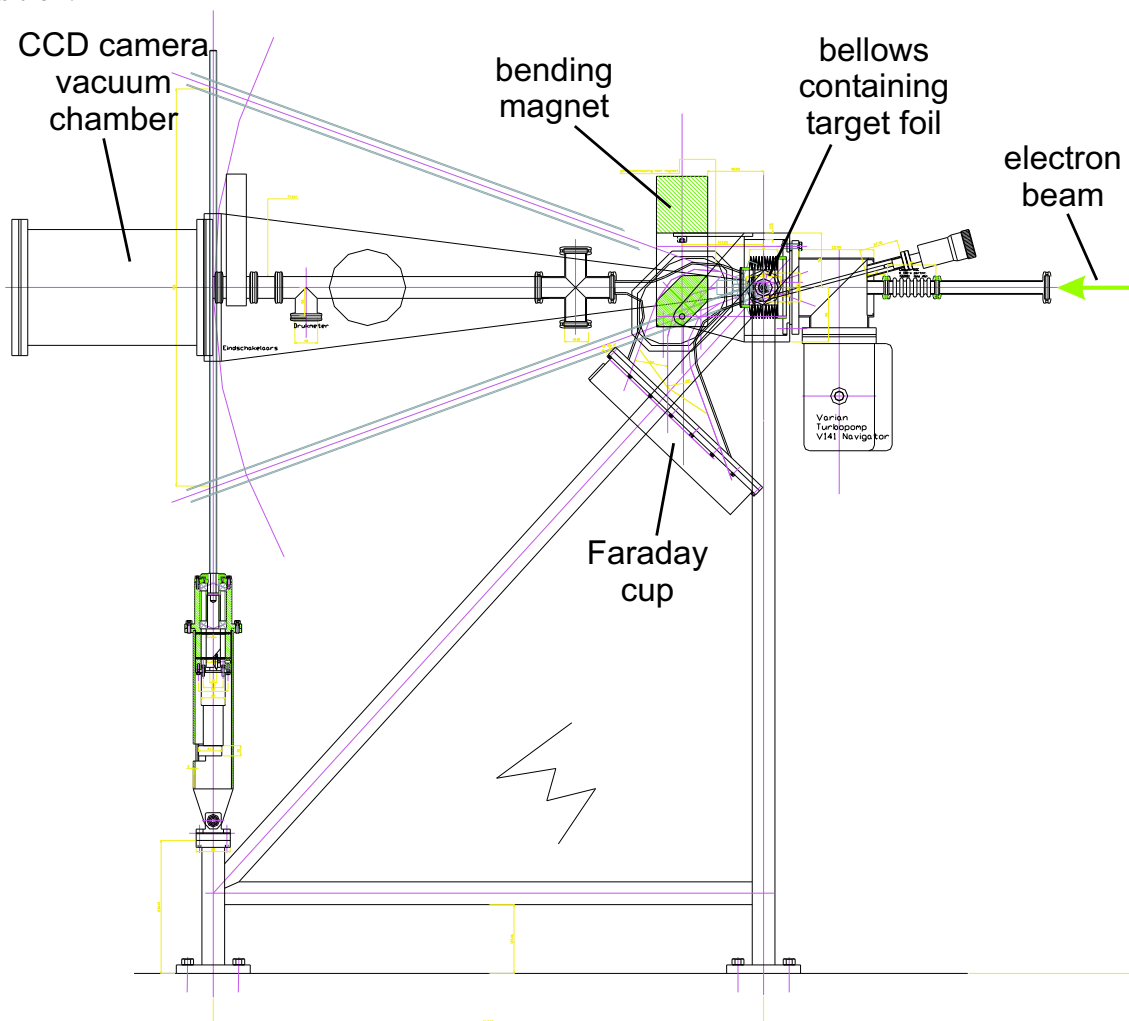

Figure 4.9: Design drawing of the goniometer. The electron beam enters from the right. The large vacuum chamber on the left contains the CCD camera.

The third issue is the mounting of the target foils in the goniometer, to enable grazing incidence. The thin foils are generally very fragile, but changing of the foil should be rather easy. Therefore, the foils are first mounted on robust frames before being inserted into the goniometer. These frames have two legs that act as leaf springs. By mounting the foil under a little tension, the surface of the foil will be flat. When the frame is mounted in the goniometer, the foil can be rotated via a linear feedthrough to any orientation from perpendicular to

parallel with respect to the electron beam. This allows the investigation of Cherenkov radiation under oblique incidence of the electron beam.
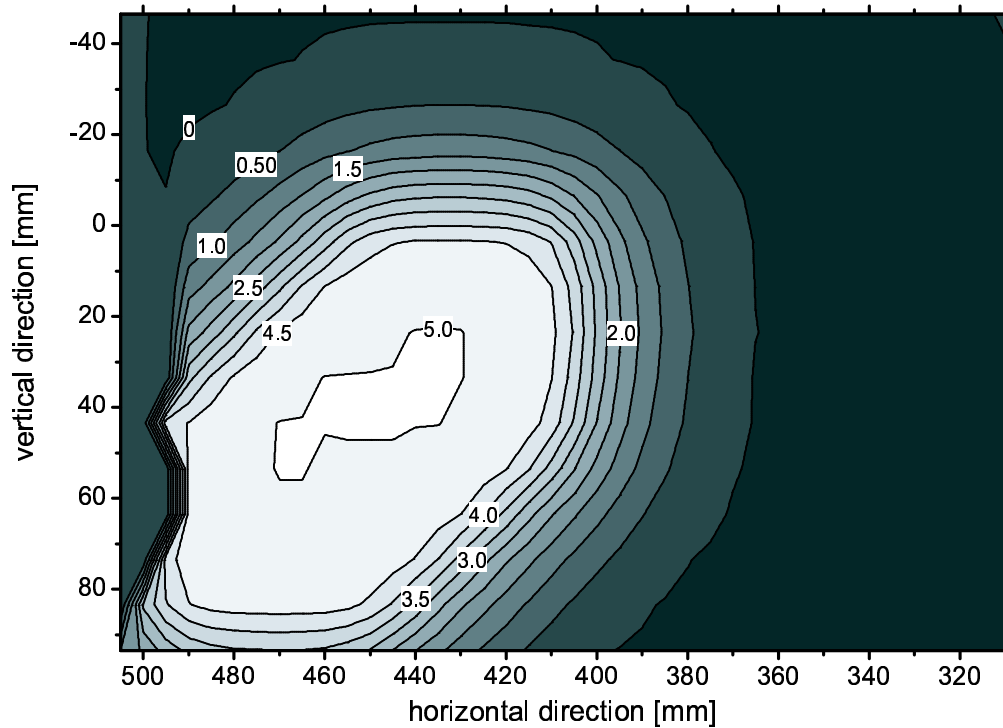

Figure 4.10: The contour map of the magnetic field [kGuass] in the center of the gap of the shielded magnet based on a 2D scan. From the right the electron beam enters the magnet and is bent down. The measurement points on the left are missing, because the probe was too short to reach these coordinates.

4.2.3   Soft x-ray CCD camera

For the detection of water-window Cherenkov radiation a dedicated soft x-ray CCD (Charge Coupled Device) camera has been used, which was developed by Space Research Organization Netherlands for x-ray astronomy[10]. The CCD chip is a copy of the chips that are used in the European XMM-Newton satellite. The special feature of the camera is the ability to determine the photon energy of each individual photon that is detected. The spectral width of the soft x-ray Cherenkov radiation ($\approx$ 1 eV) is much smaller than the spectral resolution of the CCD chip. Nevertheless, it is possible to measure the Cherenkov radiation energy, because it contains only one strong peak in the soft x-ray region.

4.2.3.1   CCD Detection Principle

The CCD chip ($28.0{\times}25.4$ mm^2) is a $1024{\times}768$ matrix of 27-μm square pixels. In order to achieve a greater than 80% detection efficiency down to the lowest energy of about 350 eV, the CCD is back-illuminated, because the gate structure at the front side absorbs too many photons at these energies. Figure 4.11[11] shows a cross section of the CCD chip. The photons

are incident from the left, which is the backside. In one pixel the process of photon detection is similar to the silicon photodiode (Sec. 4.1.4). The thickness of the CCD has to be at least 23 μm to reach a detection efficiency of 80% or higher for photon energies just below the silicon K-edge ($l_{abs} \approx 15$ μm). On the other hand, a very thick CCD chip makes it too sensitive to hard x-rays and high-energy particles. The sensitivity of the silicon photodiode for hard x-rays applies also to the CCD chip, because the thickness is comparable.
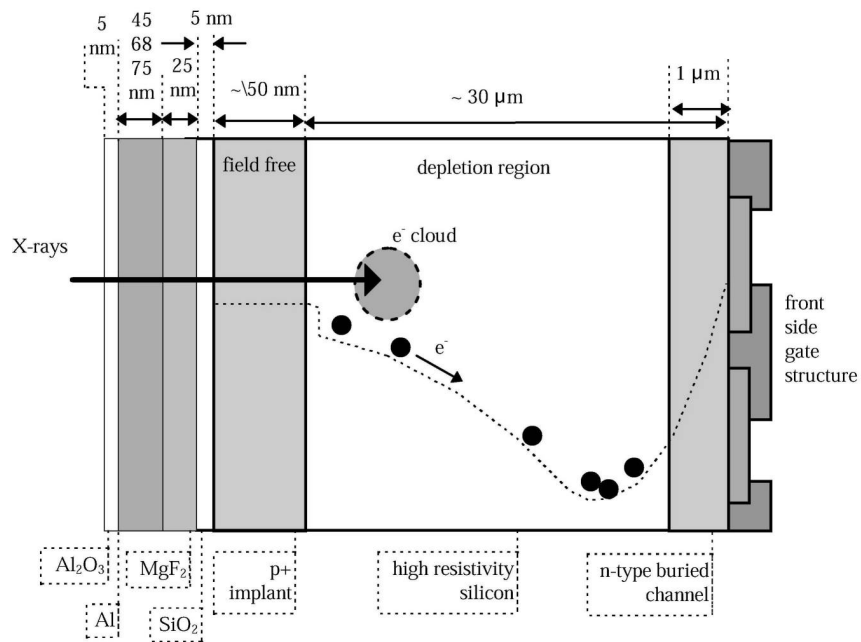
Figure 4.11: Cross section of the back-illuminated CCD chip from Ref. 11 All the different layers on top of the CCD chip are indicated as well as their thickness.
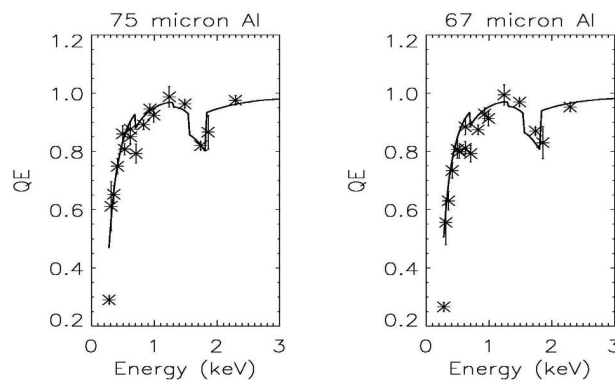
Figure 4.12: Calculated (solid line) and measured (crosses) detection efficiency (QE) for two typical values for the Al layer thickness on the CCD chip from Ref. 10.

When a photon is absorbed, the energy is transferred into electron-hole pairs, each pair requiring 3.65 eV. The electrons are caught in the potential well of the pixel. The CCD is depleted to the extent that the field just reaches the backside. A depletion that is too strong makes the CCD sensitive to defects at the back surface. In an insufficiently depleted device the photo-induced charge will not be confined to one or two pixels, but will diffuse over a

larger region. This would result in a reduced resolution. The back-layer is passivated by p+ implant to reduce leakage of electrons to this surface. To achieve a high and uniform quantum efficiency at the low photon energies the thickness of this layer has to be 50 nm. To suppress the sensitivity to visible light, the device has been coated with a thin layer of Al. To isolate this layer electrically from the CCD a MgF_2 insulating layer of 25 nm is applied. In addition, there are the native oxide layers for Si and for Al. In Fig. 4.12 the calculated and measured quantum efficiency of the CCD for two different thickness of the Al layer is given. Various bias levels can be adjusted to optimize the CCD response. In case of this CCD camera the response is optimized for photon energies as low as 280 eV (the carbon K-edge). Figure 4.13 gives a picture of the CCD chip mounted in a box of electronics boards with all the readout and communications electronics. In the goniometer setup an Al/C-filter (Luxel Inc.[2]), with layer thicknesses of, respectively, 150 nm and 27 nm, is mounted in front of the CCD chip (see Fig. 4.8). This filter blocks visible light (transmission = 5×10^{-8}) stronger than the deposited 67-nm Al-layer on the CCD chip, which appeared to be too thin to reduce it completely, and has an transmission in the water-window between 25% and 65%.
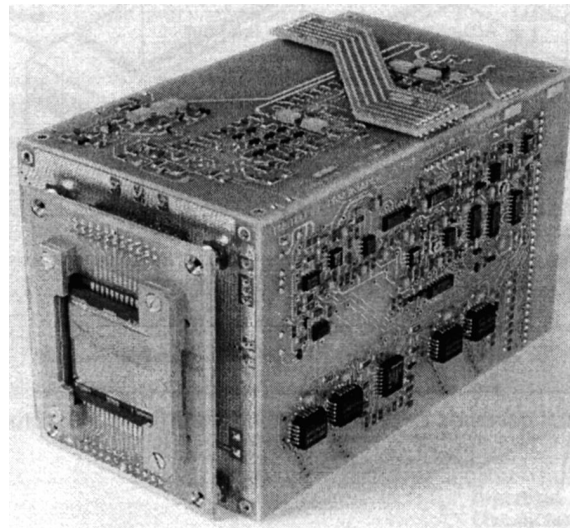

Figure 4.13: The CCD chip (28.0×25.4 mm^2) mounted in the front of a hollow box of electronic boards with readout and communication electronics.

At room temperature the CCD response is dominated by thermal noise. Therefore, the CCD chip is cooled down to -80°C by pressing the CCD chip with its front side on the surface of a cold copper block. The cooling is divided into three stages. The bottom plate on which the electronic box is mounted is cooled by cooling water with a temperature of +5°C. Then, with a stack of Peltier elements a copper block, which is situated inside the electronic box, is cooled to −35°C. With another Peltier stack a second copper block, against which the CCD chip is pressed, is cooled to −80°C. The complete CCD camera is placed inside a vacuum chamber, with a typical pressure of 10^{-6} mbar. To prevent contamination of the cold CCD surface by water and other residual gas components, a liquid nitrogen cold trap is connected to the vacuum chamber. A metal protection box surrounding the electronic box has an opening of 25.0×20.0 mm^2 in front of the CCD chip. A metal shutter made from a thin

aluminum strip covers this opening. It is opened during illumination of the CCD chip and closed during readout. The shutter is not thick enough to block hard x-ray radiation.
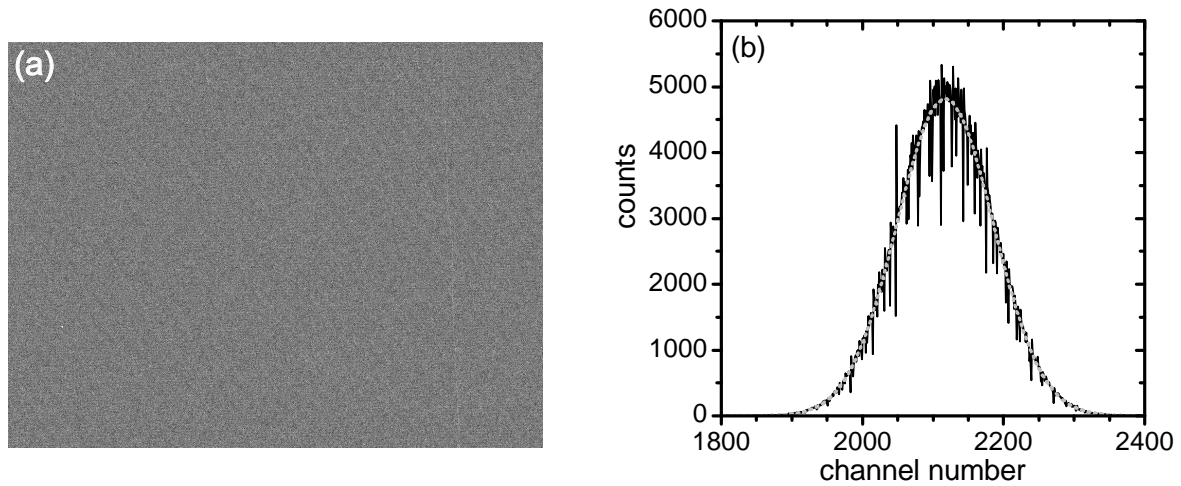
Figure 4.14: (a) CCD frame image of a typical system peak measurement (b) Pulse height spectrum, which is a histogram of pixel values from the CCD image. By fitting a Gaussian profile (the dotted curve) the peak position $p = 2108$ and the standard deviation $\sigma = 68.7$ are determined.
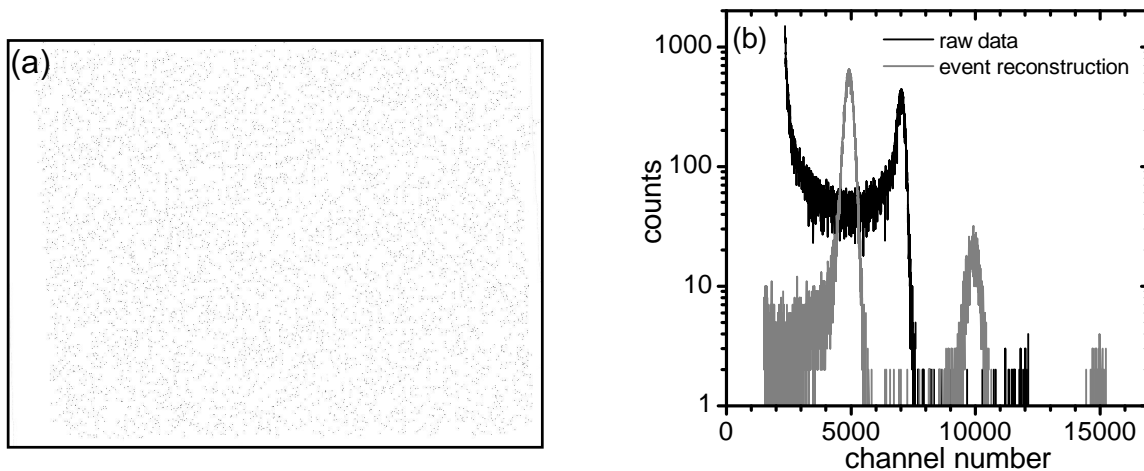
Figure 4.15: (a) CCD image (inverted) of photon measurement illuminated by Al characteristic x-rays. (b) Corresponding pulse height spectrum before (black curve) and after event reconstruction (gray curve) respectively. After event reconstruction besides the Al-K peak at channel 5000, also the double and triple photon peaks are seen.

After the CCD chip is illuminated the readout procedure is started. The pixels are sequentially shifted to the readout amplifiers and digitalized by a 16-bits ADC. This readout procedure adds systematic noise, which appears as a positive offset in the photon energy value. About half of all events are so-called single pixel events, for which the entire charge is collected underneath one pixel, and the other half of all events are called split event. On average, a soft x-ray photon will occupy about 2.5 pixels.

Figure 4.16: (a) A 100×100 window of the CCD image from Fig. 4.15(a). (b) The same window after event reconstruction, in which all split events are calculated back to the original photon.

The control software of the camera has two sampling modes, a system-peak measurement and a photon measurement. A system peak is a measurement without illumination of the CCD chip of which an example is shown in Fig. 4.14(a). The data file contains all the 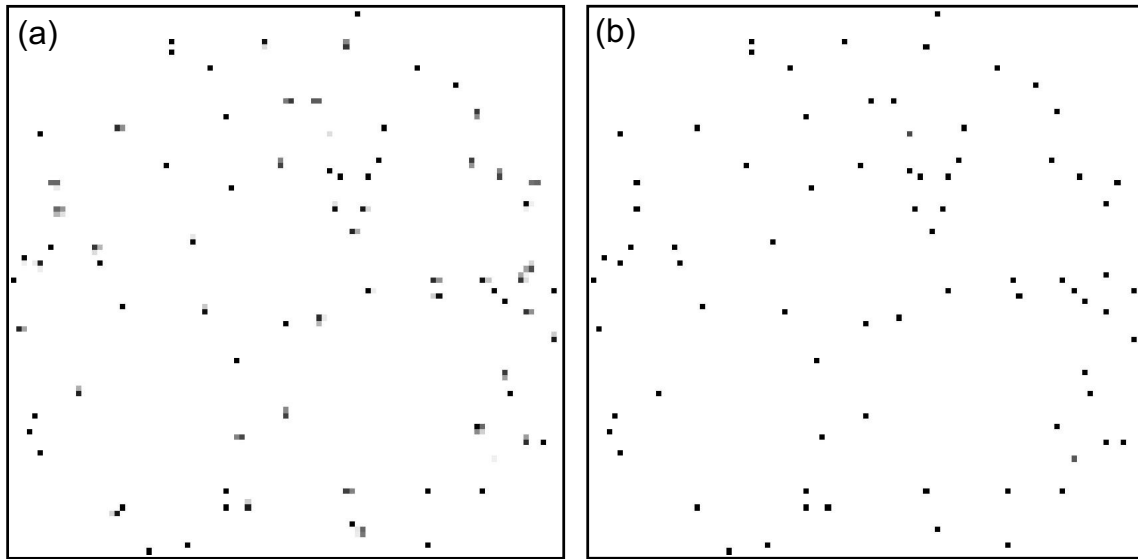pixels from the measurement irrespective of its value. From this system peak measurement a pulse height spectrum (PHS) is extracted, which is a histogram of counts (number of pixels) versus channel number (measure for the collected charge per pixel) of which an example is shown in Fig. 4.14(b). The system peak characterizes electronic noise of the amplifiers. Because the noise is stochastic the system peak has a Gaussian shape, which is characterized by its position (p) and standard deviation (σ). These two parameters are influenced by the temperature of the CCD chip and the values of bias voltages. Because the photon energy is determined with respect to the position of the system peak, the system peak measurement has to be repeated frequently. The minimum resolvable photon energy is determined by the width of the system peak.

A photon measurement is a measurement with x-ray illumination of the CCD chip. In this case a lower threshold has to be specified, which is generally set to the right edge of the system peak at $p + 3\sigma$. All pixels with values of the collected charge lower than this threshold, are rejected. This reduces the size of the data file enormously and allows a large number of frames per measurement. Figure 4.15(a) shows an example of a CCD image obtained by the illumination with characteristic x-rays from an Al-target. Figure 4.15(b) shows the corresponding pulse height spectrum (black curve). The Al-K_α peak is positioned at about channel 7000. On the low photon-energy side a long tail is visible which is, in this particular measurement, mainly due to split events.

In Fig. 4.16(a), which is a 100×100 window of the CCD image in Fig. 4.15(a), isolated islands of occupied pixels are seen. Some patterns are recognized as split events and calculated back to the original photon, which is called event reconstruction. An algorithm for this event reconstruction searches 2×2 patterns in the CCD image. It is then assumed that these pixels originate from one incident photon with the sum of the pixel charges representing

the original energy value. Larger patterns of pixels are rejected, because then it is unclear how many incident photons have caused these patterns. Therefore, when using the CCD camera as a photon-counting device to generate a spectrum of the incident radiation, the occupation of the chip should not exceed 10%. With higher occupation numbers the chance that two photons hit the same or neighouring pixels becomes too large. In Fig. 4.16(b) the 100×100 window after event reconstruction is shown containing only single pixel events. The full PHS after event reconstruction (see the gray curve in Fig. 4.15b) shows a clear Al-K peak, which has hardly any tail and which is slightly higher than in the raw data. The position of the peak is shifted to the left, because the system peak position is subtracted from the pixel value. Due to reconstruction the double peak and triple peak have become more intense.

Table 4.2: The fluorescence lines used for the calibration in the goniometer setup.

Element	Z	$K_{\alpha1}$ [eV]	Intensity	$K_{\alpha2}$ [keV]	Intensity	K_β [keV]	Intensity
Al	13	1486.7	1.00	1486.27	0.50	1557.45	0.01
Si	14	1739.98	1.00	1739.38	0.50	1835.94	0.02
Ti	22	4510.8	1.00	4504.9	0.50	4931.8	0.15
V	23	4952.2	1.00	4944.6	0.50	5427.3	0.15
Ni	28	7478.15	1.00	7460.89	0.51	8264.66	0.17
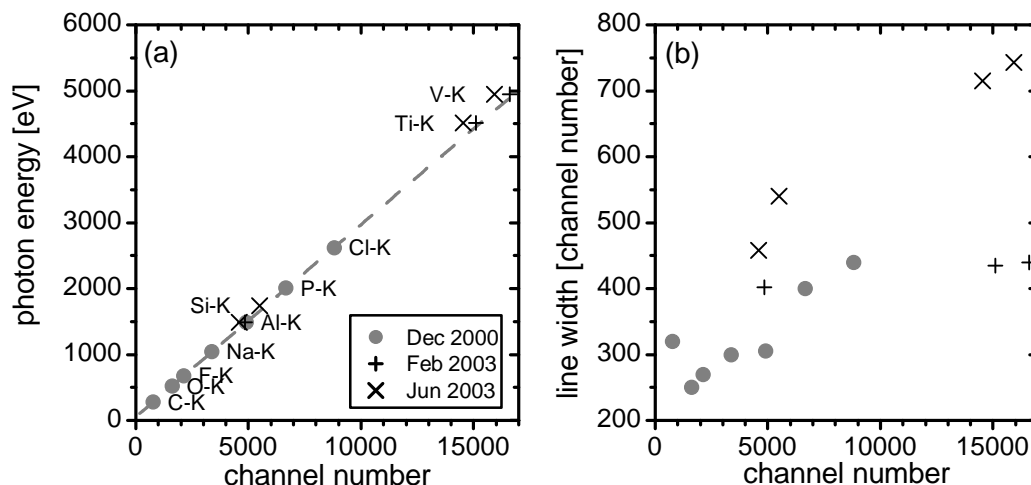
Figure 4.17: (a) Several calibrations of the CCD camera. The dashed curve represents the linear fit of the calibration made in December 2000 at SRON. (b) The FWHM width of the calibration lines expressed in number of channels.

4.2.3.2 Calibration and resolution

Calibration of the CCD camera is done with x-ray fluorescence lines. At SRON the camera was calibrated by using photon-induced fluorescence x-rays from C, O, F, Na, Al, P and Cl. These sources have a very low intensity, but produce a very clean spectrum with hardly any

Bremsstrahlung background. In Fig. 4.17(a) this calibration is plotted (gray circles) and in Fig. 4.17(b) the FWHM-width of each line is plotted.

Figure 4.18: (a) K_α-fluorescence line from aluminum, summed over a few measurements (b) K_α and K_β-fluorescence line from vanadium, summed over few measurements. The dotted curve in both figures show the fit of a Gaussian line profile.

The calibration of the CCD camera has to be checked frequently. Fluorescence radiation is generated together with the Cherenkov radiation in the target foil by the relativistic electron beam. During the passage through the targe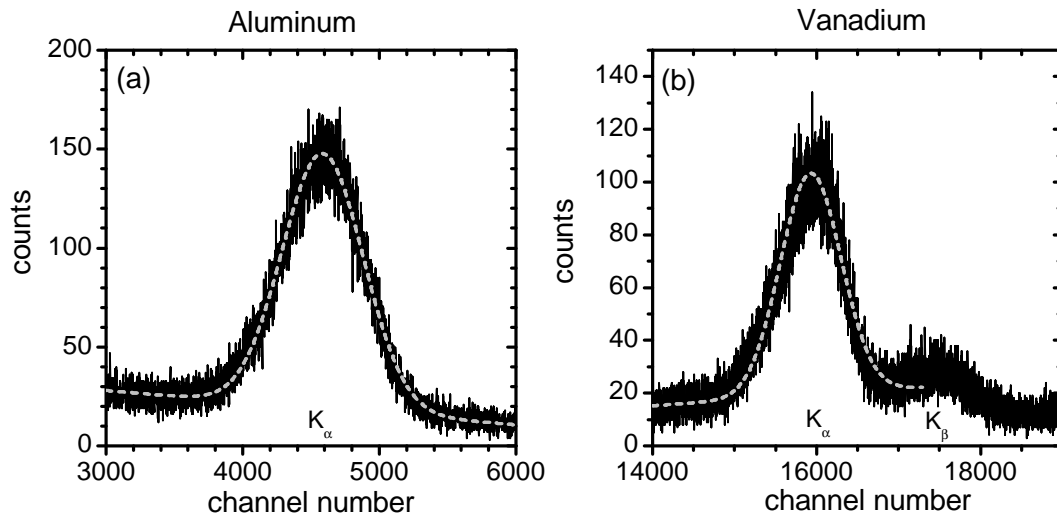t foil, a relativistic electron can excite an inner-shell electron that leaves a vacancy behind. When this vacancy is occupied by an electron from a higher shell, a characteristic photon is emitted. K_α-lines (electron decays from the L-shell to the K-shell) and K_β-lines (from the M-shell to the K-shell) are the most intense fluorescence lines, but the intensity decreases for lower atomic numbers. In Table 4.2 the fluorescence lines are summarized that have been used for the calibration of the CCD camera during Cherenkov radiation measurements. Fluorescence lines as in low photon-energy as in the SRON calibration cannot be measured in the goniometer setup, because the intensity is too low compared to the Bremsstrahlung background. However, the SRON calibration is linear throughout the whole energy range. Figure 4.18 shows two examples of fluorescence lines observed in the goniometer setup. A clear spectrum was obtained at goniometer angles between 8° and 10°, because the Bremsstrahlung background is low at these angles. The resolution of the CCD camera is too low to resolve the titanium and vanadium $K_{\alpha1}$ and $K_{\alpha2}$ lines [see Fig. 4.18(b)]. These peaks are fit by a Gaussian profile with a linear offset to take the background into account as is indicated by the dotted curves. The two calibrations made during operation of the CCD camera in the goniometer setup are added in Fig. 4.17(a) and the corresponding calibration parameters are given in Table 4.3.

References

1 P.M. Lapostolle and A.L. Septier, *Linear Accelerators*, North-Holland Publishing Company, Amsterdam, 1970.

2 Luxel Inc., http://www.luxel.com.

3 D. Attwood, *Soft X-Rays And Extreme Ultraviolet Radiation: Principles And Applications*, Cambridge University Press, Cambridge, 2000.

4 CXRO-website, http://www-cxro.lbl.gov.

5 Osmic Inc., http://www.osmic.com

6 International Radiation Detectors Inc., http://www.ird-inc.com

7 R. Moonen, *Generatie van Silicum-L EUV Cherenkov-staling met 5 MeV elektronen*, Internal Traineeship Report FTV-TIB 2000-07, Eindhoven, 2000.

8 R. de Leeuw, *The Accelerator Injection Chain of the Electron Storage Ring EUTERPE*, Universiteitsdrukkerij TUE, Eindhoven, 1996.

9 J. Corstens, *Summary Scattering Theory*, Internal Report, Eindhoven, 2001.

10 J.W. den Herder, *et al.*, "The reflection grating spectrometer on board XMM-Newton", *Astron. Astrophys.* **365**, L7-L17, 2001.

11 J.W. den Herder, *RGS User Manual*, Document ID: RGS-SRON-PM-98-010, Published at: http://rhea.sron.nl/divisions/hea/xmm/manual.html, 1999.

5 Soft x-ray Cherenkov radiation: Experimental results

This chapter discusses the experimental results obtained on soft x-ray Cherenkov radiation. The main objective of the experiments is to prove that moderately relativistic electrons generate Cherenkov radiation in the soft x-ray spectral region. The success of the measurements depends strongly on the reduction of the background intensity and the separating the soft x-ray Cherenkov signal from the remaining background signal. In Chapter 4 these background components are presented together with the spectral sensitivity of the detection systems. In this chapter the measurements of the soft x-ray Cherenkov from different materials are described in detail with attention to the background correction or separation method.

Section 5.1 presents the observation of Si-L (99.7 eV) Cherenkov radiation produced by 5-MeV electrons in a silicon foil. The radiation has been analyzed by the spectrometer consisting of a multilayer mirror and photodiode. Section 5.2 presents the first observation of Cherenkov radiation in the water-window spectral region generated at the Ti-L (453 eV) and V-L (512 eV) edges. The radiation has been analyzed by a soft x-ray CCD camera.

Section 5.3 discusses some attempts to measure Cherenkov radiation from carbon and nickel samples, and from the chemical compound silicon nitride. Carbon has been selected to test if 10-MeV electrons are already sufficient to produce C-K (284 eV) Cherenkov radiation, which has been observed before[1,2] with 75-MeV and 1.2-GeV electrons. Surprisingly, our samples did not generate Cherenkov radiation, although the optical data suggest that the refractive index at the K-edge exceeds unity sufficiently for 10-MeV electrons. Nickel has been selected to test if higher Cherenkov photon-energies than the water window can be generated with 10-MeV electrons. Theory predicts that Ni-L (852 eV) Cherenkov radiation is generated, however we were unable to detect this radiation experimentally. Finally, a silicon nitride (Si_3N_4) sample was tested as an example for generating soft x-ray Cherenkov radiation in chemical compounds. However, no N-K (410 eV) Cherenkov radiation was observed.

5.1   Si-L Cherenkov radiation

Soft x-ray Cherenkov radiation from a silicon foil can be generated at the L-edge (99.7 eV), where the refractive index slightly exceeds unity [see Fig. 5.1(a)]. The properties of Si-L Cherenkov radiation have been presented as examples in the theoretical discussion of Sec. 2.2. Before our experiments only Moran *et al.*[1] have observed Si-L Cherenkov radiation produced by 75-MeV electrons passing through the foil at grazing-incidence angle. We show that 5-MeV electrons are already sufficient to generate Si-L Cherenkov radiation with a reasonable yield. Using the multilayer-mirror-based spectrometer setup, described in Sec. 4.1, the spectral angular distribution and the absolute yield is measured. The first results on Si-L Cherenkov radiation generated by 5-MeV electrons have been reported by Knulst *et al.*[3] Improved Si-L Cherenkov measurements by Brummans[4] are presented in detail in Sec. 5.1.1.
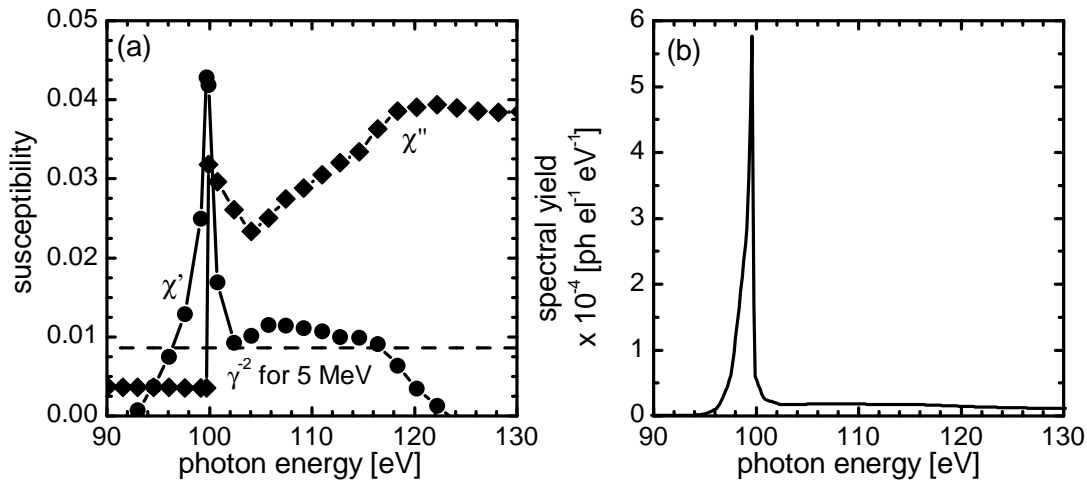

Figure 5.1: (a) Real part (χ', circles) and imaginary part (χ'', diamonds) of the susceptibility of silicon as a function of photon energy around the L-edge. The Cherenkov threshold for 5-MeV electrons is indicated by the dashed line. (b) Theoretical Cherenkov spectral yield for 5-MeV electrons in a 10-μm silicon foil.

During these measurements of Si-L Cherenkov radiation the electron beam passes through the foil at normal incidence. In that case the Cherenkov intensity is limited by the absorption length, as is discussed in Sec. 2.2. Grazing incidence might enhance the Cherenkov intensity as was discussed theoretically in Sec. 2.3. Therefore, we tested a silicon microchannel plate (MCP) with the channel walls oriented at grazing angle to the beam. The measurements are presented in Sec. 5.1.2.

5.1.1   Si-L measurements at normal incidence

In the experiments a 10-μm thick undoped single-crystal silicon wafer (Virginia Semiconductors Inc.[5]) of 1-inch (25.4 mm) diameter has been used. This wafer was gently pressed between two aluminum rings with a 20.0-mm free diameter for the electron beam to pass through. In Fig. 5.1(a) the threshold value for 5-MeV electrons is indicated in the plot of

the silicon susceptibility. The calculated angle of maximum Cherenkov intensity [see Eq. (2.56)] for this electron energy is $\theta = 10.6°$. In Fig. 5.1(b) the theoretical spectral Cherenkov yield is plotted, which is calculated by the Frank-Tamm equation (2.59) for an absorbing medium. Integration of the spectral yield over the Cherenkov line results in a theoretical yield of $N = 8 \times 10^{-4}$ photon/electron.

The principle of the spectrometer detection system, which is explained in Sec. 4.1, is rather straightforward. The observation angle of the detection section is fixed at either $\Theta = 2°$, $5°$ or $10°$ (see Fig. 4.2). The detector subtends an angle of $\Delta\Theta = 0.93°$. In Fig. 5.2(a) the theoretical spectral Cherenkov yield integrated over the detector solid angle is plotted for the observation angles of $\Theta = 5°$ and $\Theta = 10°$. The photon energy and intensity increases with increasing emission angle, which is typical for Cherenkov radiation. In short, the measurement procedure at each detector position Θ involves a multilayer-mirror scan to measure the spectral intensity distribution of the radiation. In Fig. 5.2(b) the spectral reflectivity of the multilayer mirror is plotted as a function of angle of incidence, to show that the resolution is just sufficient to see the spectral difference between the two detector angles Θ.
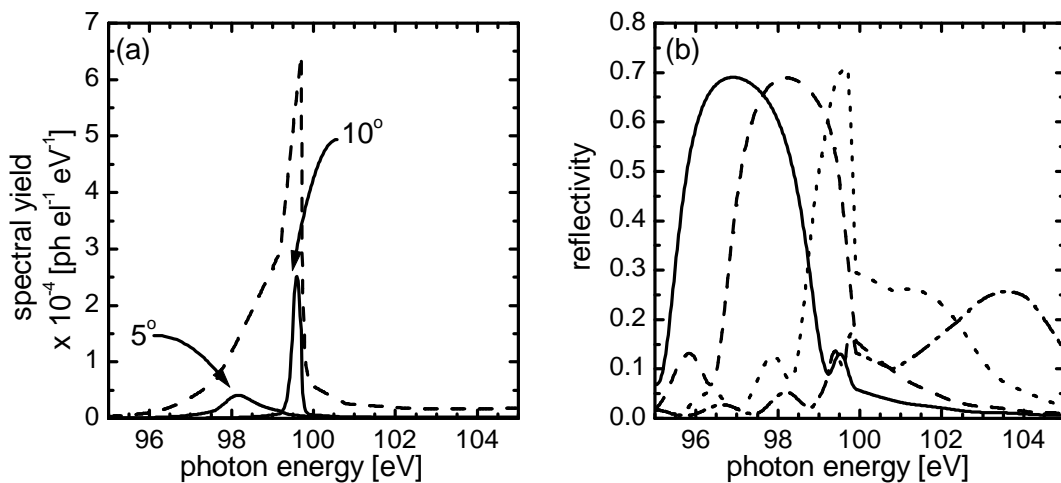
Figure 5.2: (a) Theoretical spectral yield emitted within the angular ranges 0°-15° (dashed line), $\Theta = 5°$ with $\Delta\Theta = 1°$ (solid line), and $\Theta = 10°$ with $\Delta\Theta = 1°$ (solid line). (b) Reflectivity of the Mo/Si-multilayer mirror as a function of photon energy for various angles of incidence: $\theta = 1.5°$ (solid), $\theta = 10°$ (dashed), $\theta = 16°$ (dotted), and $\theta = 20°$ (dot-dashed).

One of the main complicating factors is the large background signal, which is typically an order of magnitude larger than the Cherenkov signal. The actual analysis of the raw signal from the silicon photodiode and extracting the soft x-ray Cherenkov spectrum involves a few steps and requires some understanding of the various sources that contribute to the photodiode signal.

During this project two complete series of measurements of Si-L Cherenkov radiation have been made, with different methods of correcting for the background contributions. In Fig. 5.3 the results of the first series[3,6], are plotted for the detector angles $\Theta = 5°$ and 10°. The

shapes of the measured spectral angular distributions of Si-L Cherenkov radiation (squares) agree with theory (dashed curve). The maximum of the 10° detector-signal curve occurs at a larger angle of incidence than the maximum of the 5° detector-signal curve. This implies that higher photon energies are emitted into $\Theta = 10°$ than into $\Theta = 5°$, which is in agreement with the theoretical expectations of Cherenkov radiation. The absolute yield is of the expected order of magnitude. However, there is still a discrepancy: the scaling factor between theory and measurement for $\Theta = 5°$ and $\Theta = 10°$ are different.
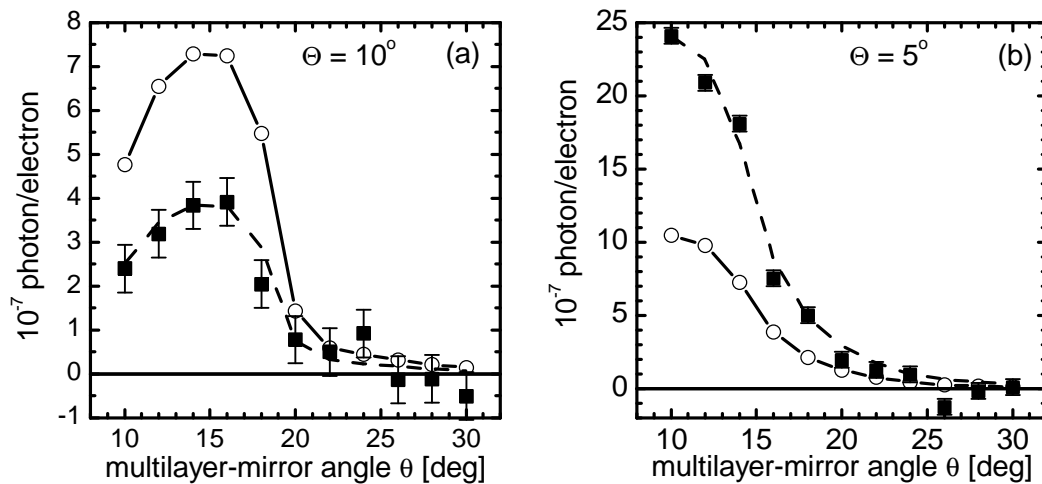

Figure 5.3: Measured (squares) and calculated (circles) detected yield as a function of angle of incidence on the multilayer mirror at a detector angle of $\Theta = 5°$ (a) and $\Theta = 10°$ (b). The dashed curve is the theoretical (solid line) multiplied by a factor of 2.4 at $\Theta = 5°$ and 0.6 at $\Theta = 10°$.

In the remainder of this section the second series[4] is presented in detail. The detection setup has been improved by, for instance, automating the multilayer-mirror rotation, which had to be set manually during the first series. These changes enabled a more sophisticated and accurate background correction. As a result the inconsistency in the scaling factor of the first series was removed and the theoretical total yield of 8×10^{-4} photon/electron has been confirmed by the measurements.

First, the background-correction method is discussed. In Fig. 5.4(a) the photodiode signal is plotted as function of the photodiode angle 2θ with the multilayer mirror kept at a fixed angle $\theta = 40°$, so that no radiation is reflected onto the photodiode. In this case the photodiode signal is only due to the background, which consists of hard x-ray radiation penetrating through the vacuum walls and also through the photodiode. At small angles the photodiode is close to the entrance diaphragm (see Fig. 4.3). At this position the shielding is minimal, resulting in a large signal. In Fig. 5.4(b) the photodiode signal is plotted as function of multilayer mirror angle θ with the photodiode angle fixed at $2\theta = 60°$. To exclude the detection of reflected radiation the photodiode was covered with an 11-µm aluminum foil. In this case the background signal varies much less than in Fig. 5.4(a) and the signal shows a weak linear behavior as a function of multilayer-mirror angle θ. We thus conclude that the

background signal depends strongly on the position of the photodiode within the spectrometer chamber and is only slightly influenced by the multilayer-mirror angle.
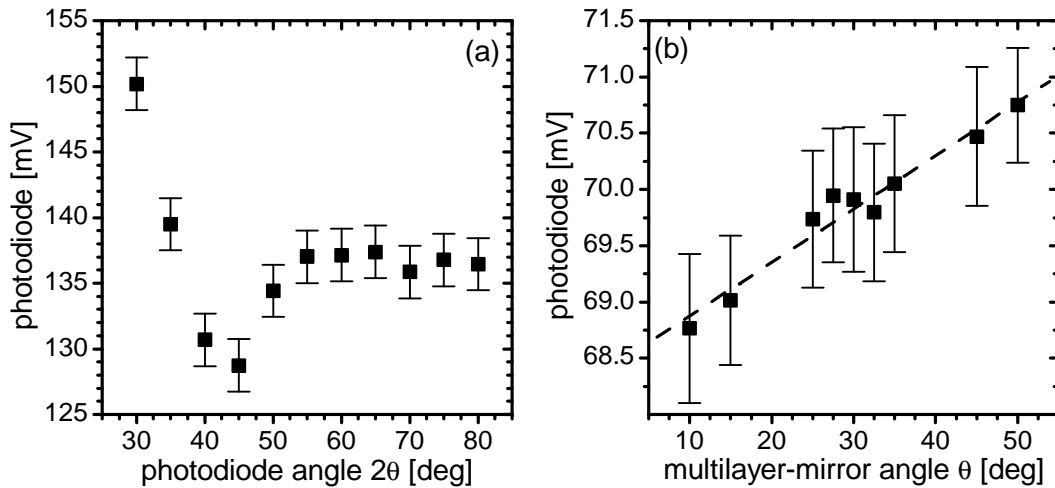
Figure 5.4: (a) Ti/Zr/C-photodiode signal as function of diode angle 2θ with the Mo/B$_4$C-multilayer mirror angle fixed at $\theta = 40°$ for $\Theta = 5°$. (b) Ti/Zr/C-photodiode signal as function of Mo/B$_4$C-multilayer mirror angle θ with the diode angle fixed at $2\theta = 60°$ and covered with an 11-μm aluminum foil for $\Theta = 5°$.
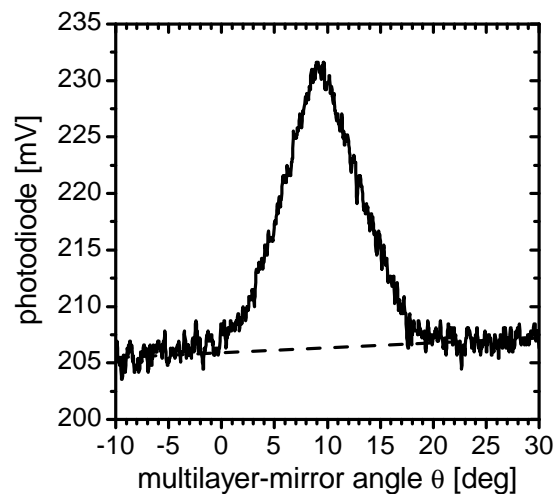
Figure 5.5: A typical photodiode measurement as function of the multilayer-mirror angle θ, i.e. the rocking curve, with the diode angle fixed at $2\theta = 20°$ for $\Theta = 5°$. The dashed line indicates the fitted background signal.

The linear dependence on the multilayer-mirror angle allows an accurate correction of the background. Based on this observation the following measurement procedure has been implemented: for a fixed photodiode angle 2θ, the signal is recorded as a function of multilayer-mirror angle θ, which is rotated by a stepper motor. Such a measurement for the case of x-rays reflected by a Bragg crystal is usually called a rocking curve. In Fig. 5.5 a

typical rocking curve is shown with photodiode angle $2\theta = 20°$. In such a rocking curve for the case of the multilayer-mirror spectrometer, the contribution of the reflected radiation to the photodiode signal appears as a peak on the linear background. The dashed line is the linear fit of the background determined by the wings of the measured curve. Two parameters are extracted from this measurement, i.e. the peak height of the reflected radiation with respect to the linear fit of the background signal and the corresponding multilayer-mirror angle θ at which the signal peaks. Note that the reflected radiation contains mainly soft x-ray radiation, but can contain also visible radiation, which is also reflected by the multilayer mirror.

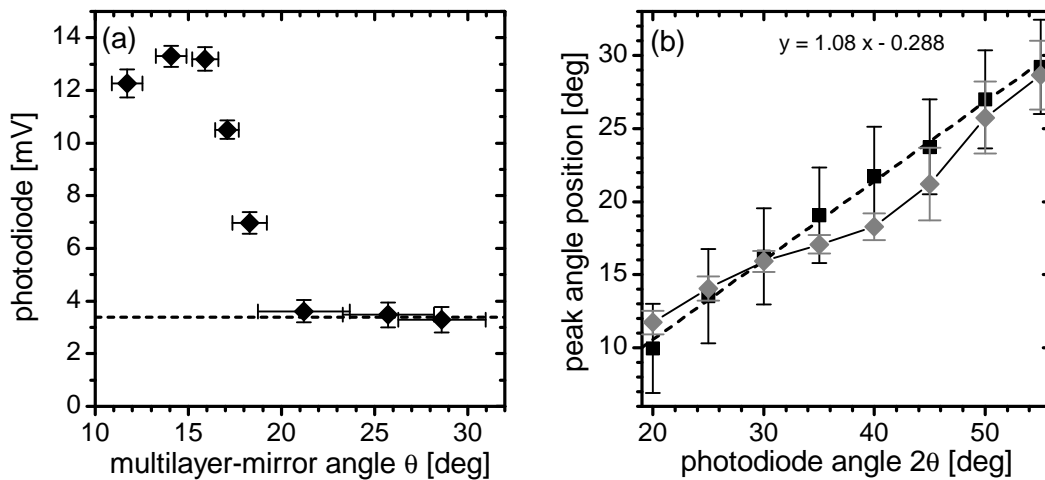Figure 5.6: (a) The background corrected photodiode signal as function of Mo/Si-multilayer mirror angle θ for $\Theta = 10°$. The dashed line indicates the offset due to the visible light. (b) The measured peak position (diamonds) plotted versus photodiode angle 2θ. The cross-check (squares) without accelerator operation. The dashed line is the fit of the control measurement.

Rocking curves are made for a certain number of photodiode angles 2θ, each corresponding to a multilayer-mirror angle of incidence θ. In Fig. 5.6(a) the obtained peak heights from these measurements are plotted as a function of multilayer-mirror angle of incidence at $\Theta = 10°$. The measurement points are plotted at the angle corresponding to the peak of the rocking curve. In Fig. 5.6(b) these peak angular positions (diamonds) are plotted as a function of the fixed photodiode angle 2θ, which apparently does not follow the θ-2θ relation (dashed line) exactly. This deviation is analyzed below.

To exclude mechanical misalignment, a cross-check was performed using visible light from the accelerator. In the standby-mode of the accelerator the gun-filament is continuously heated by the gun current and emits visible light. A fraction of this light is reflected in the direction of the detector and is detected by the photodiode, which is, in spite of its integrated filter, still slightly sensitive to visible light. Performing a measurement series with the glowing gun filament, but no accelerated electrons, the square points in Fig. 5.6(b) are obtained, which follow exactly the θ-2θ relation (dashed curve). This excludes a misalignment or mechanical problem. Therefore, the deviation from the θ-2θ relation should be found by taking a close look at the rocking curves. In Fig. 5.7 two background corrected

rocking curves (black curves), i.e. at $2\theta = 20°$ (a) and at $2\theta = 40°$ (b), are plotted together with the corresponding cross-check representing only the visible light from the gun filament (gray curves). In case of $2\theta = 40°$ the shift of the peak position to the left is clearly visible. This is simply explained by the fact that in this case at smaller multilayer-mirror angles than at exactly θ-2θ, there is already overlap between the beam of the reflected radiation and the photodiode surface. These smaller multilayer-mirror angles correspond to lower photon-energy. Since the Si-L Cherenkov intensity is maximal at these smaller angles, the peak position is shifted to lower angles. The value of the shift depends on the photodiode position 2θ with respect to the optimum reflection of the Si-L Cherenkov radiation by the multilayer mirror. This is the cause for the deviation in Fig. 5.6(b).
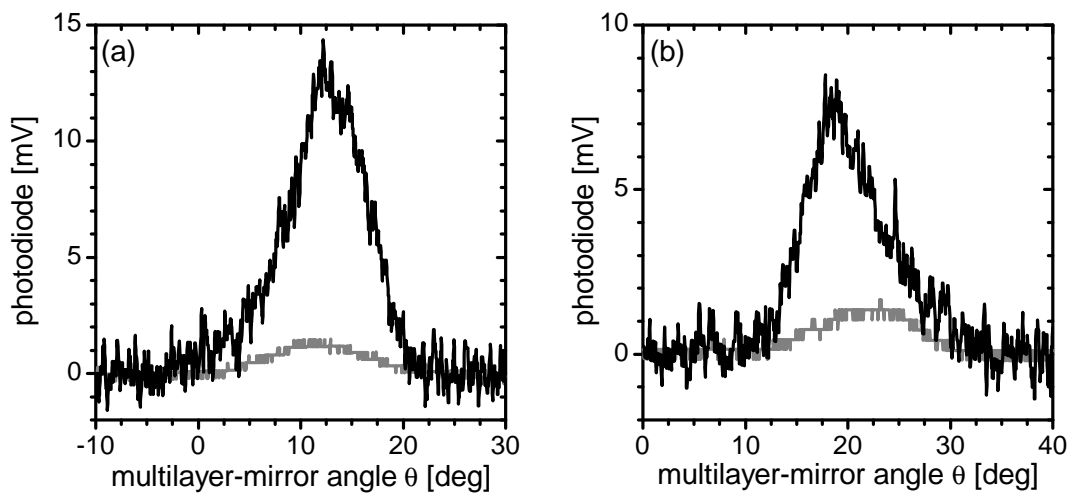

Figure 5.7: Background corrected photodiode signal (black curves) at $2\theta = 20°$ (a) and $2\theta = 40°$ (b), are plotted with the corresponding cross-check using visible light (gray curves).

So far, we have only corrected for the hard x-ray background. Visible radiation, which is partly coming from the gun filament and is partly generated as transition radiation at the target foil, is still included in the measurement of Fig. 5.6(a), because this light is reflected by the multilayer mirror simultaneously with soft x-ray radiation. The reflectivity of the visible light is independent of multilayer-mirror angle and therefore appears as a constant offset in Fig 5.6(a), of which the value is determined by the last three data points and indicated by the dashed curve. By subtracting this offset, the pure soft x-ray signal is finally obtained.

Using the same procedure, Si-L Cherenkov measurements as a function of multilayer-mirror angle have also been performed at $\Theta = 2°$ and $\Theta = 5°$. Figure 5.8 shows the soft x-ray signals obtained as a function of multilayer-mirror angle. The maximum of the 10° detector-signal curve occurs at a larger angle of incidence than the maximum of the 5° detector-signal curve. This implies that higher photon energies are emitted into $\Theta = 10°$ than into $\Theta = 5°$, which is in agreement with the theoretical expectations of Cherenkov radiation.

To enable an accurate comparison of experimental data and theory, we have calculated the detector signal as a function of multilayer-mirror angle θ. For this theoretical calculation, all the parameters of the measurement have to be taken into account, i.e. the theoretical

spectral yield emitted within the detector solid angle [Fig. 5.2(a)], the accelerator current (typically 8.2 μA average current), the detector solid angle (1.0 cm^2 photodiode area at 62 cm), the reflectivity curves of the Si/Mo-multilayer mirror [Fig. 5.2(b)] and the quantum efficiency of the photodiode with an integrated Ti/Zr/C-filter [Fig. 4.6]. The shape of the measured signals agree with the calculated curves. The measured signals for $\Theta = 5°$ and $\Theta = 10°$ are about twice as low as the calculated signals (dashed curves). For $\Theta = 2°$ the amplitude of the measured signal is higher than the calculated signal. The latter is probably due to the fact that electron scattering is not taken into account in the calculation. This effect causes in general a broadening effect on the angular profile. Because in this case the average scattering angle is estimated to be small compared to the emission angle of the Si-L Cherenkov radiation, especially the intensity at small angles is strongly increased. At larger emission angles the intensity is decreased a little. This broadening effect has been taken into account in the calculations for the water-window measurements of titanium and vanadium (see Sec. 5.2).

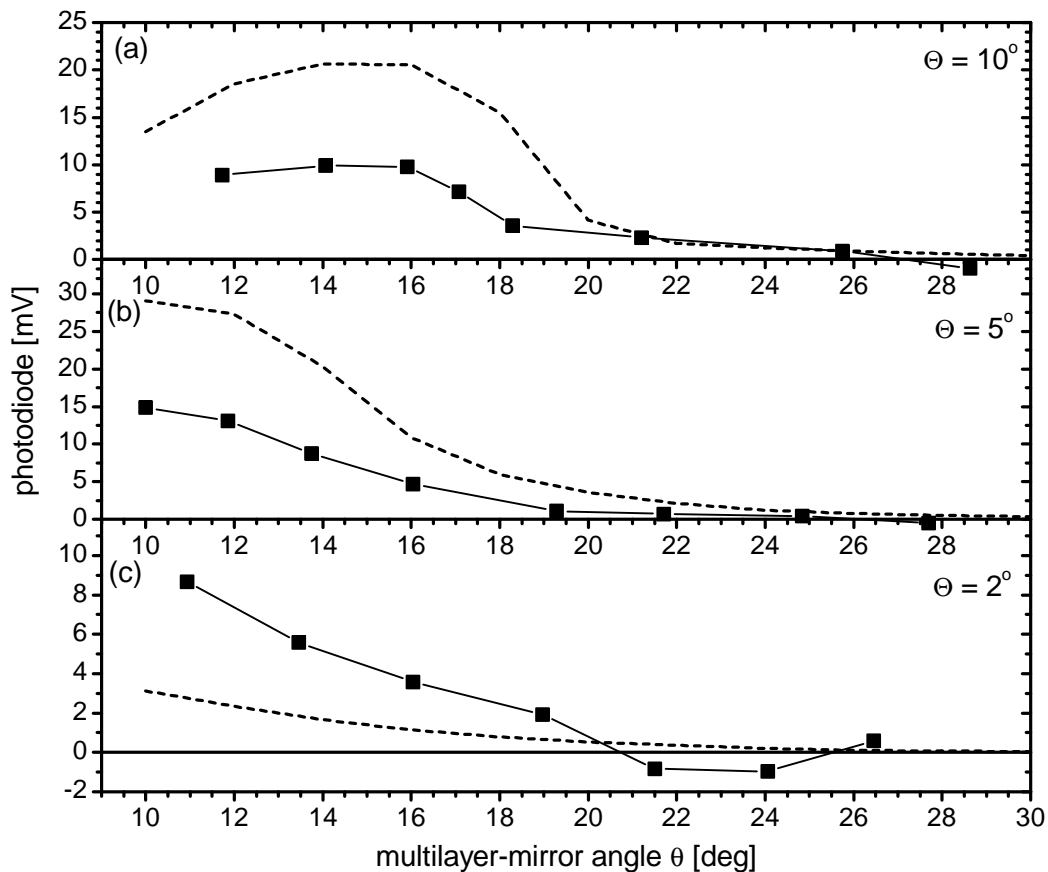Figure 5.8: The Si-L Cherenkov experimental data (squares) and theoretical curves (dashed) obtained at $\Theta =10°$ (a), $\Theta = 5°$ (b), and $\Theta = 2°$ (c) and plotted as a function of multilayer-mirror angle θ.

These measurements constitute the first spectrally and angularly resolved observation of Si-L Cherenkov radiation. Our measurements show that on the basis of the silicon refractive

index data of Henke database[7], the measured Cherenkov radiation can be accurately predicted. Although the measured signal is twice as low as the calculated signal, which can be attributed to the combination of electron scattering and remaining systematic errors, the estimated experimental yield differs less than 50% from the theoretical value of 8×10^{-4} photon/electron. In addition, we have demonstrated that soft x-ray Cherenkov radiation can be generated with moderate electron energies. The resulting soft x-ray brightness and implications for source development are discussed in Chapter 6.
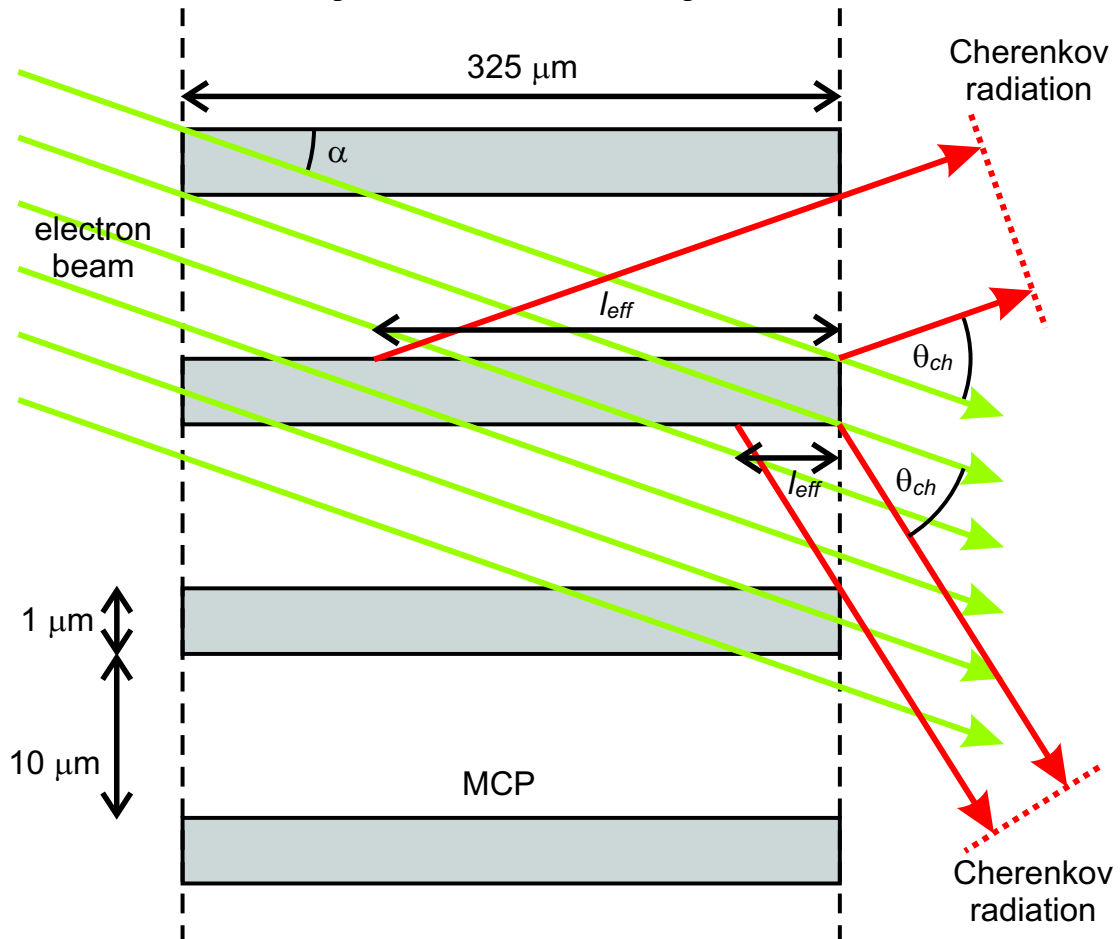
Figure 5.9: Sketch of an electron beam passing through a microchannel plate structure and generating Cherenkov radiation inside the channel walls.

5.1.2   Si-L measurements at grazing incidence

The theory of grazing-incidence Cherenkov radiation has been discussed in Sec. 2.3. The conclusion was drawn that for electron energies up to 10 MeV the intensity may be enhanced a few times compared to normal incidence. In this section the experimental results of a grazing-incidence electron-beam on silicon are presented. Instead of a single silicon foil, we have purchased a silicon microchannel plate, because it has an interesting geometry. The wall of a channel can act as a small foil, placed at grazing angles with respect to the electron beam. First, the geometry of the microchannel plate and the dependence on tilt angle is analyzed.

Then, the measurements are presented in which the Cherenkov intensity is measured as a function of the tilt angle of the microchannel plate.

Figure 5.10: Electron microscope image of silicon microchannel plate from Ref. 8. (a) top view (b) cross section.

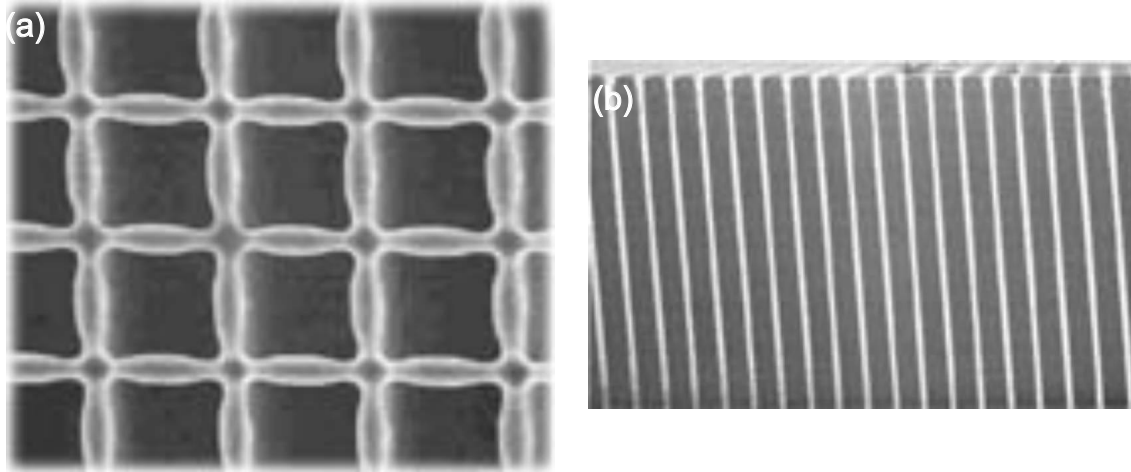In Fig. 5.9 a sketch is shown of an electron beam passing through a microchannel plate at grazing angles of incidence. The channel walls are almost parallel to the electron beam. The Cherenkov radiation is generated inside or near the walls of the microchannel plate and the intensity should be enhanced with respect to normal incidence (see Sec. 2.3). The channels of the microchannel plate are very narrow (typically about 10 μm), but very long (hundreds of μm). Because the Cherenkov emission angle is small, the radiation generated deep in the channel is still able to escape the channel. For example, radiation emitted under an angle of 5° with respect to the orientation of the channels, can escape from a depth of about 11 times the width of the channel. On the other hand, if the electron beam would be passing through the microchannel plate parallel to the channel walls, only a fraction of the electrons would pass through material, i.e. the wall cross-section divided by the channel area. Therefore, the microchannel plate has to be tilted by a small angle (α) with respect to the electron beam, so that every electron passes through a wall. As a consequence, there appears an asymmetry in the depth for which the radiation can escape from the channel, for Cherenkov radiation emitted upwards and downwards (see Fig. 5.9). For instance, when the tilt angle is 5° and Cherenkov radiation is emitted at 10° (for which the highest intensity is emitted), emission angles with respect to the channel orientation are 5° and 15° respectively for the upward and downward direction. In this example all electrons contribute to the radiation exiting the channel in the upward direction (because the emission angle with respect to the channel orientation is equal to the tilt angle), but in the downward direction only about 1/3 of the electrons contribute to the radiation escaping the channel. The enhancement of the Cherenkov intensity can now be calculated in case of a tilt angle $\alpha = 2°$ and Cherenkov angle $\theta = 5°$, which will be verified in the measurements below. Using the equations for gain and transmission of Sec. 2.3 and the effective depth of the channel, the expected gain in the upward direction is 1.5, which is slightly larger than the intensity in case of normal incidence (gain = 1).

For the experiments a p-type silicon microchannel plate was purchased from NanoSciences Corporation[8]. The microchannel plate has a diameter of 25-mm and 10-μm square channels that are 325 μm deep, with 1-μm walls (see Fig. 5.9). The matrix of channels was oriented in such a way that the walls are oriented vertically and horizontally when the microchannel plate is perpendicular to the electron beam. The orientation of the channels in the plate is slightly tilted (about 1°). In Fig. 5.10 electron microscope images are shown of the microchannel plate.

The detector angle with respect to the electron beam was set to $\Theta = 5°$, because the measurements with a silicon foil showed the highest photodiode signal at this position. The purpose of this measurement is to compare the Cherenkov intensity with the intensity from a single foil. To have a measure for the Cherenkov intensity only two photodiode positions are needed, i.e. $2\theta = 20°$ and $2\theta = 60°$. As we know from Fig. 5.6(a) the first represents soft x-ray and visible radiation and the latter the visible radiation background. By subtraction of the two values the soft x-ray Cherenkov intensity is obtained and can be compared to that for a foil as a function of tilt angle α.
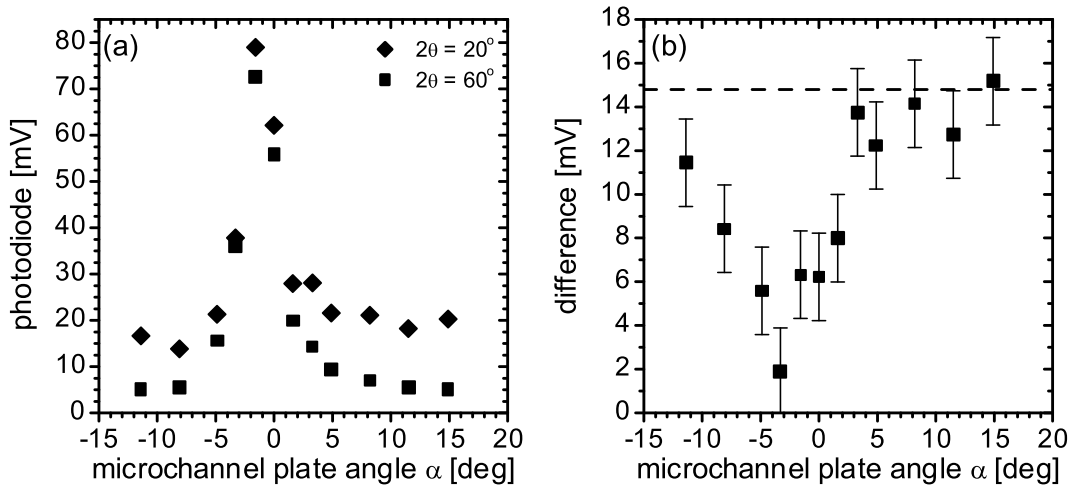
Figure 5.11: (a) The background corrected photodiode signal as function of microchannel plane tilt angle α for two different diode positions, $2\theta = 20°$ (diamonds) and $2\theta = 60°$ (squares) respectively, at $\Theta = 5°$. (b) The corresponding difference between both photodiode signals as function of microchannel plate tilt angle α. The dashed line indicates the intensity from a single foil.

In Fig. 5.11(a) the photodiode signals at $2\theta = 20°$ and $2\theta = 60°$, respectively, are plotted as a function of microchannel-plate tilt angle α. Note that these photodiode signals have been corrected for the hard x-ray background, as described in the previous section, but not yet for the visible light contribution, which is represented by the signal for $2\theta = 60°$. As can be seen the visible light component is high for angles around $\alpha = 0°$, because then the visible light from the electron gun passes easily through the microchannel plate in the direction of the detector. In Fig. 5.11(b) the signal of soft x-ray radiation, which is the difference between the two photodiode signals, is plotted as a function of microchannel plate tilt angle α. Around $\alpha =$

0° a dip is visible. The soft x-ray signal at higher tilt angles is exactly equal to the value obtained from a single foil at multilayer-mirror position θ = 10° [see Fig. 5.8(b)]. This result does not agree with the small enhancement expected on the basis of simple considerations.

It appears that the enhancement of Cherenkov radiation at grazing incidence is more complicated. For instance, we did not take into account the electron beam elastic scattering in the channel walls. As discussed in theory this has probably a negative influence of the gain. Therefore, it seems that the small gain that was expected is counteracted and as a result even less intensity is observed than in case of normal incidence. Grazing-incidence Cherenkov radiation should be investigated in a well-defined geometry, i.e. a single foil.

On the basis of this experiment we conclude that intensity enhancement of Cherenkov radiation by grazing-incidence for 5-MeV electrons, is not very likely due to the electron scattering. Because even in case a very thin foil and a low-divergent electron beam are used, the effective path length through the foil is still large which causes a high number of scattering events.

5.2   Water-window Cherenkov radiation

From Table 2.1 several materials can be selected that emit Cherenkov radiation in the water window. In Fig. 5.12(a) the corresponding calculated spectral yields are plotted using 10-MeV electrons. All materials emit Cherenkov radiation with a typical FWHM width of about 1.5 eV and a yield of a few times 10^{-4} photon per electron. These calculations are based on very few data points of the refractive index, as is illustrated by the susceptibility of titanium around the L-edge (453 eV) in Fig. 5.12(b). With our measurements these predictions can be verified.
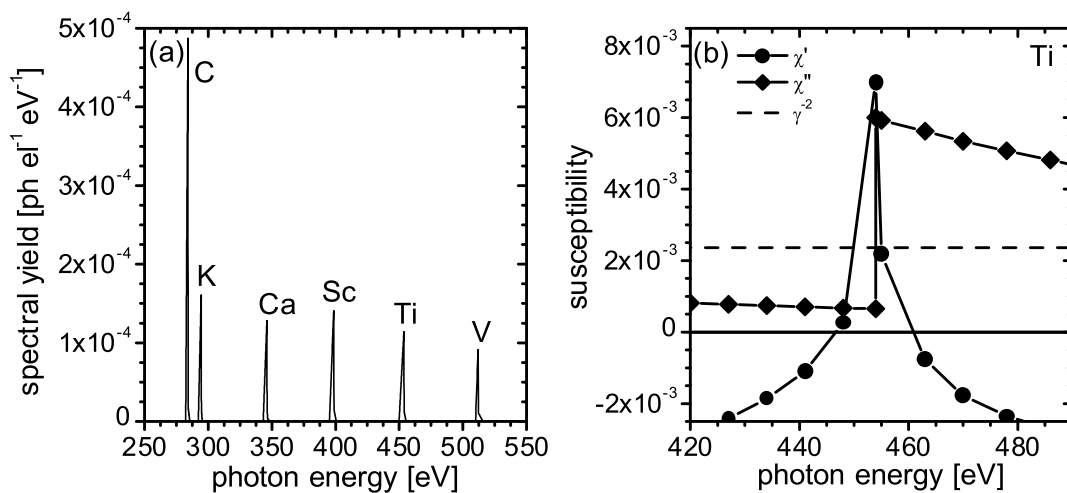

Figure 5.12: (a) The theoretical Cherenkov spectral yield of different materials in the water-window spectral region using 10-MeV electrons. (b) Susceptibility χ of titanium around the L-edge (453 eV). The dashed line indicates the Cherenkov threshold for 10-MeV electrons.

For our first experiments with the 10-MeV electrons from the LINAC-10, titanium (453 eV) and vanadium (512 eV) were selected, because both metals are readily available in 10-µm thick foils, which are purchased at Goodfellow[9] and are 25×25 mm² in size. The measurements discussed in this section have already been reported elsewhere by Knulst *et al.*[10,11]

The results from titanium and vanadium are discussed in parallel, because the measurements are very similar. The foils are mounted in the goniometer, perpendicular to the electron beam. Then, a goniometer angular scan is made from $\Theta = -10°$ to $+10°$ with steps of 1°. Before starting a measurement at a certain goniometer angular position, the electron beam current is adjusted in order to obtain a number of occupied pixels per frame (pixel values above $p + 3\sigma$, see Sec. 4.2.3) between 1×10^4 and 3×10^4, which is acceptable for event reconstruction. At small angles the electron beam current is therefore set to a very low value, because the CCD chip is positioned in the forward direction of the electron beam where the intensity of Bremsstrahlung and transition radiation is high. After the electron beam current has been adjusted, the number of electrons per accelerator pulse is determined.
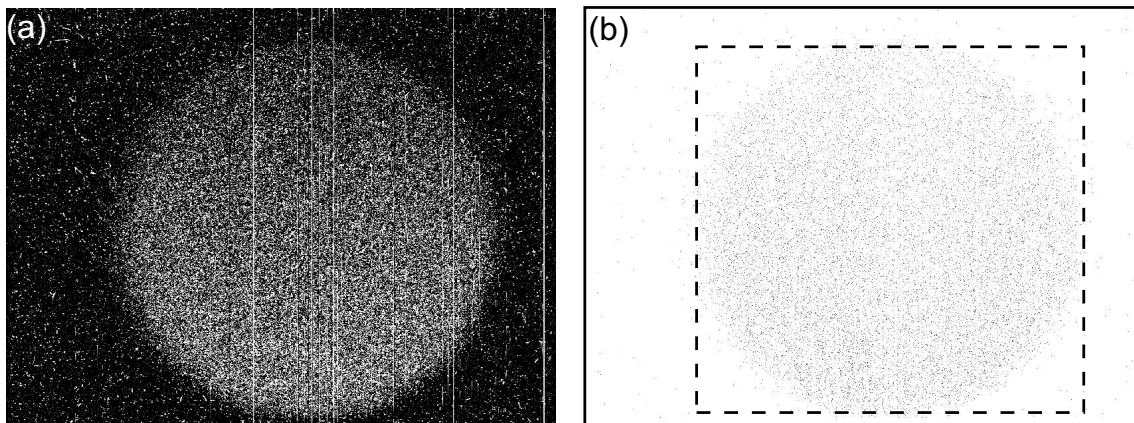
Figure 5.13: CCD chip images of titanium summed over 30 frames measured at $\Theta = -4°$. (a) Intensity image before event reconstruction. (b) Inverted image after event reconstruction with only those photons that have an energy within the Cherenkov peak. The dashed box indicated the region of interest for the Cherenkov radiation analysis.

A measurement with the CCD camera at a certain goniometer angle consists of recording a series of 30 or 60 frames. Each frame has 2 seconds illumination time, during which the accelerator produces a few pulses (typically 3 to 5 pulses) at a repetition rate of $f = 5$ Hz. The accelerator cannot be operated continuously, because during the read out time (which takes typically 20 seconds) the CCD chip is still sensitive to hard x-ray radiation that could influence the measurement. Between measurements of Cherenkov radiation, a system-peak measurement is performed (typically 3 to 5 frames) to check the CCD camera properties, which is needed for the event reconstruction.

In Fig. 5.13(a) the CCD image of a titanium measurement at $\Theta = -4°^*$ is shown before event reconstruction. Because this image is a sum over 30 frames it represents an intensity image, i.e. the whiter the pixel the more photons are detected. The bright circle is the size of

---

* For negative Θ the goniometer moves upwards from the horizontal position.

the Al/C-filter that is placed in front of the CCD chip. Outside the filter diameter fewer photons are detected, which are generally hard x-ray photons that are able to penetrate through the thick filter holder. In Figs. 5.14(a) to 5.14(c) the pulse height spectra summed over 30 frames are plotted that are measured at respectively $\Theta = 0°$, $-4°$ and $-9°$. The corresponding pulse height spectra obtained after event reconstruction are shown in Figs. 5.15(a) to 5.15(c). In Fig. 5.16 three pulse height spectra of vanadium at $\Theta = 0°$, $-4°$ and $-9°$ are plotted after event reconstruction.

Figure 5.14: CCD pulse height spectrum obtained using a titanium foil, summed over 30 frames (before event reconstruction) measured at $\Theta = 0°$ (a), $\Theta = -4°$ (b), and $\Theta = -9°$ (c).

The pulse height spectra of titanium (Fig. 5.15) and vanadium (Fig. 5.16) can be explained in terms of a number of radiation phenomena that are caused by the electron beam while it passes through the target foil. In the pulse height spectra two peaks are clearly distinguished. A strong peak on the low photon-energy side, which is interpreted as Cherenkov radiation (CR) and the weaker peak on the high photon-energy side, which is identified as fluorescence radiation (K_α and K_β). The offset under the Cherenkov peak is a

low intensity, continuous background of transition radiation (TR) that decreases with photon energy and has its maximum intensity at an emission angle of $1/\gamma$, i.e. 2.8° for 10-MeV electrons. The very small background around the fluorescence peak is Bremsstrahlung, which is mainly hard x-rays and is produced when electrons pass through the foil and lose kinetic energy. Bremsstrahlung is also emitted within an angle of approximately $1/\gamma$. By changing the detection angle the relative intensities of these radiation phenomena vary. At large detection angles (e.g. $\Theta = -9°$) the fluorescence radiation, which is emitted isotropically over 4π sr, is dominant, because at these angles the other radiation phenomena are much less intense. This fluorescence radiation is used for the energy calibration of the CCD camera (see Sec. 4.2.3.2). At smaller detection angles (e.g. $\Theta = -4°$ and $\Theta = 0°$) Cherenkov radiation, transition radiation and Bremsstrahlung are dominant. In addition, there is a narrow peak on the left far most side of the spectrum, which is an artifact that always appears after event reconstruction.
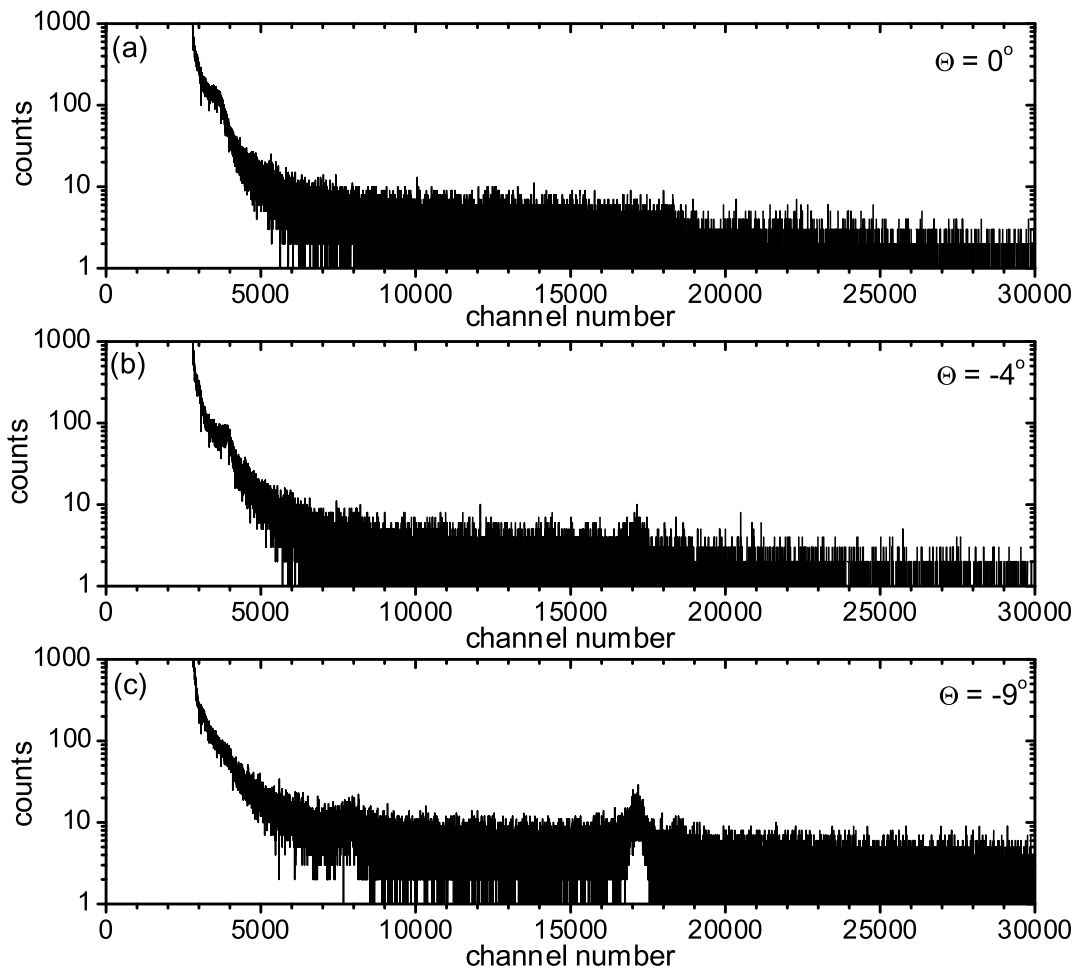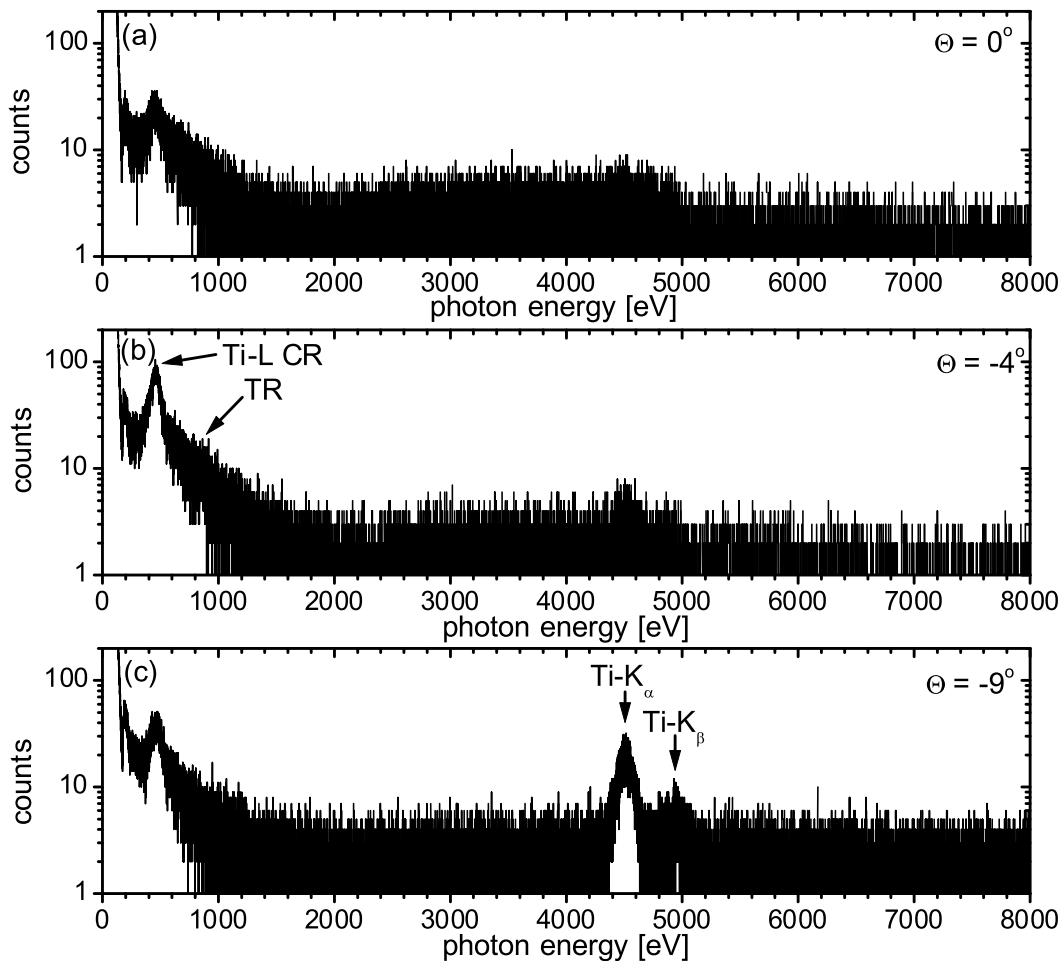

Figure 5.15: CCD pulse height spectrum obtained using a titanium foil, summed over 30 frames (after event reconstruction) measured at $\Theta = 0°$ (a), $\Theta = -4°$ (b), and $\Theta = -9°$ (c).

If only the pixels with photons energies within the Cherenkov peak are selected from, for instance for the case of titanium in Fig. 5.15(b), the CCD-image plotted in Fig. 5.13(b) is

obtained. This shows that the majority of the pixels are within the circle that represents the transmission through the Al/C filter. For all further analysis we have taken a squared window of pixels (dashed line) tide around the Al/C filter in order to lower the background noise with respect to the Cherenkov radiation.
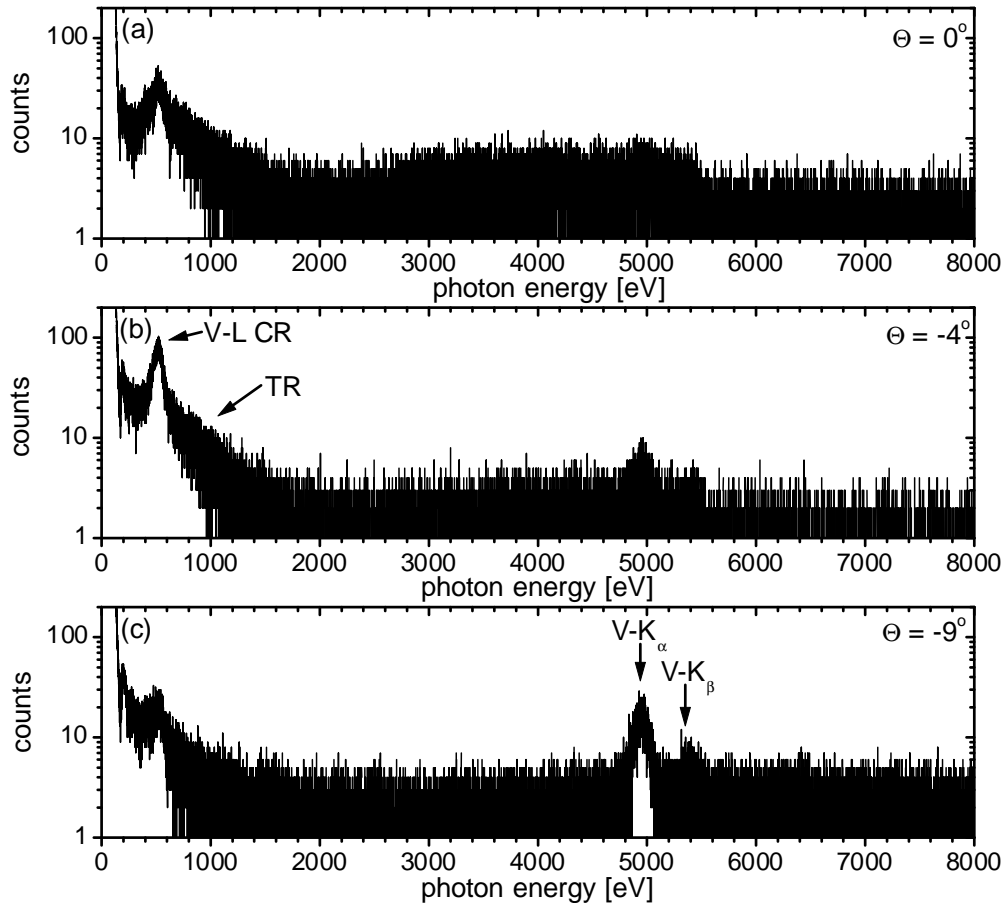
Figure 5.16: CCD pulse height spectrum obtained using a vanadium foil, summed over 30 frames (after event reconstruction) measured at $\Theta = 0°$ (a), $\Theta = -4°$ (b), and $\Theta = -9°$ (c).

Figures 5.17(a) and 5.18(a) zoom in on the Cherenkov peak of titanium and vanadium measured at $\Theta = -4°$. The FWHM width of 98 eV of the measured titanium peak and 102 eV of the measured vanadium peak are completely determined by the spectral resolution of the CCD camera, since the Cherenkov peaks are only a few eV wide (Chapter 2). Therefore, in these small windows the peak can be fitted by a Gaussian profile with a linear offset. Based on the peak positions obtained from the Gaussian fit and on the calibration of the CCD camera, the Cherenkov peaks are experimentally determined at 459 ± 2 eV for titanium and 519 ± 3 eV for vanadium. A small, but significant, difference is observed with the theoretical peak positions at their respective L-edges, i.e. 453 eV and 512 eV. The fact that we measure the peaks at slightly higher photon energies will be explained below.

In Figs. 5.17(b) and 5.18(b) the theoretical spectral yields (dotted lines) are plotted, which are calculated by the Ginzburg-Frank equation (2.82) and integrated over the solid angle of

the detector at an emission angle of 4°. In both spectra clearly the high Cherenkov peak is visible on a low-intensity background of transition radiation decreasing with photon energy. By multiplying these spectra with the transmission of the Al/C-filter the spectra are calculated of the photon flux incident on the CCD chip (dashed curves). Then, by convolving these spectra with the spectral response of the CCD camera, i.e. a Gaussian profile with a FWHM width of 98 eV in the case of titanium and 102 eV in the case of vanadium, the expected CCD camera spectra are calculated (solid curves). The peak positions of the calculated CCD camera spectra are determined at 458 eV for titanium and 522 eV for vanadium. The measured peak positions of both titanium and vanadium agree within the experimental error with the theoretical values obtained from this analysis. These shifts are due to the fact that at a photon energy a few electron-volts below the L-edges the real part of the susceptibility goes through zero and therefore at this specific photon energy both transition radiation and Cherenkov radiation are absent. The resulting dip shifts the peaks to slightly higher energies. In Fig. 5.19 these calculated CCD camera spectra are plotted together with the measured spectra, showing that the low-energy part of the measured spectra is completely described in terms of Cherenkov and transition radiation. For the case of vanadium the measured Cherenkov peak is higher than the theoretical curve, which will be discussed below.
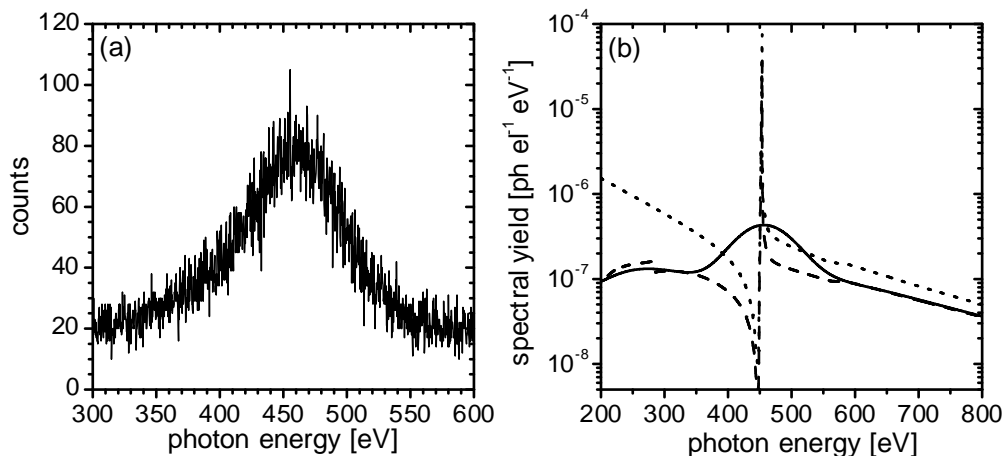
Figure 5.17: (a) The Cherenkov peak of titanium measured at $\Theta = -4°$ [from Fig 5.15(b)]. (b) Theoretical calculation of the expected CCD spectrum starting from the theoretical spectral yield (dotted curve) and multiplied by the transmission of the Al/C-filter (dashed curve) and then taking the convolution with the CCD spectral response (solid curve) for titanium.

It is important to realize that the theoretical spectral FWHM width of Cherenkov radiation is about 2 eV for both titanium and vanadium. Note that the actual height of the Cherenkov peaks is therefore approximately 50 times higher than the measured peaks in the spectra, which can only be observed by using a high-resolution spectrometer. This means that the radiation spectra in the soft x-ray region of both titanium and vanadium are completely dominated by a single intense peak of Cherenkov radiation.
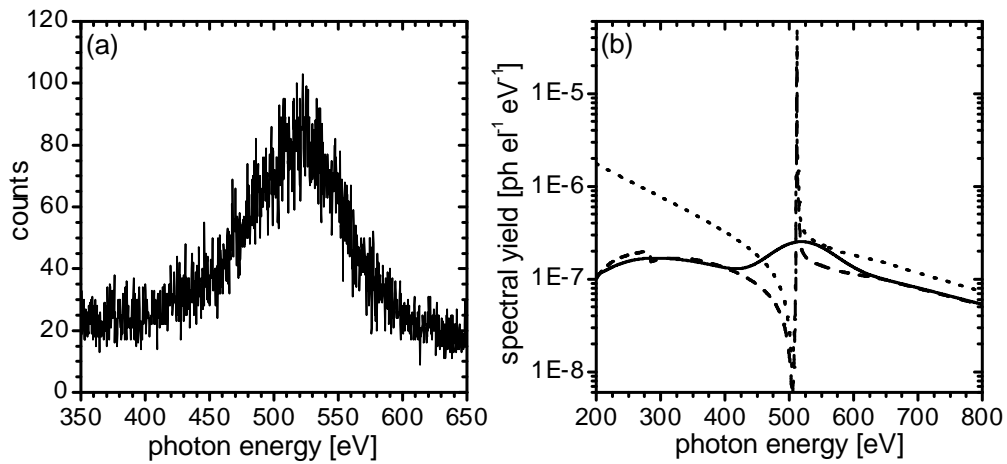
Figure 5.18: (a) The Cherenkov peak of vanadium measured at $\Theta = -4°$ [from Fig 5.16(b)]. (b) Theoretical calculation of the expected CCD spectrum starting from the theoretical spectral yield (dotted curve) and multiplied by the transmission of the Al/C-filter (dashed curve) and then taking the convolution with the CCD spectral response (solid curve) for vanadium.
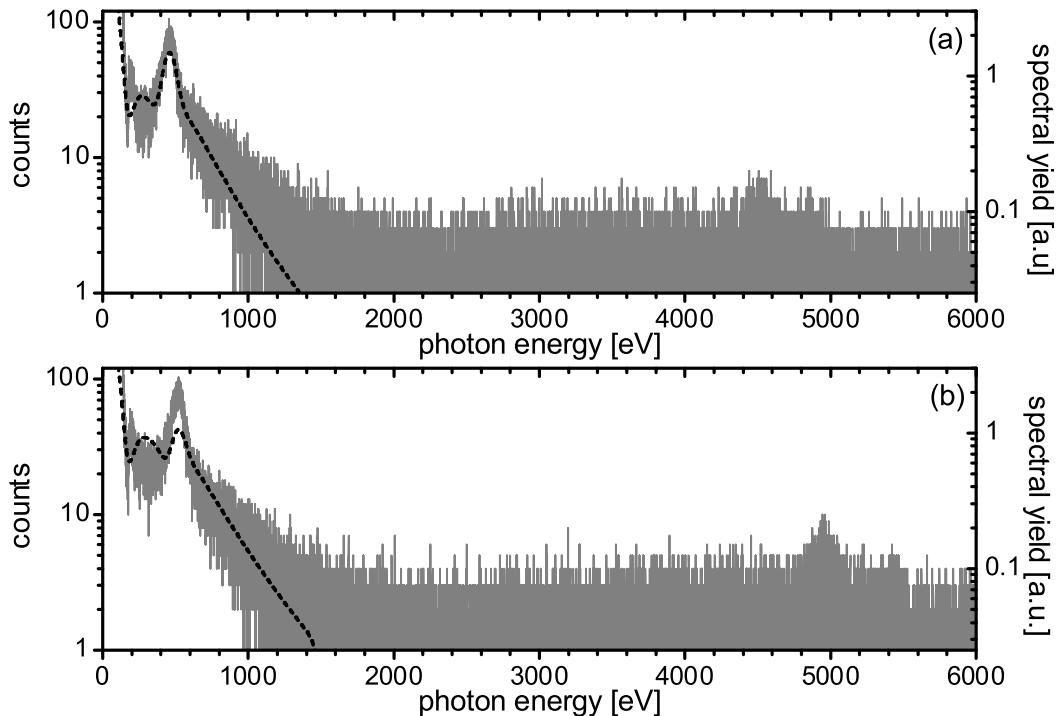
Figure 5.19: Pulse height spectra of the radiation produced by 10-MeV electrons in titanium (a) and vanadium (b) at $\Theta = -4°$. The dashed curves are the calculated CCD spectra from Figs. 5.17(b) and 5.18(b).

Similar spectra as in Figs. 5.15 and 5.16 have been obtained at goniometer angles ranging from $\Theta = -10°$ to $+10°$ for both titanium and vanadium. From each spectrum the area of the Cherenkov peak is determined, which gives the number of photons at each detector position. Then, by taking into account the detection efficiency of the CCD camera (see Fig. 4.12), the transmission of the Al/C-filter, the solid angle of the detector and the number of electrons used to record a spectrum, the angular yield (number of photons per electron per solid angle) can be calculated. The angular yield is shown as a function of goniometer angle in Fig. 5.20(a) for titanium and in Fig. 5.20(b) for vanadium. Clearly, the typical Cherenkov angular profile is seen, i.e. a symmetric profile with a minimum at 0º and with a maximum at the angle associated with the maximum value of the refractive index. The angular profile is broadened due to small-angle elastic scattering that the electrons undergo when passing through the target foil. The divergence of the electron beam before entering the foil can be neglected. Using the results of Chapter 3, we have analyzed the influence of elastic scattering of electrons in the foil on the angular Cherenkov emission profile. The angular Cherenkov radiation distribution $f(\theta)$ of a scattered electron beam is calculated by a small-angle, 2-D convolution (see Sec. 3.3), given by

$$f(\theta) = \iint g(\theta')h(\theta'')\theta' d\theta' d\varphi', \tag{5.1}$$

in which $g(\theta)$ is the electron distribution and $h(\theta)$ is the Cherenkov radiation angular distribution. The angles are related by

$$\theta''^2 = \theta^2 + \theta'^2 - 2\theta\theta'\cos(\varphi'). \tag{5.2}$$

The electron distribution $g(\theta)$ has been calculated using Molière's theory of multiple scattering[12] that applies to the 10-µm foils, for which the average number of scatterings per electron is 42 for titanium and 56 for vanadium. The resulting scattering distributions have an average scattering angle of, respectively, 1.1° and 1.3°. The Cherenkov radiation distribution $h(\theta)$ is calculated by integrating the Ginzburg-Frank equation (2.81) over the photon energies for which the Cherenkov condition is satisfied (dotted curves in Fig. 5.20). The resulting photon distributions for the scattered electron beam are indicated by the solid curves in Fig. 5.20. This broadening effect explains the non-zero angular yield value at 0° and the less steep drop for angles higher than the maximum intensity. The measured angular profiles are also shifted slightly with respect to the theoretical curves, which is probably due to a small misalignment of the electron beam.

Integrating the measured angular distribution over all emission angles we find a total yield of 3.5×10^{-4} photon/electron for titanium and 3.3×10^{-4} photon/electron for vanadium. For titanium this is slightly higher than the theoretical value of 2.4×10^{-4} photon/electron. For vanadium the experimental value is more than twice as high as the theoretical value of 1.4×10^{-4} photon/electron. In view of the fact that the calculation is based on the only two refractive index data points available, i.e. the maximum value at the edge and one data point below the Cherenkov threshold, the measured spectra and angular profiles agree very well with the theoretical predictions. The fact that the yield of vanadium is higher than theoretically expected, can be explained by assuming that the peak in the refractive index at the L-edge is slightly broader than according to the data of Ref. 7. A higher peak in the refractive index data cannot explain the higher yield of vanadium, because this would give

rise to a larger Cherenkov angle. The spectral resolution of the CCD camera is far too low to directly measure the actual Cherenkov radiation line width.
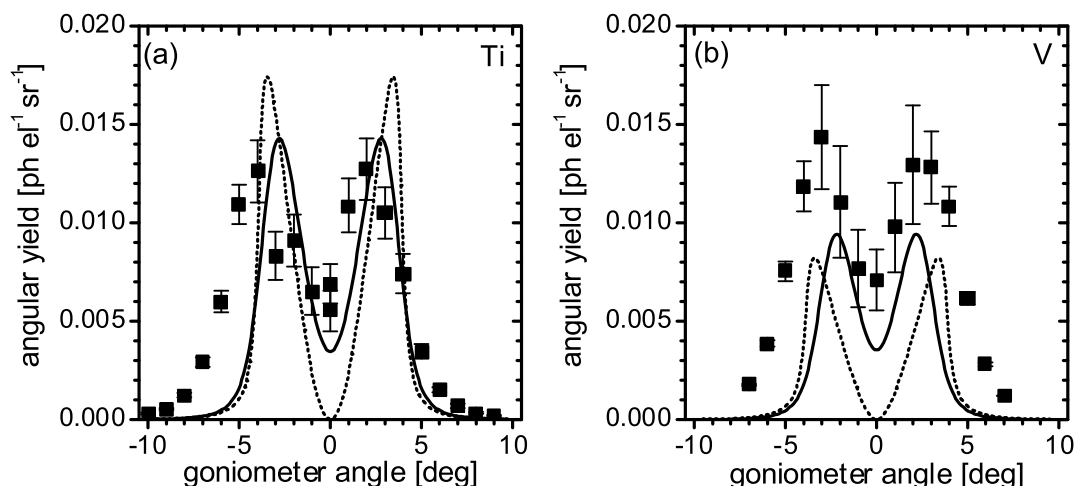
Figure 5.20: Measured Cherenkov angular yield as a function of detection angle generated by 10-MeV electrons in titanium (a) and vanadium (b). The dotted curves are theoretical angular Cherenkov yields for an ideal parallel electron beam. The solid curves take elastic scattering of the electron beam in the foil into account.

In summary, these measurements are the first observations ever of Cherenkov emission lines in the water-window spectral region. From these measurements it is concluded that the Cherenkov spectrum consists of a narrow, strong peak on top of a low intensity background. The soft x-ray Cherenkov radiation intensity is much higher than the transition and fluorescence radiation intensity. The theoretical predictions are remarkably accurate, in view of the very limited refractive index data that are available. Apparently, for titanium the data at the L-edge are quite accurate. For the case of vanadium we conclude on the basis of the Cherenkov yield measurements that the anomalous dispersion at the L-edge is broader than in the Henke database. This shows that the Cherenkov radiation may be a tool to validate the refractive index value at specific inner-shell absorption edges. Especially in the narrow spectral region at the absorption edge it is difficult to directly measure the refractive index using other methods. The resulting brightness and implications for source development are discussed in Chapter 6.

5.3   Other materials

5.3.1   C-K measurements

Carbon-K (284 eV) Cherenkov radiation has been observed two times before, using, respectively, 1.2-GeV[2] and 75-MeV[1] electrons. We set out to demonstrate that 10-MeV electrons should be already sufficient. In Fig. 5.21(a) the susceptibility of carbon is plotted as

a function of photon energy around the K-edge. There is only one data point that exceeds the 10-MeV threshold, but it is sufficiently high and therefore, like in the case of titanium and vanadium, C-K Cherenkov radiation is very likely. The angle of maximum intensity is expected at 4.2°. In Fig. 5.21(b) the predicted spectral yield is plotted using 10-MeV electrons. By integrating over the Cherenkov line a total yield of 4.8×10^{-4} photon/electron is calculated. It is important to mention that the refractive index of carbon used in these calculations is based on a density of $\rho = 2.2$ g/cm^3.
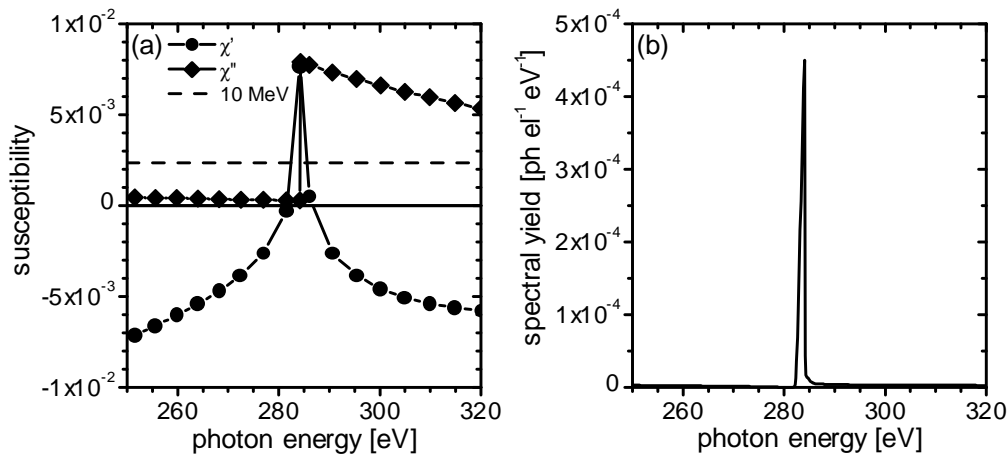
Figure 5.21: (a) Susceptibility of carbon around the K-edge (284 eV) for $\rho = 2.2$ g/cm^3. The dashed line indicates the threshold for 10-MeV electrons. (b) The calculated spectral yield of carbon using 10-MeV electrons.

Carbon foils come in many forms with a large spread in density, which has to be taken into account, because the refractive index is proportional to the density [see Eq. (2.25)]. Therefore, several different foils have been tested. Two foils have been purchased at ACF-Metals[13]: an evaporated (amorphous) carbon foil (standard type) of 1600 µg/cm^2 and a polycrystalline graphite foil (PCG type) of 2000 µg/cm^2. The first foil has a density of 1.83 ± 0.03 g/cm^3, which is typical for thick evaporated carbon layers, corresponding to a thickness of about 8.7 µm. The PCG foil is composed of graphite microcrystals and is porous. Therefore, the average density of such a foil ranges between 0.8 and 1.2 g/cm^3. Thus, the estimated thickness of the purchased PCG foil is about 20 µm, but due to the porosity it has a nonuniformity of about 40%. For this foil it is hard to predict the Cherenkov radiation output, because it is unclear which density has to be used: the density of the microcrystals (about 2.0 g/cm^3) or the average density (about 0.8-1.2 g/cm^3). In addition, we have a diamond foil at our disposal.

In Figs. 5.22(a) and 5.22(b) the spectra are shown that have been recorded at $\Theta = -4°$ for respectively evaporated foil and PCG foil. Also spectra have been recorded at other goniometer angles. However, there was no Cherenkov peak visible in these spectra around the position of the carbon K-edge 284 eV.

Figure 5.23 shows the spectra obtained with the diamond foil. This time all the spectra have been plotted in one graph, normalized to the number of electrons per spectrum. Also in

these spectra there is no Cherenkov peak visible. The shape of the spectra, mainly transition radiation, hardly changes as function of goniometer angle, but the intensity decreases with increasing goniometer angle.
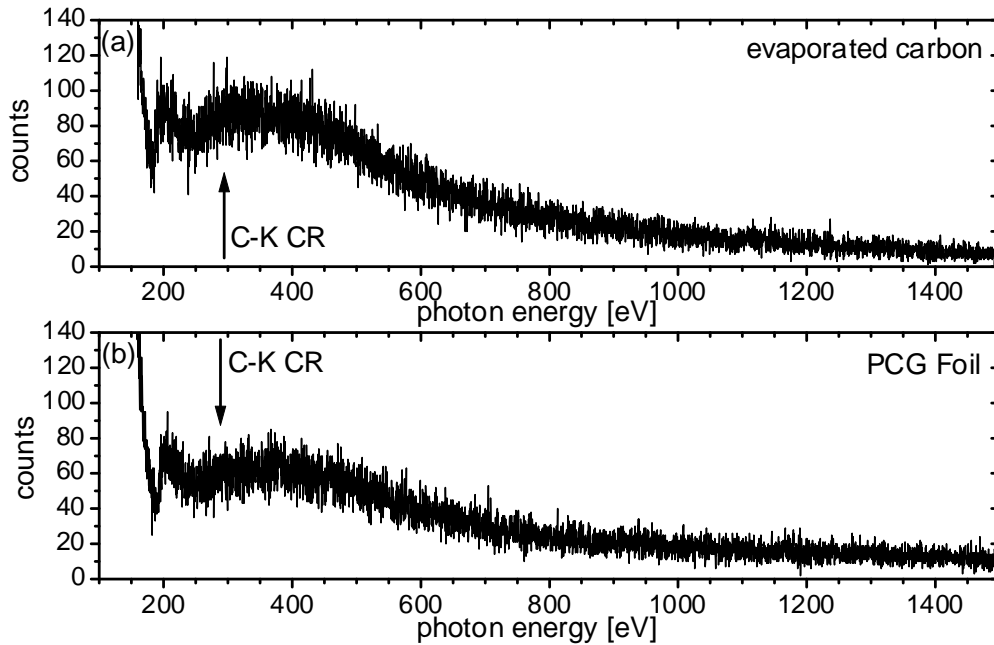
Figure 5.22: CCD spectrum obtained at $\Theta = -4°$ using (a) evaporated carbon (b) polycrystalline graphite (PCG) foil.
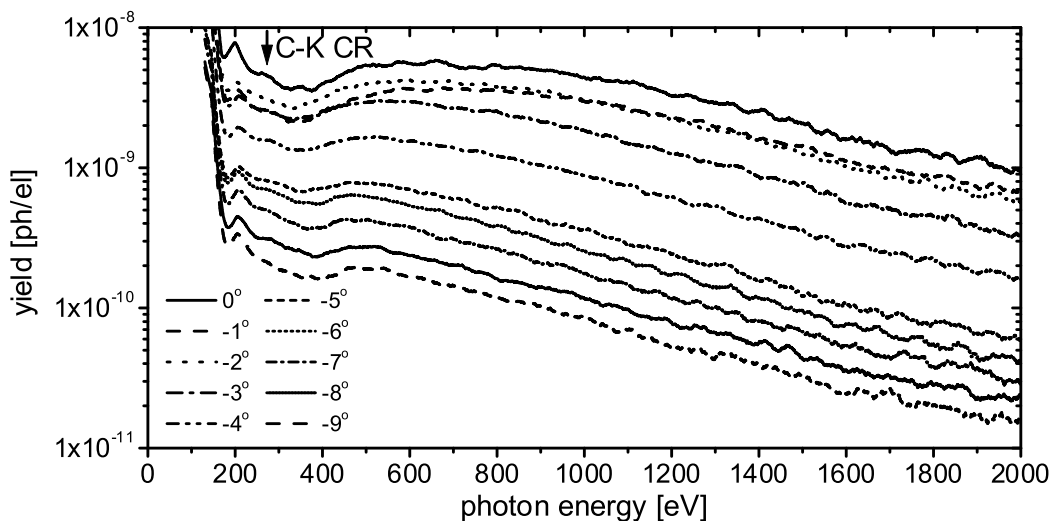
Figure 5.23: CCD spectra obtained using the diamond foil, as function of goniometer angle Θ, normalized to the number of electrons and smoothed over 100 channel numbers.

The fact that we did not observe C-K Cherenkov radiation using 10-MeV electrons is unexpected, because the Cherenkov condition is amply fulfilled according to the refractive index data. For titanium and vanadium the maximum value of the refractive index data agrees very well with the measurements. Therefore, we conclude from the carbon measurements that the refractive index peaks less than according to Ref. 7. A new upper limit of the refractive index can be set based on our measurements with 10-MeV electrons, i.e. $\chi'_{max} = (2.4 \pm 0.3) \times 10^{-3}$.
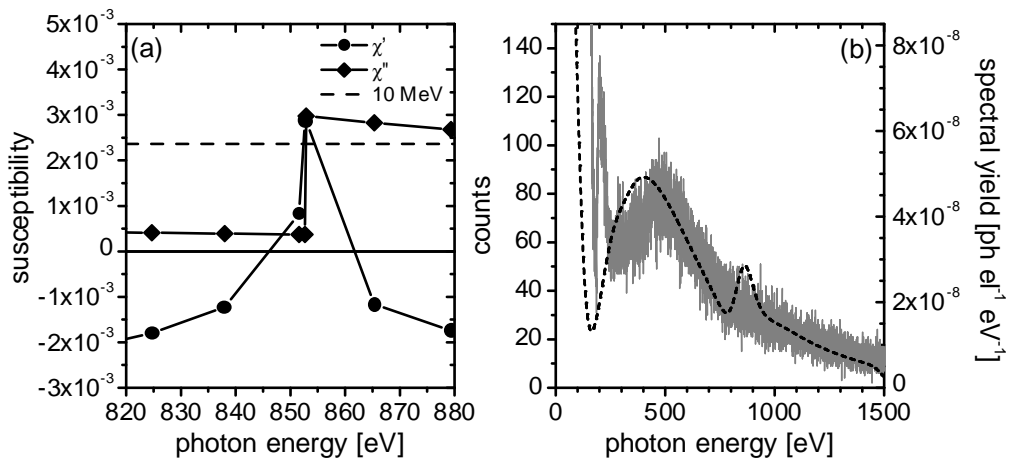

Figure 5.24: (a) Susceptibility χ of nickel around the L-edge (852.7 eV). The dashed line indicates the threshold for 10-MeV electrons. (b) Pulse height spectra of the radiation produced by 10-MeV electrons in nickel at $\Theta = -1°$. The dashed curve is the calculated CCD spectrum.

5.3.2 Ni-L measurements

We have also tried to demonstrate that Cherenkov radiation with a photon energy higher than the water window can be generated by 10-MeV electrons. In Fig. 5.24(a) the susceptibility of nickel is plotted around the L-edge (852.7 eV). The susceptibility peaks just above the threshold value for 10-MeV electrons. Based on these values the maximum intensity is expected at an emission angle of about 1°. We have purchased a 10-μm thick nickel foil of 25×25 mm^2 (Goodfellow[9]). We have performed a complete goniometer angular scan.

In Fig. 5.24(b) the recorded spectrum at $\Theta = 1°$ is plotted together with the theoretical calculation, which is analogue to the titanium and vanadium calculations. Despite the high number of frames used to obtain this spectrum, no Cherenkov radiation is observed, nor in other spectra at different goniometer angles. The theoretical curve shows that the Ni-L Cherenkov peak should just exceed the noise in the transition radiation spectrum. Since we do not observe this, it is very likely that the value of the real part of the susceptibility of nickel at the L-edge is slightly lower than given by Ref. 7. On the other hand, we have not taken into account elastic scattering of the electron beam, which can broaden the angular radiation distribution (see Fig. 5.20) and have a decreasing effect on the intensity. Nickel might still be a Cherenkov emitter, but higher electron energies are needed. The same holds probably for

Cu, which is the next element in the periodic table with a threshold below 10 MeV (see Table 2.1).

5.3.3   N-K measurements from Si_3N_4

We have also done measurements on Si_3N_4 to test if chemical compounds can emit Cherenkov radiation using 10-MeV electrons. The investigation of chemical compounds is of interest for two reasons: First, the chemical binding can slightly shift an absorption edge, for instance the silicon L-absorption edge is slightly shifted to higher photon-energies (103 eV) when the silicon atoms are either in a nitride or oxide environment. Because Cherenkov radiation is associated with an absorption edge, the consequence might be that the photon energy of the generated radiation is also shifted. Moreover, the resonant behavior of χ' may be changed, thus elements that do not radiate in their pure state, may radiate Cherenkov radiation in a compound. These possible effects due to chemical bindings are not taken into account when retrieving optical data of a chemical compound at the CXRO-website[7].
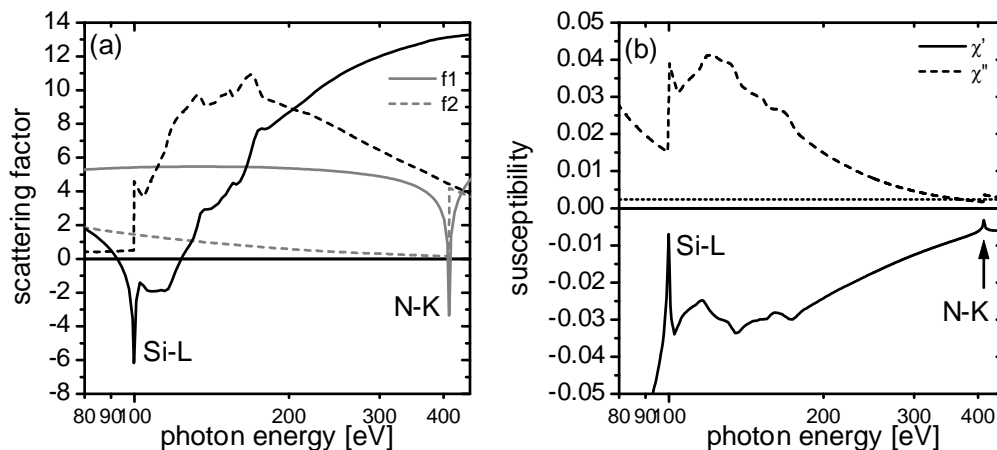
Figure 5.25: (a) Complex scattering factor ($f = f_1 + i \cdot f_2$) of nitrogen (gray curve) and silicon (black curve). (b) Complex susceptibility of Si_3Ni_4 with a density of 3.44 g/cm^3, obtained from the CXRO-website.

A second reason compounds are interesting is that elements that are not readily available in the solid state can be part of a chemical compound in the solid state, such as oxygen in oxides and nitrogen in nitrides. Therefore, the dielectric constant of gases, which exceeds unity at absorption edges very slightly due to the low density, might be increased in the solid chemical compound. Lower electron energies are then sufficient to generate Cherenkov radiation at that edge.

We have chosen to take the chemical compound Si_4N_3 to study the generation of N-K Cherenkov radiation with the CCD camera using the LINAC-10 setup. Interestingly, the scattering factor of nitrogen (this also holds for oxygen, but this is not further analyzed in this section) becomes negative at the K-edge (410 eV), as is shown in Fig. 5.25(a). If the partial nitrogen density is sufficiently high, Cherenkov radiation may be generated. In Fig. 5.25(b)

the susceptibility of Si_3N_4 is plotted according to the CXRO-website. Although the refractive index does not peak above unity at the nitrogen K-absorption edge, it can have a stronger resonance due to the chemical environment than according to this data.

A Si_3N_4 sample has been made at the FOM-institute AMOLF. The top layer of a silicon wafer was transformed into silicon nitride. Then, from the back of the wafer a square area of 8x8 mm^2 was etched away, leaving a thin silicon nitride membrane of 300-nm thickness behind. In Fig. 5.26 the measured spectra normalized to the number of electrons per spectrum are plotted for different goniometer angles. The Cherenkov peak is expected around 410 eV, but in the angular profiles no peak is visible at that position. For larger goniometer angles a peak appears around channel number 5500, which can be identified as silicon K_α-fluorescence radiation. By taking a close look at the transition radiation spectra for different goniometer angles, one can see that the spectra change shape, while the carbon profiles in Fig. 5.23 keep their shape for different goniometer angles. This effect is due to interference between transition radiation generated at the first interface, when the electrons enter the membrane, and the second interface, when the electrons exit the membrane. This can only be observed for photon energies higher than 300 eV, for which the absorption length is larger than the thickness of the foil. This has been confirmed by simulations using the code of Lastdrager[14].
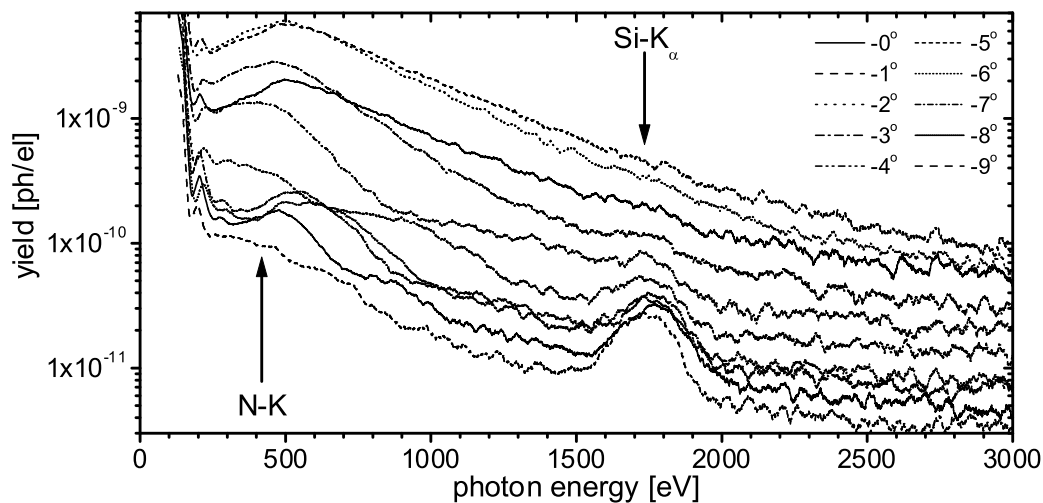
Figure 5.26: CCD spectra obtained using Si_3N_4, normalized to the number of electrons and smoothed over 100 channel numbers by averaging, as a function of goniometer angle Θ. The target thickness allows interference of transition radiation from front and back interface of the 300-nm thick foil.

On the basis of these measurements we conclude that no N-K Cherenkov radiation can be generated with 10-MeV electrons in a Si_3N_4 foil. The partial nitrogen density is apparently too low to sufficiently counteract the scattering factor of silicon ($f_1 \approx 13$ at 410 eV) in the water window (see Fig. 5.25). To have a larger probability of generating Cherenkov radiation at the nitrogen K-edge, the nitrogen fraction should be larger than the 'host' element, like silicon in this case, or the 'host' element should have a low scattering value at that photon energy, for example carbon with $f_1 \approx 5$ at 410 eV.

References

1 M.J. Moran, B. Chang, M.B. Schneider and X.K. Maruyama, "Grazing-incidence Cherenkov X-ray generation", Nucl. Instrum. Methods **B48**, 287 (1990).

2 V.A. Bazylev, V.I. Glebov, E.I. Denisov, N.K. Zhevago, M.A. Kumakhov, A.S. Khlebnikov and V.G. Tsinoev, "X-ray Cerenkov radiation. Theory and experiment", Sov. Phys. JETP **54**, 884-892, 1981.

3 W. Knulst, O.J. Luiten, M.J. van der Wiel and J. Verhoeven, "Observation of narrow-band Si L-edge Cerenkov radiation generated by 5 MeV electrons", Appl. Phys. Lett. **79**, 2999-3001, 2001.

4 R. Brummans, *Generation of soft x-ray Cherenkov radiation at grazing incidence*, Internal Graduation Report FTV/TIB 2003-01, Eindhoven, 2003.

5 Virginia Semiconductors Inc., http://www.virginiasemi.com.

6 F. van Kempen, *Extreme ultraviolette Cherenkov-straling opgewerkt in silicium*, Internal Traineeship Report FTV-TIB 2001-07, Eindhoven, 2001.

7 B.L. Henke, E.M. Gullikson and J.C. Davis, "X-ray interactions: photoabsorption, scattering, transmission, and reflection at E=50-30000 eV, Z=1-92", *At. Data and Nucl. Data Tables* **54**(2), 181-342 (1993). [Online] Available: http://www-cxro.lbl.gov.

8 NanoSciences Corporation, http://www.nanosciences.com.

9 Goodfellow, http://www.goodfellow.com.

10 W. Knulst, M.J. van der Wiel, O.J. Luiten and J. Verhoeven, "High-brightness, narrowband and compact, soft x-ray Cherenkov sources in the water window", *Appl. Phys. Lett.* **83**, 4050-4052 (2003).

11 W. Knulst, M.J. van der Wiel, O.J. Luiten and J. Verhoeven, "High-brightness, compact soft x-ray source based on Cherenkov radiation", in Proceedings of SPIE Annual Meeting 2003 in San Diego, 2003.

12 H.A. Bethe, "Molière's Theory of Multiple Scattering", *Phys. Rev.* **89**, 1256 (1953).

13 ACF-Metals, http://www.techexpo.com/firms/acf-metl.html.

14 B. Lastdrager, *Transition radiation and Cherenkov radiation. Classical and quantum mechanical calculations*, Graduation Report Universiteit van Amsterdam, Amsterdam, 1997.

6 Towards a compact soft x-ray Cherenkov source

In the previous chapter it was shown that soft x-ray Cherenkov radiation can be efficiently generated by moderate electron energies. In this chapter we explore the feasibility of using the Cherenkov effect as a compact source in the soft x-ray region. In Sec. 6.1 the quality of the soft x-ray Cherenkov source is discussed, which is expressed in the quantity brightness. To make an estimation of what is actually achievable, two important limitations, i.e. heat load and accelerator quality, are discussed. It turns out that the estimated brightness figures of the soft x-ray Cherenkov source in the water window are comparable to the values of laser-produced plasma sources. After having established the source brightness, the collection of the generated soft x-ray Cherenkov radiation is discussed in Sec. 6.2. Finally, in Sec. 6.3 it is shown that the proposed soft x-ray Cherenkov source fulfills the requirements for soft x-ray microscopy and for x-ray photoelectron spectroscopy. The first application is based on a linear accelerator scheme, while the latter is based on a betatron scheme.

6.1 Quality of the soft x-ray Cherenkov source

The quality of a source can be expressed in the quantity brightness B, which is defined as the radiated power ΔP per unit area ΔA and per unit solid angle $\Delta\Omega$[1]:

$$B = \frac{\Delta P}{\Delta A \, \Delta\Omega}.$$ (6.1)

The spectral brightness is the brightness per unit relative spectral bandwidth,

$$B_{\Delta\omega/\omega} = \frac{\Delta P}{\Delta A \, \Delta\Omega \, \Delta\omega/\omega}.$$ (6.2)

In the x-ray community the spectral brightness is usually expressed in the unit $\text{ph}\cdot\text{s}^{-1}\cdot\text{mm}^{-2}\cdot\text{mrad}^{-2}\cdot0.1\%\text{BW}^{-1}$, where BW is the bandwidth. In a lossless optical system without aberrations the brightness at the source is equal to the brightness in the image plane.

It is thus an important value in designing microscopes and other imaging systems, because it determines the theoretically maximal resolution that can be obtained.

The maximum brightness of the soft x-ray Cherenkov source is obtained by sending as many electrons as possible through the target foil with the smallest possible spot size. In this section we discuss limiting factors on the brightness when designing an actual Cherenkov source. In Sec. 6.1.1 the heat load of the electron beam on the target foil is discussed, which restricts the maximum current density that can be sent through the target foil. Then, in Sec. 6.1.2 two different types of compact electron accelerators are presented. In both cases the typical achievable average current and spot size are reviewed. Finally, in Sec. 6.1.3 the maximum achievable brightness is presented for silicon, titanium and vanadium L-edge Cherenkov radiation taking into account the above limitations.

6.1.1   Thermal limitations

Relativistic electrons lose a tiny fraction ($\approx 10^{-4}$) of their kinetic energy when passing through a µm-thick foil. The energy lost goes partly into Bremsstrahlung and other radiation emission effects and partly into heat. When a high average current is sent through a foil, the total amount of energy deposited in the foil can be quite large, which may lead to significant heating of the foil. The foil may be cooled by either conduction or radiation. In practice the melting point of the target material determines the maximum allowable temperature rise. In this section estimations are made of the temperature of the foil as a function of average current and spot size of the electron beam. These two parameters limit in principle the maximum brightness that can be achieved for a soft x-ray Cherenkov source, irrespective of the accelerator performance.

Table 6.1: Collision stopping power and collision energy loss per unit path length (dE/dx) for 10-MeV electrons.

Material	Collision stopping power [MeV cm^2 g^{-1}]	Collision energy loss [keV µm^{-1}]
Silicon	1.697	0.40
Titanium	1.51	0.68
Vanadium	1.466	0.89

The energy loss of a relativistic electron when traveling through a medium is described by the stopping power, which is a function of the incident electron energy and material properties. The stopping power is divided into two parts, a radiative and collision part. To estimate the energy loss of the particle that is transferred into heat, the collision stopping power has to be used. This value describes the average rate of energy loss per unit path length due to Coulomb collisions that result in the ionization and excitation of atoms. In Table 6.1 these collision stopping power values are specified for the three Cherenkov emitting materials together with the energy loss of 10-MeV electrons passing through a 1-µm layer of those materials.

Electron accelerators are pulsed electron sources with a pulse duration of typically 2 µs. The heat from a single accelerator pulse is deposited in a volume determined by the electron-beam spot size and the thickness of the foil. Assuming the cooling is negligible during the pulse, the temperature rise ΔT of this volume can be expressed as function of average current density $\bar{J} = fQ_{pulse}/A$ sent through the foil:

$$\Delta T = \frac{dE/dx}{C\rho} \frac{Q_{pulse}}{A} = \frac{dE/dx}{C\rho} \frac{\bar{J}}{f} \tag{6.3}$$

with C the specific heat capacity, ρ the mass density, dE/dx the electron energy loss per unit pathlength due to collisions, f the pulse frequency of the accelerator, Q_{pulse} the total charge per pulse and A the electron beam spot size. In Table 6.2 the thermal properties of the Cherenkov emitting materials are summarized. When taking the melting temperature as the limit, the maximum current density turns out to be $\bar{J} \approx 2 \ \text{mA}/\text{mm}^2$ for all three materials, assuming $f = 300$ Hz.

Table 6.2: Thermal properties of Cherenkov emitting materials.

Material	Density	Melting temperature	Specific heat capacity	Heat conductivity[*]	Diffusion coefficient
	[g cm^{-3}]	[K]	[J K^{-1} g^{-1}]	[W cm^{-1} K^{-1}]	[cm^2 s^{-1}]
Silicon	2.33	1687	0.703	0.8-1.5	0.5-0.92
Titanium	4.5	1941	0.523	0.219	0.093
Vanadium	6.1	2183	0.486	0.307	0.10

[*] specified between 273 K and 373 K

During the time between the accelerator pulses the heat is conducted in the direction of the edge of the foil. The temperature profile in the foil $T(\mathbf{r},t)$ can be calculated from the diffusion equation,

$$\rho C \frac{\partial T}{\partial t} = \kappa \nabla^2 T + P_{source} - P_{sink} , \tag{6.4}$$

with κ the heat conductivity and P the power per unit volume deposited in the foil by the electron beam (*source*) and cooled at the edge of the foil (*sink*). The heat diffusion speed can be characterized by the diffusion coefficient D, which is defined as

$$D = \frac{\kappa}{\rho C} . \tag{6.5}$$

In Table 6.2 the calculated values for the three different materials are listed. Because the target foils are very thin, the heat diffusion is 2-dimensional. In case the power is dumped in a very short time and the heat sink is far away from the source, the shape of the temperature profile as a function of time is described by $\exp(-r^2/4\pi Dt)$. During the time between the accelerator pulses ($f = 300$ Hz) the temperature profile has typically extended by about 0.6 mm for the case of titanium and vanadium and about 1.4-2.0 mm for the case of silicon. This distance is too small to reach the boundary of the foil and thus insufficient to have it cooled

down before the next accelerator pulse arrives. However, when focusing an electron beam down to a spot diameter of 0.1 mm or smaller, the temperature profile has extended significantly. This is of importance for cooling by radiation, because the dissipated power is proportional to the hot area.

So far, we have analyzed that conductivity cannot contribute significantly to the cooling of the foil. Instead, the heat should be radiated from the surface of the foil. The radiated power is given by the black body radiation, i.e.

$$P_{rad} = \varepsilon \sigma A T^4 \tag{6.6}$$

with ε the emissivity, which is a factor describing the emission efficiency compared to an ideal black body, $\sigma = 5.67{\times}10^{-8}$ W m^{-2} K^{-4} the constant of Stefan-Boltzmann and A the radiative area. Typically, the value of the emissivity is between 0.2 and 0.8.

On average, the deposited heat due to energy loss of the electron beam should be equal to the radiated power from the front and back surface for a certain temperature of the foil and current density. By putting a limit on the maximum allowable temperature rise ΔT of the foil, for instance, to 75% of the melting temperature, the maximum average current is given by,

$$\bar{I} = \frac{2\varepsilon\sigma A^* T_0^4}{dE/dx\,d}\left[\left(1 + \frac{\Delta T}{T_0}\right)^4 - 1\right] \tag{6.7}$$

with T_0 is the temperature of the surroundings, d the foil thickness and A^* the effective black body radiation area. Assuming that the radiative area is equal to the electron beam spot size and taking a 1-μm foil thickness, the maximum average current density turns out to be about $\bar{J} \approx 0.2\,\text{mA}/\text{mm}^2$ for all three materials and $\varepsilon = 0.2$. This is a lower limit of the maximum achievable brightness, because it is based on a conservative estimation.

If the electron beam is focused to a spot size smaller than 1 mm, heat conduction between the accelerator pulses enlarge the effective radiative area to about a 1-mm spot as we have analyzed before. Then, it turns out that the temperature rise due to a single accelerator pulse is the limiting factor again ($\bar{J} \approx 2\,\text{mA}/\text{mm}^2$). Assume a 0.1-mm spot size, the maximum average current that is allowed without melting the surface is 0.02 mA for the three materials. In conclusion, the highest brightness value is limited to the Cherenkov radiation generated by a 0.02-mA average current electron-beam of 10-MeV that is focused to a spot size of 0.1 mm on a 1-μm thick target foil.

We have shown that the energy loss of a strongly focused electron beam, which is deposited in a small volume, limits the brightness. To increase the average current density, two solutions can found that lead to a lower temperature rise. The first option is to increase the pulse frequency of the accelerator, however, higher than 1 kHz is not easily feasible. The second is to increase the volume in which the heat is deposited, for instance, by making a rotating target foil. High-flux x-ray tubes make use of this solution, i.e. a rotating anode. As an example, to increase the volume effectively by a factor 10, a target disk of 10-cm diameter should rotate at about 10 Hz. In this case, an average current of 0.2 mA on a 0.1-mm spot size is allowed ($\bar{J} \approx 20\,\text{mA}/\text{mm}^2$). As we will show later in Sec. 6.1.3 this current density gives a promising value for the brightness of the soft x-ray Cherenkov source that is comparable to other compact x-ray sources.

6.1.2   Compact electron accelerators

In this section two different accelerator schemes for the compact Cherenkov source are discussed. The first scheme is based on a linear accelerator of which the full current is sent through a foil only once (Sec. 6.1.2.1). This scheme has the advantage that accurate control of the electron spot size on the target foil is possible. The second scheme is based on a betatron of which the relatively low current electron beam is circulated many times through the foil (Sec. 6.1.2.2). This scheme has the advantage that the total charge accelerated is rather low, and therefore the background intensity is very low. Both compact accelerators can produce electron energies in the range from 5 MeV to 35 MeV. Although the betatron has received little attention since the development of high-current linear accelerators, we show that for the case of a Cherenkov source it can have several advantages.

6.1.2.1   **Linear accelerator**

Linear accelerators are widely used in industry, e.g. for x-ray inspection, and in health care, especially radiation treatment, because these accelerators produce high average currents and are compact in size. Typically, the compact accelerators that are commercially available produce up to 10-MeV electrons, with an average current of about 1 mA, which represents a beam average power of 10 kW. Because these accelerators are optimized to operate at high current, the beam is characterized by an energy spread of a few percent and a low emittance ($\approx$ 10 mm mrad, unnormalized), which limits the focusability to a spot size of about a millimeter (i.e. $\bar{J} \approx 1\,\mathrm{mA/mm^2}$).

In the pursuit for a high-brightness Cherenkov source much can be gained by increasing the current density on the target foil by focusing the electron beam with dedicated charged particle optics to a small spot size in the range of 0.1 mm to 0.01 mm. This spot size should be reached while keeping the divergence smaller than the Cherenkov emission angle, so that the angular radiation distribution is not seriously broadened. This requires better emittance values and lower energy spread. For the case of commercially available, compact, linear accelerators better emittance always goes at the expense of beam current, because they are not developed for such high-brightness applications. On the basis of our experience we claim that an accelerator delivering a current density of 0.2 mA on a 0.1-mm spot size can be developed.

The main advantage of the linear accelerator is the high average current and having the control of the beam spot on the target foil by additional charged particle optics. The disadvantage is that the beam is used only once to produce the radiation, while losing just a very small amount of energy, and therefore having a very low efficiency. In addition, the full beam contributes to the x-ray background radiation, which requires relatively thick shielding.

6.1.2.2   **Betatron**

A betatron is a circular induction electron accelerator[2], in which the circulating electrons form the secondary winding of a transformer. The primary winding introduces a magnetic flux in the iron yoke, which increases with time. As a consequence the circulating electrons experience an accelerating azimuthal electric field. The strength of the guiding field for which the electrons are kept in a fixed orbit independent of the kinetic energy is determined by the so-called betatron condition. The acceleration is limited by the saturation of the iron. Usually,

the magnetic field is harmonically cycled between the positive and negative maximum with a frequency of 50 Hz. At the maximum energy the electrons can be extracted from the betatron into a beam line.

In case of the soft x-ray Cherenkov source it is not necessary to extract the electron beam. As has been shown by Kaplin *et al.*[3] thin x-ray radiators can be placed inside a betatron through which the electron beam can be recirculated many times. The advantage is that, although the betatron has a low charge per pulse, the average current through the foil is enhanced by the number of passes, which can be a few hundred. In this section the possibilities are discussed of using a 35-MeV betatron for a soft x-ray Cherenkov source. In Fig. 6.1(a) an example is shown of a 5-MeV, commercially available betatron, which can be purchased from Adelphi Technology[4].
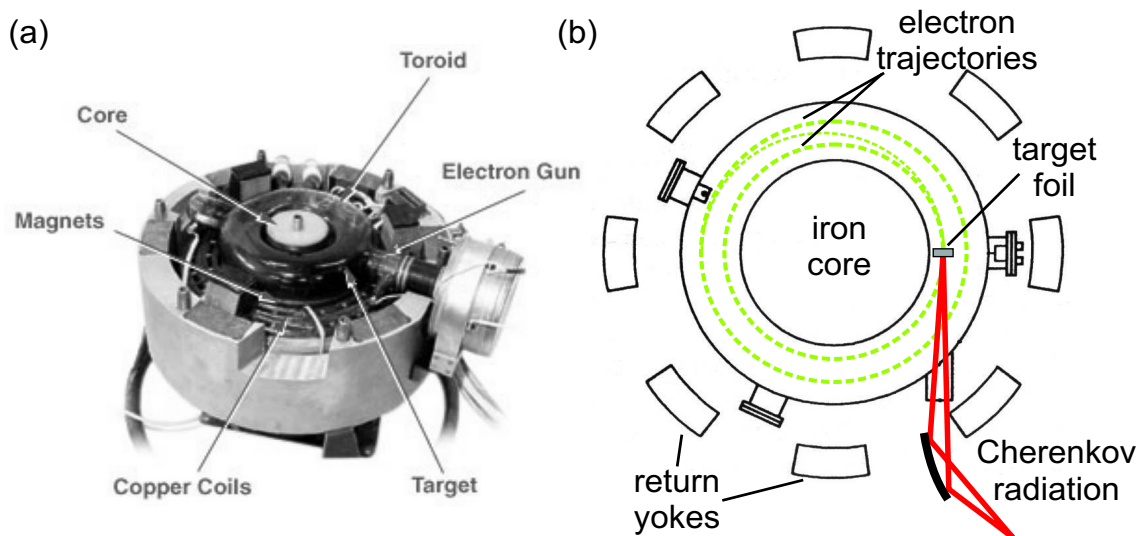
Figure 6.1: (a) Photo of the interior of a 5-MeV betatron. Outer diameter is 36 cm. (b) Betatron scheme.

In the 35-MeV betatron electrons are injected at 60 keV and subsequently accelerated to the desired energy in a stable orbit of $R_0 = 245$ mm. The repetition rate of the accelerator is 50 Hz and the total charge per pulse is 0.4 nC. By switching on an additional magnetic field during a short period the accelerated electrons are moved to an inner orbit, in which a target foil can be placed [see Fig. 6.1(b)]. In a report of Kaplin *et al.*[5] the number of passages possible through thin target foils placed inside this 35-MeV betatron have been presented. It is summarized in Ref. 3 that, for instance, 590 passes have been observed through 1-μm Cu and 460 passes have been observed for 3-μm Mylar. These thicknesses are comparable with the optimal thickness required for the generation of soft x-ray Cherenkov radiation. The scattering of electrons and their energy loss in the target foil cause the beam emittance to increase during the recirculation. At some point an electron is no longer confined in the orbit and is lost immediately. Taking 0.4 nC per pulse passing 500 times through the target foil with a frequency of 50 Hz, the average current is equivalent to about 0.01 mA, which a factor 100 lower than a high-power linear accelerator. Several improvements to the average current of the betatron are feasible, such as injection energy and pulse frequency, which can probably

increase the average current by a factor 10. The hard x-ray background contribution is in case of the betatron lower than in case of the linear accelerator by a factor equal to the number of passes at the same equivalent average current.

Table 6.3: Spectral brightness calculation based on the experimental parameters (QE, θ_{min}, θ_{max}) and theoretical FWHM-bandwidth $\Delta E/E$ and assuming a 0.2-mA average current, 10-MeV electron accelerator with 0.1-mm electron-beam spot size.

material	Cherenkov yield $\times 10^{-4}$ [ph/el]	$\Delta E/E$ $\times 10^{-3}$	θ_{min} [degrees]	θ_{max} [degrees]	spectral brightness [ph·s^{-1}·mm^{-2}·mrad^{-2}·0.1%BW^{-1}]
Ti	3.5	4.4	0.0	4.7	0.6×10^9
V	3.3	2.3	0.0	5.0	1.0×10^9
Si	8.0	10	5	12	1.1×10^8

Inside the betatron the electron beam cannot be focused. If a large target foil is used, a spot size of a few millimeters is obtained[6]. At Adelphi Technology microspot target of 0.1 mm in diameter are proposed to increase the brightness. Such a microspot target reduces the x-ray source size to the size of the target instead of the electron beam spot size. The idea is that the electrons keep circulating until they have passed through the microspot target just as many times as they would have in case of a large target foil.

However, if we apply the heat load discussion of the previous section to the microspot target, the maximum current is limited by radiative cooling from the small front and back surfaces. It turns out that the current limit is about 2 μA ($\bar{J} \approx 0.2$ mA/mm^2) for the three materials, which is 100 times as low as the linear accelerator scheme.

In conclusion, although betatrons have not received much attention lately, we have shown that it is very interesting option for a compact Cherenkov radiation source. The important advantage is that the hard x-ray background is many factors lower than in case of a linear accelerator. In addition, the use of microspot targets can enhances the brightness without decreasing the photon flux too much or using charged particle optics to focus the electron beam.

6.1.3   Achievable brightness

The maximum average current density puts an upper limit on the brightness that can be achieved with the Cherenkov source:

$$B_{max} = \bar{J}_{max} \frac{N}{\Delta\Omega \, \Delta\omega/\omega} \tag{6.8}$$

with N the Cherenkov yield in photon per electron and $\bar{J}_{max}$ the maximum average current density. From the heat-load analysis we have calculated a maximum current density of 20 mA/mm^2, which is obtained by focusing a 0.2-mA average current electron beam to a spot size of 0.1 mm on a rotating, 1-μm thick target foil. For the three Cherenkov emitting materials this foil thickness is about equal to the thickness for optimal Cherenkov generation ($\approx 2.3 \, l_{abs}$). In addition, this foil thickness does not seriously broaden the angular divergence of the electron beam due to elastic scattering.

Table 6.4: Spectral brightness comparison of compact x-ray sources around 13.5 nm.

source type	photon energy [eV]	energy source	relative bandwidth [0.1%]	solid angle [sr]	source size [mm]	spectral brightness [ph·s⁻¹·mm⁻²·mrad⁻²·0.1%BW⁻¹]
Z-pinch plasma[7]	91.9 eV (13.5 nm) with Xe	120-Hz discharge	20	4π	0.5	1.5×10^{10}
Cherenkov source[*]	99.7 eV (12.4 nm) from Si-L	10-MeV, 0.2-mA electron beam	10	0.11	0.1	1.1×10^{8}
EUV tube[8]	91.9 eV (13.5 nm) from silicon	Continuous 10-keV, 1-mA electron beam	20	2π	0.1	1.2×10^{6}

[*] Brightness value assuming 0.2-mA and 100 μm spot size.

Table 6.5: Spectral brightness comparison of compact x-ray sources in the water window.

Source type	photon energy [eV]	energy source	relative bandwidth [0.1%]	solid angle [sr]	source size [mm]	spectral brightness [ph·s⁻¹·mm⁻²·mrad⁻²·0.1%BW⁻¹]
Laser - produced plasma[9]	368 (3.37-nm) C_{IV} from liquid ethanol	100-Hz, 10-Watt Nd:YAG laser	3.3	4π	0.025	6×10^{9}
Cherenkov source[†]	512 (2.42 nm) from V-L	10-MeV, 0.2-mA electron beam	2.4	0.024	0.1	1×10^{9}
High-harmonic generation[10]	284 (4.37 nm)	1-kHz Ti:sapphire laser helium	continuous in water window	Well-collimated	-	5×10^{7}
Liquid x-ray tube[11]	525 (2.36 nm) from oxygen	10-keV, 60-μA electron beam on water jet	7.2	2π	0.1	7×10^{7}

[†] Brightness value assuming 0.2-mA and 100 μm spot size.

Based on the characterization of soft x-ray Cherenkov radiation in the previous Chapter 5, the maximum achievable brightness can be calculated with Eq. (6.8). In Table 6.3 these

brightness figures of titanium, vanadium and silicon are summarized. Although the total yield of silicon is high, the corresponding spectral brightness is lower than titanium and vanadium, which is mainly due to the large solid angle of the silicon L-edge Cherenkov radiation. Theory of Sec. 2.3 shows that grazing-incidence Cherenkov radiation might increase the brightness value, because the radiation is concentrated in a preferred direction and thus the solid angle is decreased.

The brightness values of the soft x-ray Cherenkov sources in Table 6.3 can now be compared to other sources. The typical brightness values of compact x-ray sources around 13.5 nm and in the water window are summarized in Table 6.4 and Table 6.5, respectively. Of each source specific properties are specified to indicate the basis of the brightness number. When our estimated brightness values are compared to these other sources, the proposed soft x-ray Cherenkov source looks very promising. Cherenkov radiation is much brighter than the x-ray tubes and high-harmonic generation. In the water window, the brightness of the soft x-ray Cherenkov source using vanadium is in the same order of magnitude as the brightness achieved with laser-produced plasma sources. A comparison with synchrotron radiation, of which the brightness exceeds the value of the Cherenkov source with at least 4 orders of magnitude, has been omitted, because it is not a compact source.

With the brightness of the laser-produced plasma presented in Table 6.5 soft x-ray microscopy has been demonstrated[9]. The first estimation of the achievable brightness of a Cherenkov source shows that it is in the order of magnitude of what is required for soft x-ray microscopy based on a compact source. We emphasize that in contrast to the laser-based sources, the emission spectrum of the proposed Cherenkov source in the soft x-ray region consists of only a single, strong peak and no wavelength selection is necessary and that, in principle, no debris formation occurs.

6.2   Collector optics and shielding

In the previous section we have characterized the source quality. To use this radiation for a certain application the radiation has to be collected and manipulated with optics. In this section different types of collector optics are discussed, which is the first step after the generation of the Cherenkov radiation. In case of the Cherenkov source the collector optics has to serve two purposes: collecting efficiently all the generated soft x-ray Cherenkov radiation and separating the radiation spatially from the penetrating hard x-ray background. This creates the possibility to put shielding in the direct path from the target foil to the detection system as is schematically shown in Fig. 6.2(a). In the focal point of the collector optics a sample can be positioned. Depending on the application of the source, the spot size, divergence and flux of photons at this point are specified. Additionally, the spectrum of the radiation in this point should be clean from any background radiation, which requires filtering of the Bremsstrahlung, fluorescence and transition radiation.

The collector optics can be put either close to or at large distance from the target foil. In the first option, the electrons have to pass through a hole in the optics [see Fig. 6.2(b)]. This has the advantage that the mirror is relatively small in size. However, this is only possible if the electron beam divergence is smaller than the Cherenkov emission angle. The second

option is preferred when the electron beam is strongly focused on the target foil to obtain a high brightness value. Then the optics is put far away to enable deflection of the electrons before collecting the radiation.
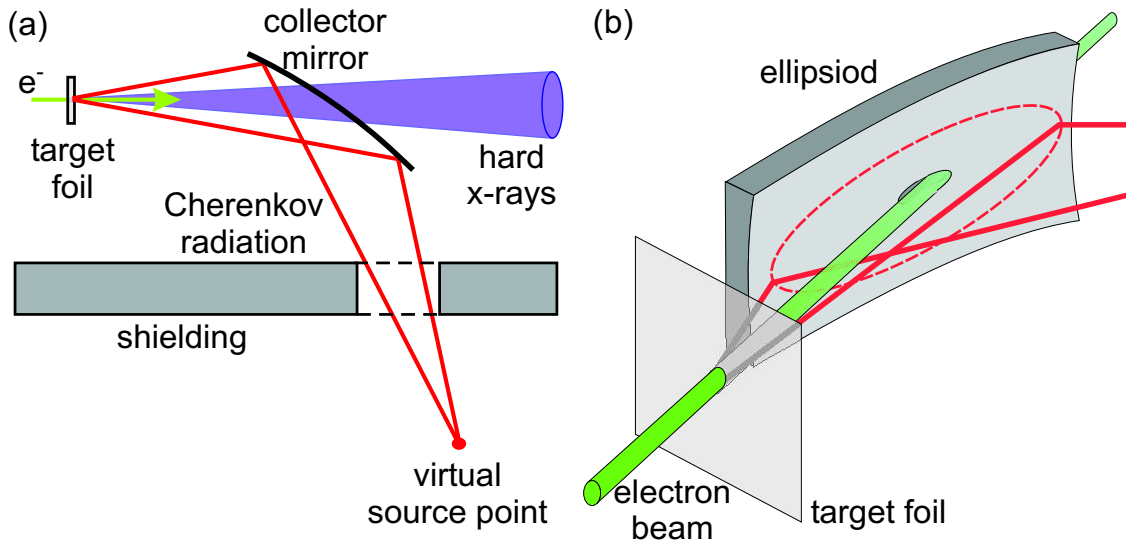
Figure 6.2: (a) Schematic overview of the collector mirror that focuses the Cherenkov radiation to a virtual source, which is then spatially separated from the hard x-ray background. In the direct line of sight from the target foil to the detection setup shielding can be placed.
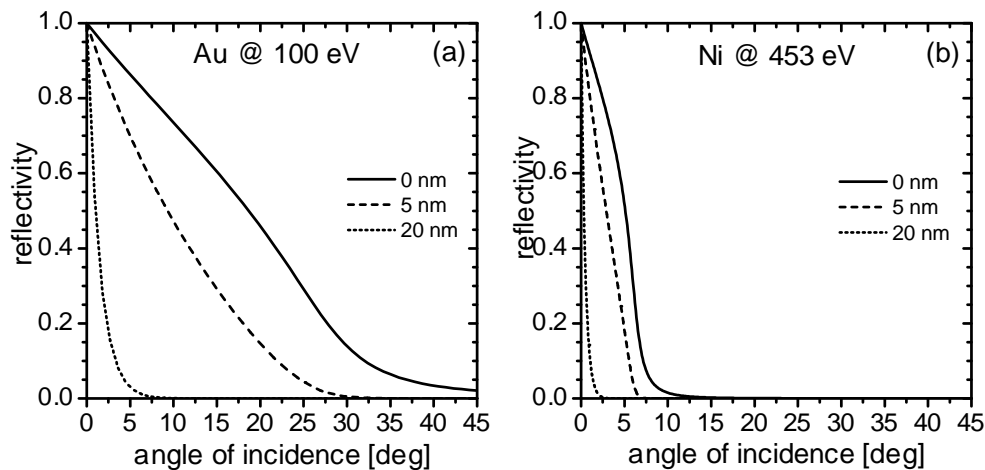
Figure 6.3: (a) Reflectivity of 100-eV radiation from a gold surface as a function of angle of incidence for difference values of RMS roughness. (b) Reflectivity of 453-eV radiation from a gold surface as a function of angle of incidence for difference values of RMS roughness. Both figures are calculated at the CXRO-site for the case of s-polarization.

In the following sections candidate optical systems for the collector are discussed briefly: grazing-incidence mirrors, multilayer mirrors, and capillary optics. Zone plate diffraction

lenses or mirrors are also widely used as x-ray optics. However, for the collection of soft x-ray Cherenkov radiation these lenses are not suited due to their very small size.

## 6.2.1   Grazing-incidence mirrors

X-rays can undergo total external reflection at an interface at grazing incidence angles due to the fact that the refractive index is generally smaller than unity. The angle of total external reflection depends strongly on the dispersion of the surface material. The total external reflectivity is general smaller than unity, because of absorption, surface roughness and contamination. The influence of absorption on the reflectivity is determined by the ratio between the real part and the imaginary part of the refractive index. For optimal reflectivity the real part should be high compared to the imaginary part. The surface roughness lowers the reflectivity due to scattering losses. In general, the RMS roughness of the surface has to be smaller than the wavelength of the incident radiation to have sufficient reflectivity. Finally, contamination or oxidation of the surface may also lower the reflectivity. Therefore, surface materials are preferred that do not easily generate a natural oxide layer or for which the reflectivity of the oxidized surface is comparable to the pure element.

Commonly used materials in the soft x-ray region for grazing-incidence optics are silicon, gold, iridium, nickel[12] and especially around 100 eV ruthenium. By conventional polishing techniques a surface roughness of a few angstrom can be achieved. However, polishing of curved, non-spherical surfaces requires different polishing techniques. Surface materials are also often deposited as a thin layer on a polished substrate. The influence of the roughness is illustrated in Figs. 6.3(a) and 6.3(b) by the reflectivity of a gold surface for 100-eV radiation and of a nickel surface for 453-eV radiation. Typically, in the water-window region smaller angles of incidence are required for total external reflection.
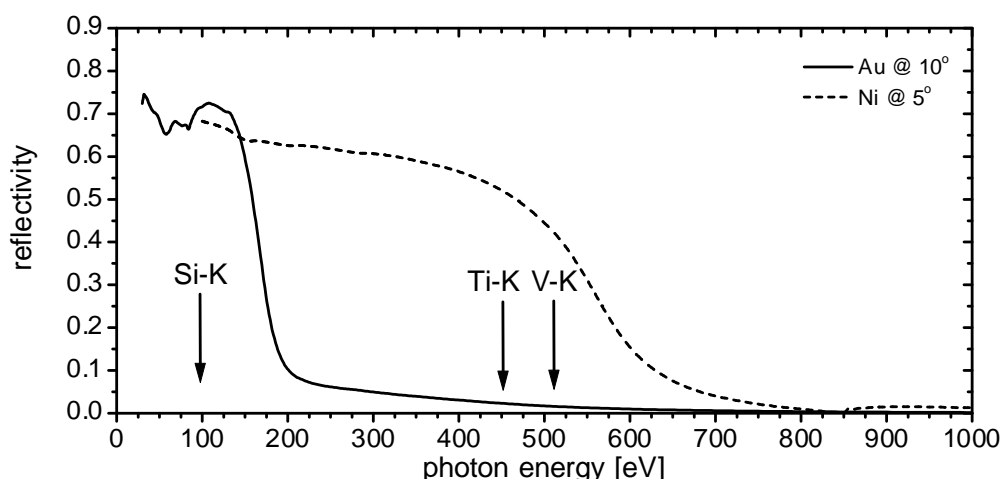

Figure 6.4: Due to dispersion the grazing-incidence optics can also provide a low-pass filter by selecting an angle of incidence, which is shown for three different materials.

The dispersion and absorption of the surface material can actually be used to create a low-pass filter with the grazing-incidence optics. By a proper choice of a material with a

certain absorption edge and choice of an angle of incidence, the high photon-energy part will not be reflected, while the low photon-energy part is still sufficiently reflected. This is illustrated in Fig. 6.4 by the reflectivity as a function of photon energy for the different materials at a specific grazing-angle of incidence. For instance, nickel reflects all photon energies within the water window with a reflectivity between 60% and 40%. At higher photon-energies the reflectivity at an angle of incidence of 5° is negligible.

By using curved surfaces at grazing incidence, reflective focusing or defocusing optics can be made in the soft x-ray region. However, curved surfaces used at grazing incidence give generally rise to large image aberrations[13,14]. For the case of the collector mirror that is required for the Cherenkov source, an ellipsoid provides on-axis point-to-point focusing. Due to the fact that the Cherenkov source area on the target foil has a certain extent, the image by the grazing-incidence ellipsoid still suffers from serious aberration. Well-known solutions with less aberrations are Wolter-type[15] grazing-incidence systems, which consist of two mirrors. For instance, in case of the Cherenkov source a combination of an ellipsoid with either a convex or concave hyperboloid is preferred. With such a system focus spot sizes of a few tens of micrometers have been demonstrated[14].

In conclusion, grazing-incidence optics is a very good option for the collector mirror. Using a Wolter-type system a small spot size can be obtained, although the efficiency is lower than using a single ellipsoid. By choosing the proper surface material at a certain angle of incidence, the transition radiation at higher photon-energies than the Cherenkov line can be filtered out. The overall estimated collection efficiency, which collects all emitted radiation, is between about 50% for Si-K and about 15% for V-K using a two-mirror system.

6.2.2 Multilayer mirrors

Multilayer mirrors are interference reflection-coatings (see Sec. 4.1.3) that enable high normal-incidence reflectivity, filling the gap between ultraviolet reflection of bulk material and x-ray Bragg reflection from crystals. In principle, multilayer mirrors combine very well with the Cherenkov source, because both make use of the anomalous dispersion in combination with the low absorption at the low photon-energy side of the edge. For instance, Mo/Si-multilayer mirrors have a reflectivity of about 70% on the low photon-energy side of the silicon L-absorption edge. In the water-window spectral region mirrors have been demonstrated with about 5% reflectivity at normal incidence using Ti and Sc as spacer material[16]. However, reflection at normal-incidence for photon energies higher than the water window has not been shown, because the layer thickness decreases to a few atomic layers, which causes large difficulties. Therefore, for these photon energies grazing-incidence multilayer mirrors are preferred, because at grazing incidence the layer thickness is still reasonable thick.

The actual implementation of near normal-incidence multilayer mirrors is not very useful, because then the radiation is reflected back to the target foil. To deflect the soft x-ray Cherenkov radiation away from the hard x-rays, reflection angles around 45° are preferred. For these angles the reflectivity of multilayer mirrors in the water window is enhanced, because the layer thickness is larger than at normal incidence. Multilayer coatings can be applied to curved surfaces to produce focusing or defocusing elements. However, when

applying focusing multilayer-mirror at oblique incidence, aberrations are introduced like in the case of grazing incidence.

The advantage of using multilayer-coated optics over grazing-incidence optics is the fact that it provides a narrow bandpass filter around the desired photon energy. In the water window a promising option is the combination of multilayer coatings and grazing-incidence optics. Although the spectral resolution is low due to the fact that fewer layers contribute to the reflectivity at grazing-incidence, the filtering ability is still higher than without a multilayer coating. The estimated collection efficiency for a multilayer is about 77% for Si-K Cherenkov radiation at 45° and about 20% for the water-window using coated grazing-incidence optics.

6.2.3   Capillary optics

Capillary optics is also based on total external reflection at grazing incidence. A cylindrical capillary guides light by total reflection on the internal surface of the capillary. Due to losses caused by the surface roughness and absorption, the length of the capillary is typically limited to 1 m. The entrance aperture of the capillary is matched to accept only the grazing-angles of total reflection. Capillary optics can consist of a single tube or of multiple capillaries. The first acts as a collimator, but can only collect a very small solid angle. The latter consists of a large collection of capillaries. The multicapillary can contain thousands of small capillaries and therefore collect a large solid angle (up to about 10º)[17]. By directing the beginning and the ending of the capillaries within the bundle to a focus point on each side, x-rays emitted from a source point can be focused into a second point. The x-ray beam divergence at the end of an individual capillary and the focal distance of the bundle determine the spot size in the focal point of the multicapillary. Spot sizes of a few tens of μm have been reported[14].

In the case of the Cherenkov source a multicapillary is required that provides not only focusing from target foil to a virtual source point, but also bending around an arc to separate the guided soft x-rays from the penetrating hard x-rays. Up to now, multicapillaries have been demonstrated with multi-keV radiation. In principle, there are no limitations to use it in the soft x-ray region as long as the reflectivity at the internal surface of the capillaries is high enough. Overall transmissions of a few times ten percent have been reported[14].

6.3   Challenging applications

In the introduction we have introduced two applications of the soft x-ray Cherenkov source. Of course many other applications can be found with each a specific demand on the brightness value. In particular soft x-ray microscopy and x-ray photoelectron spectroscopy are the most challenging. Imaging applications, such as soft x-ray microscopy, require a high brightness value. Soft x-ray microscopy has been demonstrated using a compact source with a brightness value between 10^9 and 10^{10} ph·s^{-1}·mm^{-2}·mrad^{-2}·0.1%BW^{-1}. The linear accelerator is therefore best suited for these applications. For example, assuming the linear accelerator is operated at 0.2-mA average current and the electron beam is focused to a spot size of 0.1 mm on the target foil. When using a vanadium foil the source brightness value is about 1×10^9 ph·s^{-1}·mm^{-2}·mrad^{-2}·0.1%BW^{-1}. Grazing-incidence Wolter optics is the best option to preserve

the brightness as well as to focus the beam to a 10-μm spot size. Due to the two reflections at the Wolter optics (40 % each) the brightness at the sample position is about 2×10^8 ph·s^{-1}·mm^{-2}·mrad^{-2}·0.1%BW^{-1}. To make a soft x-ray microscope image also the x-ray flux is of importance, because it determines the exposure time. According to estimations[18] the flux should be between 10^8 and 10^9 ph s^{-1} μm^{-2} on the sample to result in an exposure time of a few seconds for 25-nm resolution zone plate imaging. If we collect all the generated Cherenkov radiation using the specified accelerator and focus the radiation on a 10-μm spot size, the estimated flux on the target position is 8×10^8 ph s^{-1} μm^{-2}, which is within the required flux range.

The linear accelerator can produce a higher brightness than the betatron. However, the microspot target in betatron is still an interesting option for x-ray photoelectron spectroscopy. For x-ray photoelectron spectroscopy the flux on the target position is specified, which is a derived value from the brightness without a firm requirement for bandwidth and solid angle. Typically, the flux has to be larger than 10^8 ph/s on a 10-μm spot. For instance, operating the betatron at 2-μA average current a photon flux of about 4×10^9 photon per second is produced for the case of titanium and vanadium. If all photons are collected with a multicapillary and focused with 10× demagnification and a reflection efficiency of 25%, 1×10^9 photons per second on a 10-μm spot size can be obtained at the sample position. This flux amply fulfills the requirements for x-ray photoelectron spectroscopy. The advantage for this application of a betatron over a linear accelerator is that it is, in general, cheaper, even more compact than linear accelerators in the same energy range and that it requires substantially less shielding.

References

[1] M. Born and E. Wolf, *Principles of optics: electromagnetic theory of propagation, interference and diffraction of light*, Cambridge University Press, Cambridge, 1999.

[2] S. Humphries Jr., *Principles of charged particle acceleration,* online available at: http://www.fieldp.com/cpa/cpa.html, Wiley-Interscience, Chichester, 1986.

[3] V.V. Kaplin, S.R. Uglov, O.F. Bulaev, V.J. Goncharov, A.A. Voronin, M.A. Piestrup, C.K. Gary, N.N. Nasonov and M.K. Fuller, "Tunable, monochromatic x rays using the internal beam of a betatron", *Appl. Phys. Lett.* **80**, 3427-3429 (2002).

[4] Adelphi Technology, Palo Alto, USA, http://www.adelphitech.com.

[5] V.V. Kaplin, S.R. Uglov, O.F. Bulaev, V.J. Goncharov, A.A. Voronin, M.A. Piestrup and C.K. Gary, "Thin betatron radiators for more efficient x-ray generation", *Rev. Sci. Instrum.* **73**, 63-68 (2002).

[6] V.V. Kaplin, S.R. Uglov, O.F. Bulaev, V.J. Goncharov, M.A. Piestrup and C.K. Gary, "Observation of multiple passes of electrons through thin internal targets of a betatron", *Nucl. Instrum. Methods* **B173**, 3-15 (2001).

[7] R. Struik, *Characterisation of XUV Sources*, Technische Universiteit Eindhoven, Eindhoven, 2002.

[8] A. Egbert, B. Mader, B. Tkachenko, A. Ostendorf, C. Fallnich, B.N. Chichkov, T. Missalla, M.C. Schürmann, K. Gäbel, G. Schriever and U. Stamm, "Compact electron-based extreme ultraviolet source at 13.5 nm", *J. Microlith., Microfab., Microsyst.* **2**, 136-139 (2003).

[9] G.A. Johansson, A. Holmberg, H.M. Hertz and M. Berglund, "Design and performance of a laser-plasma-based compact soft x-ray microscope", *Rev. Sci. Instr.* **73**, 1193-1197 (2002).

[10] E.A. Gibson, A. Paul, N. Wagner, R. Tobey, D. Gaudiosi, S. Backus, I.P. Christov, A. Aquila, E.M. Gullikson, D.T. Attwood, M.M. Murnana and H.C. Kapteyn, "Coherent soft x-ray generation in the water window with quasi-phase matching", Science **302**, 95-98 (2003).

[11] B. Buijsse, "A keV-electron-based tabletop soft X-ray source", in Proceedings of SPIE Vol. 4502, 74-81 (2001).

[12] R.L. Sandberg, D.D. Allred, J.E. Johnson and R.S. Turley, "A comparison of uranium oxide and nickel as single-layer reflectors from 2.7 to 11.6 nanometers", in Proceedings of SPIE Annual Meeting 2003 in San Diego, 2003.

[13] J. H. Underwood, "Imaging properties and aberrations of spherical optics and nonspherical optics", in *Vacuum Ultraviolet Spectroscopy I*, edited by J.A. Samson and D. L. Ederer, (Academic Press, San Diego, 1998), Chap. 9, pp. 145-181.

[14] P. Dhez, P. Chevallier, T.B. Lucatorto and C. Tarrio, "Instrumental aspects of x-ray microbeams in the range above 1 keV", *Rev. Sci. Instrum.* **70**, 1907-1920 (1999).

[15] H. Wolter, *Ann. Der Phys.* **10**, 94-114 (1952).

[16] E. Spiller, "Reflection optics: Multilayers", in *Vacuum Ultraviolet Spectroscopy I*, edited by J.A. Samson and D. L. Ederer, (Academic Press, San Diego, 1998), Chap. 14, pp. 271-288.

[17] M.A. Kumakhov, "Channeling of photons and new x-ray optics", *Nucl. Instrum. Methods* **B48**, 283-286 (1990).

[18] H. Hertz (private communication).

Samenvatting

Dit proefschrift beschrijft het onderzoek naar de fysica van een nieuw type stralingsbron in het zachte röntgengebied. Het principe van deze zachte röntgenbron is de generatie van Cherenkovstraling dat wordt uitgezonden door relativistische elektronen tijdens de passage door een dun folie. In dat folie is de snelheid van de elektronen (bijna 300000 km per seconde) een klein beetje hoger dan de snelheid van lichtgolven in dat materiaal. Daardoor ontstaat er in het folie een schokgolf van licht, analoog aan de boeggolf van een schip. De fasesnelheid van licht in een materiaal wordt bepaald door de brekingsindex. Om het Cherenkoveffect mogelijk te maken, moet de brekingsindex groter zijn dan één. Hier wordt in het algemeen aan voldaan in het zichtbare gebied, waar Cherenkovstraling dan ook veel wordt toegepast. In het röntgengebied werd tot kort geleden Cherenkovstraling uitgesloten, omdat naast het feit dat materialen niet transparant zijn, de brekingsindex in het algemeen kleiner is dan één. In 1981 werd aangetoond dat Cherenkovstraling in het röntgengebied wel mogelijk is. Dit werd gedemonstreerd met een koolstoffolie en zeer relativistische elektronen. Het project beschreven in dit proefschrift bestudeert de mogelijkheid van een zachte röntgenbron gebaseerd op Cherenkovstraling, gegenereerd door relatief laag energetische elektronen. Het interessante voordeel van deze nieuwe röntgenbron is de compacte omvang van de benodigde elektronenversnellers.

Het zachte röntgengebied (dit beslaat fotonenergieën van ongeveer 100 eV tot enkele keV's) is een zeer interessant gedeelte van het elektromagnetisch spectrum, ondanks de moeilijkheden door de hoge absorptie van straling in alle materialen. De korte golflengte van het licht (van ongeveer 20 nm tot 1 nm) biedt de mogelijkheid om zeer kleine structuren van nanometer afmetingen (een miljoenste van een millimeter) af te beelden. Voor biologische studies biedt microscopie in het zachte röntgengebied een unieke combinatie van mogelijkheden tussen die van licht- en elektronenmicroscopie. De natuur creëert een 'water window' in het spectraal gebied tussen de absorptiekant van koolstof en van zuurstof waarin een hoog contrast ontstaat tussen organische materiaal (sterk absorberend) en de waterige omgeving (relatief transparant), bijvoorbeeld een dierlijke cel. Daarnaast biedt het zachte röntgengebied de mogelijkheid van chemische identificatie aan de hand van de bindingsenergieën van atomaire elektronen. Een bekende analysetechniek die dit mogelijk maakt is röntgen foto-elektron spectroscopie (XPS), dat veel wordt gebruikt om de chemische samenstelling van oppervlakten en dunne lagen te bepalen.

De huidige röntgenbronnen voor zachte röntgenmicroscopie zijn voornamelijk synchrotron lichtbronnen. Synchrotrons zijn grote elektronenopslagringen van enkele tientallen tot enkele honderden meters in diameter en zijn de helderste bronnen in dit spectrale gebied. Echter door de enorme omvang zijn deze lichtbronnen zeer duur en zijn er maar een beperkt aantal in de wereld. Bijvoorbeeld, voor biologen is het zeer interessant om over een eigen röntgenmicroscoop te beschikken. Daarom is er voor een compacte heldere röntgenbron zeer veel interesse. De meest gebruikte bron voor XPS is een röntgenbuis. Vergeleken met synchrotronbronnen zijn röntgenbuizen compacte bronnen, maar hebben een lage intensiteit. Daarom is het ook voor deze toepassingen interessant om een compacte bron te gebruiken die veel meer intensiteit produceert, zodat er sneller en met een hogere gevoeligheid gemeten kan worden. Op basis van het onderzoek in dit proefschrift tonen wij aan dat de zachte röntgen Cherenkovbron in principe geschikt is voor beide toepassingen.

In dit proefschrift wordt de theorie van Cherenkovstraling uitgebreid besproken. Omdat Cherenkovstraling in dunne folies wordt gegenereerd, wordt er door de elektronen tevens transitiestraling gegenereerd als ze het folieoppervlak passeren. In de theorie worden beide effecten gewoonlijk apart beschouwd, maar juist voor zachte röntgenstraling is het belangrijk om beide gelijktijdig te analyseren. Met behulp van de uitdrukking voor de stralingsintensiteit kunnen we de Cherenkovstraling karakteriseren aan de hand van de brekingsindex in het zachte röntgengebied. Voor sommige materialen piekt de brekingsindex in het zachte röntgengebied even boven één uit als gevolg van anomale dispersie bij fotonenergieën rond de bindingsenergie van elektronenschillen. Uit deze theoretische analyse volgt dat de gegeneerde zachte röntgen Cherenkovstraling van nature nauwbandig is en wordt uitgezonden in een holle kegel met een kleine tophoek in de voorwaartse richting van de elektronenbundel. De theoretische opbrengst van de Cherenkovstraling blijkt hoog genoeg te zijn voor toepassing als bron. Daarnaast zijn relatief lage elektronenergieën (5 MeV tot 25 MeV) al voldoende om Cherenkovstraling effectief te genereren. Als laatste kunnen verschillende Cherenkov lijnen worden gegenereerd door eenvoudig van foliemateriaal te wisselen.

Het doel van de experimenten was om deze theoretische eigenschappen van Cherenkovstraling aan te tonen. Tot dan toe waren er twee eerdere experimentele waarnemingen van Cherenkovstraling bekend, namelijk bij de silicium L-absorptiekant (100 eV) en koolstof K-absorptiekant (284 eV), gegenereerd met zeer hoog-energetische elektronen (75 MeV en 1,2 GeV). Wij hebben gebruik gemaakt van twee verschillende elektronenversnellers met elk een eigen gespecialiseerde detectieopstelling. Een 5 MeV lineaire elektronenversneller is gebruikt om silicium L-absorptiekant Cherenkovstraling te genereren. De gegenereerde straling is geanalyseerd met een spectrometer gebaseerd op een röntgen multilaagsspiegel. Een 10 MeV lineaire elektronenversneller is gebruikt om Cherenkovstraling met hogere fotonenergieën te genereren. De straling is geanalyseerd met een speciale zachte röntgencamera, waarmee de energie van ieder gedetecteerd foton bepaald kan worden. Een van de belangrijkste aspecten van de experimenten was het onderscheiden van de Cherenkovstraling uit de achtergrondstraling via een detectorspecifieke methode. Deze achtergrond bestaat uit andere stralingsverschijnselen die inherent zijn aan het passeren van relativistische elektronen door een dun folie, zoals fluorescentiestraling, Bremsstrahlung en transitiestraling.

Door middel van de experimenten hebben we de generatie van silicium L-absorptiekant (100 eV) Cherenkovstraling met 5 MeV elektronen aangetoond. Daarnaast hebben we met 10 MeV elektronen Cherenkovstraling in het water window aangetoond van twee nieuwe materialen, namelijk titaan L-absorptiekant (453 eV) en vanadium L-absorptiekant (512 eV) Cherenkovstraling. De gemeten intensiteiten en hoekverdelingen van de Cherenkovstraling kwamen goed overeen met de theoretische berekeningen op basis van brekingsindexdata. In het bijzonder was de gemeten intensiteit van de vanadium Cherenkovstraling ongeveer twee maal zo hoog als theoretisch berekend. Een kleine aanpassing aan de brekingsindexdata kan onze meting verklaren.

Daarnaast hebben we nog andere pogingen ondernomen om Cherenkovstraling te genereren met 10 MeV elektronen in koolstof, nikkel en siliciumnitride. (i) Koolstof is interessant omdat Cherenkovstraling bij de K-absorptiekant (284 eV) al eerder is waargenomen met hoogenergetische elektronen. Ondanks het feit dat de drempel voor het Cherenkoveffect ruim voldoende was voor 10 MeV elektronen, hebben wij geen Cherenkovstraling waargenomen. Daarom kunnen we op basis van deze metingen een nieuwe maximale waarde voor de brekingsindex van koolstof bij de K-absorptiekant vaststellen. (ii) Nikkel is gekozen omdat op basis van de brekingsindex dit de hoogst mogelijke Cherenkov fotonenergie (852 eV) oplevert met behulp van 10 MeV elektronen. Omdat maar net aan de drempelwaarde is voldaan, is het niet verrassend dat hier geen nikkel Cherenkovstraling is waargenomen. (iii) Siliciumnitride is onderzocht om het idee te testen of met 10 MeV elektronen Cherenkovstraling gegenereerd kan worden met gasvormige elementen, zoals stikstof, maar dan in vaste chemische vorm. Echter, er is geen Cherenkovstraling waargenomen.

Op basis van de metingen van de gegenereerde Cherenkovstraling hebben we aan het einde van het proefschrift de vergelijking gemaakt met andere compacte zachte röntgenbronnen. Om verschillende bronnen met elkaar te vergelijken bereken we de waarde van de bronhelderheid. De berekeningen laten zien dat onze zachte röntgen Cherenkovbron een vergelijkbare helderheid heeft als laser geproduceerde plasmabronnen, die tot nu toe de helderste compacte bronnen in het water window zijn. Omdat dit type bron al toegepast is bij röntgenmicroscopie experimenten, toont aan dat ook onze Cherenkovbron in principe geschikt is voor die toepassing. De voordelen van de Cherenkovbron zijn dat het röntgenspectrum uit een enkele sterke smalle lijn bestaat, dat alle gegenereerde straling effectief kan worden gecollecteerd met optiek onder scherende inval en dat er in principe geen 'debris' wordt gegenereerd.

Dankwoord

In dit proefschrift zijn de resultaten van mijn promotieonderzoek samengevat die zijn behaald over de afgelopen vier jaar. Op deze plek wil ik graag van de gelegenheid gebruik maken om mensen te bedanken die een bijdrage hebben geleverd aan de resultaten van het promotieonderzoek. Om mee te beginnen, mede dankzij de inzet van een groot aantal stage- en afstudeerstudenten zijn veel van de resultaten tot stand gekomen. In chronologische volgorde waren dat: Joeri de Groot, Roel Moonen, Ivo Classen, Roger Wolf (Universiteit van Heidelberg), Andreas Hillenbach (Universiteit van Heidelberg), Frank van Kempen, Wim Deferme, Karin Hendriks, Niek Kleemans, Ralph Brummans. Ik heb met veel plezier met deze studenten samengewerkt en hen begeleid.

Speciale bewondering wil ik uitspreken voor de enthousiaste inzet van Leo de Folter. De technische ondersteuning van hem vanaf het begin van het project is essentieel geweest. Door zijn zeer brede inzetbaarheid hebben we veel werk kunnen verzetten aan de opstellingen. Zo stond aan het begin van het project de LINAC-5 in een onwerkbare opstelling. We hebben daarom de bunker verbouwd, infrastructuur aangelegd, de versneller op een bok geplaatst en een bundelondersteuning gemaakt. Nadat met deze opstelling de zeer belangrijke resultaten van silicium Cherenkovstraling waren behaald, begon helaas de renovatie van het cyclotrongebouw die langer duurde dan gepland. Ook hierbij heeft Leo zeer veel werk verzet om de experimenten tot zeer kort voor en zo snel mogelijk na renovatie te continueren. Nogmaals, deze ondersteuning van Leo is onmisbaar geweest.

Dit promotieproject is geïnitieerd door Jan Verhoeven van het FOM-instituut AMOLF. Veel vooronderzoek is toentertijd verricht door een afstudeerstudent Boris Lastdrager, van wie ik een numeriek rekenprogramma voor Cherenkovstraling heb gekregen en waar ik dankbaar gebruik van heb gemaakt. Gedurende het project kwam Jan vaak tijdens werkbezoekjes met leuke ideetjes aanzetten. Ook SRON in Utrecht is vanaf het begin betrokken geweest bij dit promotieproject. Voordat ik begon, is er al een prototype CCD-camera in Eindhoven getest. Onderleiding van Ton den Boggende is er door SRON een zachte röntgen CCD-camera gebouwd, die uiteindelijk in de LINAC-10 opstelling is gebruikt. Met deze zeer gevoelige camera met spectraal oplossend vermogen zijn twee nieuwe Cherenkov emitterende materialen gevonden, namelijk titaan en vanadium. Bij deze wil ik Ton en zijn team bedanken voor de ondersteuning die ze hebben gegeven voor de CCD-camera.

Vanaf halverwege het promotieproject kwam naast de LINAC-5 ook de LINAC-10 beschikbaar voor mijn experimenten. Voordat deze versneller gebruikt kon worden, moesten er veel aanpassingen worden gemaakt. Veel werk aan de elektronica en besturing is verricht door Harry van Doorn en Ad Kemper. Deze versneller is essentieel geweest voor het succes van Cherenkovstraling in het water-window spectrale gebied, wat een zeer belangrijk resultaat is van mijn promotieproject. Een detectieopstelling voor Cherenkovstraling achter deze versneller is door de Gemeenschappelijke Technische Dienst van de TU/e vervaardigd. Daarbij heb ik de samenwerking met Erwin Dekkers en Jurgen Bulsink als zeer constructief ervaren.

Tijdens het project hebben we een aantal experimenten gedaan waarbij we een spectrometeropstelling hebben gebruikt van Philips Research Laboratories, bestaande uit een CCD-camera en EUV-grating. Graag wil ik Jeroen Jonkers bedanken voor zijn inspanning daarvoor. Daarnaast hebben we voor Cherenkov metingen aan silicium een Si/Mo-multilaagspiegel van het FOM-instituut Rijnhuizen gekregen dat een onderdeel is van een spectrometer, waarvoor ik graag Erik Louis wil bedanken.

Mijn promotieonderzoek stond onder de begeleiding van mijn copromotor Jom Luiten en promotor Marnix van der Wiel. De afgelopen vier jaar heb ik van beiden veel geleerd. Marnix heeft altijd oog gehad voor de juiste toon bij de presentatie van de resultaten. Door de samenwerking met Jom heb ik vooral het schrijven van artikelen sterk weten te ontwikkelen. Vanaf het begin van het project heb ik het enthousiasme en de gedrevenheid van Jom als zeer motiverend ervaren. De hoeveelheid ideetjes die de revue zijn gepasseerd de afgelopen vier jaar zijn bijna ontelbaar en ik hoop dat ik iets van die enorme inventiviteit heb meegekregen voor mijn verdere loopbaan. Hierbij wil ik Jom zeer bedanken voor de dagelijkse begeleiding van mijn promotieproject.

De afgelopen vier jaar heb ik met veel plezier gewerkt in de capaciteitsgroep Fysica en Toepassingen van Versnellers. In het wetenschappelijk onderzoek met al zijn facetten, zoals experimentele, theoretische, technische, begeleiding van studenten en wisselwerking met collega's, voel ik mij zeer thuis. Daarom vind ik het jammer dat ik deze periode bij de universiteit moet afsluiten, maar ik hoop op een voortzetting van mijn loopbaan in het technisch-wetenschappelijk onderzoek.

Graag wil ik als afsluiting in herinnering brengen dat ik heb genoten van de enthousiaste discussies die vaak geïnspireerd werden door de dagelijkse actualiteit gedurende de koffiepauzes. De "Faculty Pub", die ik meerdere keren met Jaap Corstens heb georganiseerd, is na een periode van regelmatige gezellige vrijdagmiddagborrels helaas de laatste tijd wat ingezakt. Misschien dat hier in de toekomst nieuw leven ingeblazen kan worden. Bij deze wil ik nogmaals alle collega's van FTV en TIB bedanken voor mijn fijne tijd op de TU/e.

Walter Knulst
Eindhoven, december 2003

Curriculum vitae

1976   Geboren in Alkmaar

1994-1999   Studie Technische Natuurkunde met afstudeerrichting laserfysica aan
                de Universiteit Twente (UT) te Enschede

1999-2003   Promovendus aan de Technische Universiteit Eindhoven (TU/e) in de
                capaciteitsgroep Fysica en Toepassingen van Versnellers (FTV) van
                de faculteit Technische Natuurkunde.